REVIEW ARTICLE

Phonons and elasticity in critically coordinated lattices

T C Lubensky[1], C L Kane[1], Xiaoming Mao[2], A Souslov[3] and Kai Sun[2]

[1] Department of Physics and Astronomy, University of Pennsylvania, Philadelphia, Pennsylvania, 19104, USA

E-mail: tom@physics.upenn.edu

[2] Department of Physics, University of Michigan, Ann Arbor, MI 48109, USA

[3] School of Physics, Georgia Institute of Technology, Atlanta, Georgia 30332, USA

Contents

Abstract. Much of our understanding of vibrational excitations and elasticity is based upon analysis of frames consisting of sites connected by bonds occupied by central-force springs, the stability of which depends on the average number of neighbors per site z. When $z < z_c \approx 2d$, where d is the spatial dimension, frames are unstable with respect to internal deformations. This pedagogical review focuses on properties of frames with z at or near z_c, which model systems like randomly packed spheres near jamming and network glasses. Using an index theorem, $N_0 - N_S = dN - N_B$ relating the number of sites, N, and number of bonds, N_B, to the number, N_0, of modes of zero energy and the number, N_S, of states of self stress, in which springs can be under positive or negative tension while forces on sites remain zero, it explores the properties of periodic square, kagome, and related lattices for which $z = z_c$ and the relation between states of self stress and zero modes in periodic lattices to the surface zero modes of finite free lattices (with free boundary conditions). It shows how modifications to the periodic kagome lattice can eliminate all but trivial translational zero modes and create topologically distinct classes, analogous to those of topological insulators, with protected zero modes at free boundaries and at interfaces between different topological classes.

1. Introduction

Understanding and controlling mechanical stability is important to fields ranging from structural engineering to granular materials and glasses. We do not want buildings or bridges to fail, and we want to be able to manage the elastic response of materials of everyday life. This review focusses on the elastic and dynamical properties of periodic ball-and-spring networks that are at or near mechanical collapse. This may seem like a fairly narrow subject, but it is one of considerable richness and impact.

In a remarkable 1864 paper [1], James Clerk Maxwell undertook the first systematic study of the mechanical stability of frames consisting of points, which we will refer to as *sites*, with connections, which we will usually refer to as *bonds*, between them as a model for such real-world structures as the Warren Truss (patented in 1848) shown in figure 1. He defined a "stiff" frame as one in which "the distance between two points cannot be altered without changing the length of one or more connections". He showed that a stiff frame containing N sites in d dimensions requires

$$N_B = dN - f(d) \tag{1.1}$$

connections, where $f(d) = d(d+1)/2$ is the number of rigid translations and rotations under free boundary conditions. Under periodic boundary conditions, which Maxwell did not consider, $f(d) = d$. This relation, often referred to as *Maxwell's rule*, can be reexpressed as a critical coordination number ($z \equiv 2N_B/N$),

$$z_c^N = 2d - 2\frac{f(d)}{N}. \tag{1.2}$$

If $z < z_c^N$, the system is not stiff, and if $z > z_c^N$, it is. As we shall discuss in more detail in the next section, Maxwell's rule for the stability of frames requires modification [2]. Nevertheless, it provides a useful and universally used benchmark for the analysis of the stability of frames. We will refer to free frames, i.e., ones under free boundary conditions, satisfying Maxwell's rule as *Maxwell frames*. It is fairly common practice to use the term *isostatic* for frames satisfying Maxwell's rule. Though isostatic frames do satisfy Maxwell's rule, they have more restrictive properties, which we will discuss in section 2.

Our principal interest here is in frames whose sites can be collected into identical contiguous unit cells whose origins lie on a Bravais lattice and which fill some region of space. We will refer to these frames as *lattices* and if they are subjected to periodic (free) boundary conditions as periodic (free) lattices. Any frame, even those that are not lattices, e.g., whose sites are randomly distributed, can also be subjected to periodic (free) boundary conditions in which case we will refer to them as periodic (free) frames. For reasons that we will justify more fully later, we will use the term *periodic Maxwell frame (lattice)* for periodic frames (lattices) with average coordination number $z_c = 2d = z_c^\infty$ rather than z_c^N. Free frames can be liberated from periodic ones by cutting of order $N^{(d-1)/d}$ bonds.

Maxwell's analysis applies to frames with an arbitrary number of sites and bonds. In addition to being a workhorse of the structural engineering community [3, 4], it has seen extensive use (though not always with attribution to Maxwell) in physics, materials science, and mathematics. It is a critical component of the theory of structural glasses [5, 6, 7, 8, 9], rigidity percolation [10, 11, 12, 13, 14], framework silicates like β-cristobalite [15], jamming of packed spheres [16, 17, 18, 19, 20],
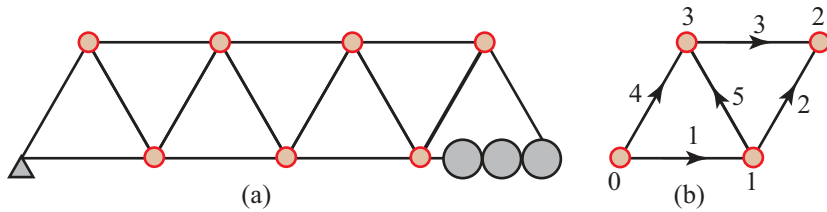
Figure 1. (a) The Warren Truss. This is an isostatic structure composed of equilateral triangles with $N = 9$ sites and $N_B = 15$ connections, so that $2N - N_B = 3$. The lower left site (indicated by the small triangle) is fixed with respect to the earth, and the lower right site is constrained to move only horizontally along a track with wheels. These constraints reduce the number of free degrees of freedom of the sites by 3 to $N_{free} = 2N - 3 = 15 = N_B$. (b) A reduced version of the isostatic Warren Truss indicating conventions for labeling sites and bonds. The arrows indicate indicate bond directions following the convention described in section 2.2, Eqs. (2.10) to (2.13).

biopolymer networks [21, 22, 23, 24, 25, 26, 27, 28], and of some theories of protein folding [29]. Rigidity percolation and jamming generally involve central forces only, and the Maxwell relation and its generalization can be applied to these problems directly. Structural glasses and biopolymer networks have bending forces that require a modification of the Maxwell rules, and we will not make much contact with them in what follows.

Both randomly packed spheres (figure 2(a)) and diluted elastic networks (figure 2(b)) pass from a state that does not support stress to one that does as the number of bonds or contacts increases. At the critical point separating these two states, the coordination number is at or near the Maxwell critical value of z_c. The rigidity percolation transition is generally continuous [10, 11, 12, 14] in two-dimensions, and it is well-described by the language of critical phenomena, applied so successfully to percolation in random resistor networks [30, 31]. Both shear and bulk elastic moduli increase from zero as a power law in $(z - z_c)$, and there is a divergent length scale associated with the probability that two sites are in the same rigid cluster as a function of their separation. In three dimensions, the rigidity transition is apparently first order [14].

Jammed systems exhibit different behavior. They are constructed by increasing the density of spheres in a fixed volume until they first resist a further increase. At this point, they are jammed, and their bulk modulus B (which resists compression) is nonzero [32, 33], but their shear modulus G is of order $1/N$ [34, 35]. At large N, G increases linearly in $\Delta z = (z - z_c)$ [36, 32, 33]. The density of states of systems with $\Delta z > 0$ exhibits a crossover from Debye-like behavior ($\sim \omega^{d-1}$ in d dimensions as a function of frequency ω) at low frequency to a flat-plateau beyond a characteristic frequency $\omega^* \sim (\Delta z)$ [33, 37]. There are two diverging length scales, $l^* \sim (\Delta z)^{-1}$ and $l_T \sim (\Delta z)^{-1/2}$, which can be extracted [37] by, respectively, comparing ω^* to the longitudinal and transverse sound frequencies $c_L l^{-1}$ and $c_T l^{-1} \sim (\Delta z)^{1/2} l^{-1}$ at wavenumber $q \sim l^{-1}$, where $c_L \sim B^{1/2}$ and $c_T \sim G^{1/2}$ are the longitudinal and transverse sound velocities. Other interpretations of these lengths invoke finite-size effects in the modes of a finite sample cut from a larger one [18, 17, 38] for l^* and stability of the system to boundary perturbations [39, 40], crossover between strong and weak scattering at ω^* [41, 42], or correlations in systems with $z < z_c$ [43, 44] for

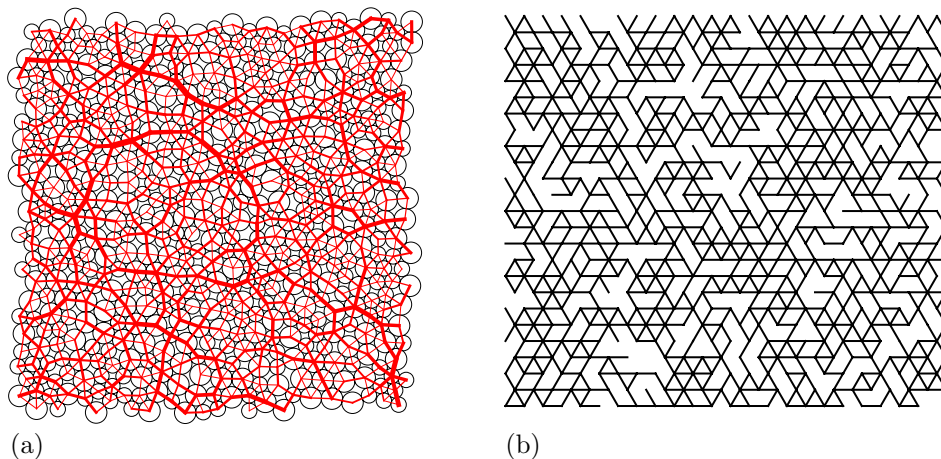(a)   (b)

Figure 2. (a) packed discs of two sizes just above the jamming transition. The dark red lines are chains of force that are a response to the pressure required to pack the particles at $z > z_c$ (courtesy of Carl Goodrich). (b) A representative bond-diluted lattice near the rigidity percolation threshold of $z_c \approx 3.96$.
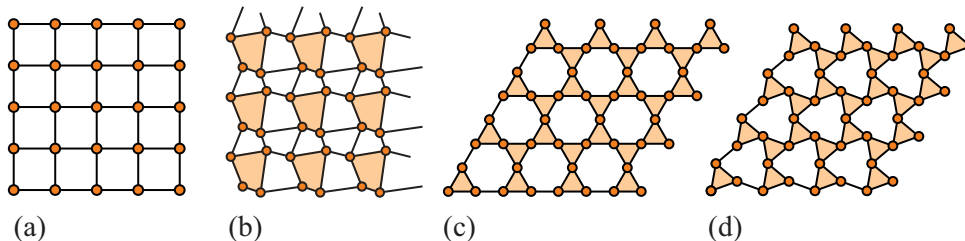

(a)   (b)   (c)   (d)

Figure 3. (a) Square, (b) distorted square, (c) kagome lattice, and (d) twisted kagome lattice

l_T.

Though the transition to elastic stability in both rigidity percolation and jamming occurs at or near the Maxwell critical point $z = z_c$, properties at and above the two transitions are quite different. Presumably, the difference is a reflection of the different geometrical arrangements of the Maxwell lattices at or near the two transitions. An interesting question then is what precisely are the differences. Can they be quantified, and if so how? These questions then raise a broader question of whether there are wider classes of Maxwell frames that lead to elastic and vibrational structure different from those of the percolation and jamming lattices. As a first step toward answering that question, it is useful to study periodic Maxwell lattices, like the square and kagome lattices shown in figure 3 with NN bonds and $z = 2d = 4$, and the reduced coordination lattices they spawn when bonds are cut to create free surfaces. They can easily be moved away from the Maxwell limit toward greater rigidity by uniformly [45] or randomly [46] adding further neighbor bonds, and they have an advantage that they lend themselves to exact calculations of elastic response both in the uniform and random systems (via effective medium theory). In addition, in spite of their simplicity, they present a surprisingly rich phenomenology that inform us generally about Maxwell frames.

Much of the language [2, 47, 48, 49] for probing the mechanical properties of frames used in this review was developed by members of the Structural Mechanics group at the University of Cambridge, which provided an elegant generalization of Maxwell's relation based on general principles of linear algebra and used it to deepen our understanding of the more subtle properties of frames. Though well-known in the engineering community, it is less so in the physics and materials science communities. This review will, therefore, begin in section 2 with a fairly comprehensive review of this work. It is followed by five more sections and four appendices. Section 3 deals the long-wavelength elastic limit and how it can be calculated using the developments in references [47, 48]. Section 4 tailors the formalism of the preceding sections specifically to periodic lattices. Section 5 looks in detail at the properties of the three simple lattices in figure 3, and section 6 explores lattices with topologically protected states at interfaces, which are closely related to topologically protected electronic states in the quantum Hall effect [50, 51], polyacetylene [52] and topological insulators [53, 54, 55, 56, 57, 58]. Section 7 presents some final thoughts and speculates about future directions. The four appendices provide mathematical detail and display derivations of various important relations.

Section 5 contains several subsections. Section 5.1 with its simple analytical treatment of the square lattice sets the stage for the study in section 5.2 of the simple kagome lattice. Both lattices have lines of zero modes in their Brillouin zones arising from their having straight sample-traversing filaments of colinear bonds. Section 5.3 then explores how the simple geometrical operation of "twisting" neighboring triangles in the standard kagome lattice [figure 3(c)] to convert it to the twisted lattice [figure 3(d)] gaps the phonon spectrum of the simple kagome lattice at all wavenumbers except at the origin and leads to zero-frequency Rayleigh surface modes [59] not present in either the square or standard kagome lattices.

This review is intended to be as much a pedagogical introduction to periodic Maxwell lattices as an overview of the subject. Except in section 6, which requires the use of some fairly subtle concepts detailed in reference [60], it provides sufficient calculational detail that even someone totally new to the subject should be able to follow it. Though, as the introductory paragraphs have indicated, this review was inspired in part by jamming and rigidity percolation, it is not about these subjects, and they will be considered only when they have direct overlap with the ideas being presented.

2. Generalized Maxwell relation as an index theorem

2.1. The Maxwell rule and states of self stress

Each site in d-dimensions has d independent translational degrees of freedom, and in the absence of constraints on point motion, a collection of N points without connections has $N_{\text{free}} = dN$ zero-frequency displacement modes, which we will refer to as *zero modes*. In the presence of constraints, N_{free} will be less that dN. Each connection reduces the number of zero modes by one. Thus if there are N_B connections and no constraints, there are

$$N_0 = dN - N_B \tag{2.1}$$

zero modes. Of these, $f(d)$ are the trivial ones associated with rigid translations and rotations. Any other zero modes involve internal displacements of the sites and are generally called *mechanisms* [2] in the engineering literature and *floppy modes*
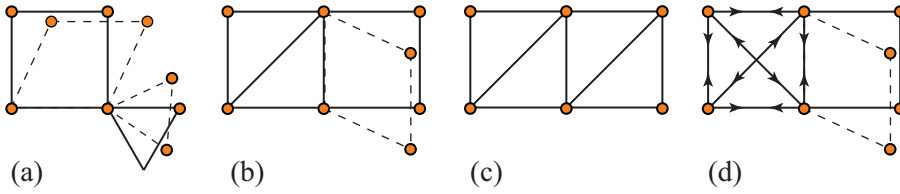
Figure 4. (a) to (c) Frames satisfying the Maxwell rule. (a) has 6 sites, 7 bonds, 5 zero modes, and two mechanisms indicated by the dotted bonds. (b) has 6 sites, 8 bonds, 4 zero modes, and one mechanism. (c) and (d) are constructed from (b) by adding an additional diagonal bond. (c) satisfies the Maxwell rule with only the three trivial zero modes. (d) has 4 zero modes and one state of self stress indicated by the arrows on the bonds in the left square.

in the physics literature [6]. Equation (2.1) reexpressed in terms of the number of mechanisms M is

$$M = dN - N_B - f(d). \tag{2.2}$$

We will refer to Eqs. (2.1) and (2.2) as the *Maxwell count*. A frame is stiff if it has no mechanisms. Setting $M = 0$ yields the Maxwell rule [Eqs. (1.1)]. Figure 4(a) depicts a simple frame that obeys Maxwell's count. It consists $N = 6$ sites and $N_B = 7$ bonds, and it has $N_0 = 2 \times 6 - 7 = 5$ zero modes and $M = N_B = 5 - 3 = 2$ mechanisms.

The simple Maxwell rule does not apply to all frames [2]. Consider the two-square frame with $N = 6$ sites and $N_B = 8$ bonds shown in figure 4(b). It has one mechanism as expected from the Maxwell count. If an extra bond is added, Maxwell's rule would say that the frame is stiff with no mechanisms. The extra bond, however, can be placed as a diagonal in the right square [figure 4(c)] or as an extra diagonal in the left square [figure 4(d)]. In the first case, there are no mechanisms, and Maxwell's rule applies. In the second case, however, the mechanism present before the extra bond was added remains, and the Maxwell count is violated. But the left square with crossed diagonal bonds has an extra *redundant* bond not needed for its rigidity. It also has a new and interesting property: the outer bonds of the square can be placed under tension (compression) and the inner diagonal bonds under compression (tension) such that the net force on all sites is zero. This is a *state of self stress*, which, because of its repeated use in this review, we will usually abbreviate as SSS. This theme can clearly be repeated with each added bond either decreasing the number of zero modes or increasing the number of states of self stress to yield the modified Maxwell count [2]:

$$N_0 = dN - N_B + N_S \qquad \text{or} \qquad N_0 - N_S = dN - N_B, \tag{2.3}$$

where N_S is the number of SSSs. This is an *index theorem* [61, 62] , which we will derive in section 2.2, relating mode and self-stress count to geometric properties of the lattice. We will refer to it simply as the Index theorem .

Two types of mechanisms can be distinguished: "finite" ones in which finite-amplitude displacements of sites stretch no bonds and "infinitesimal" ones in which bond lengths do not change to first order in the magnitude of displacements but do so to second (or higher) order. The Index theorem [2], as we shall show below, follows from the assumption of a linear relation between site displacements and bond lengths, and it treats all displacements as infinitesimal, i.e., it counts both finite and infinitesimal mechanisms but does not identify which is which. Figures 5(a)-(b) show how a finite mechanism can be converted into two infinitesimal mechanisms and one
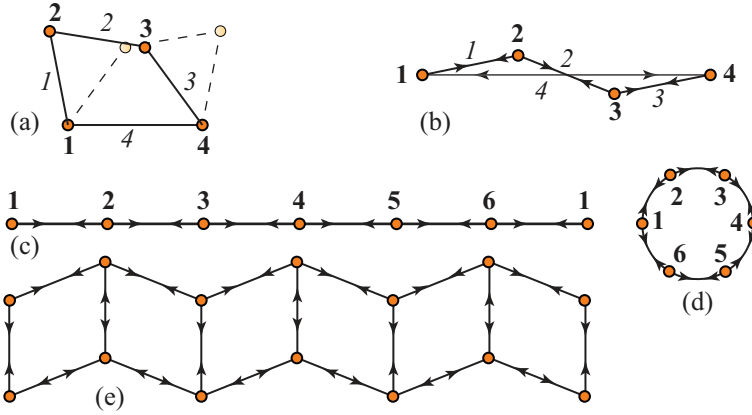
Figure 5. States of self stress: (a) A frame with four sites (**1-4**) and four bonds (italic *1*, *2*, *3*, and *4*) with 4 zero modes and one finite mechanism (dashed lines); (b) A frame in which the length of bond *4* is equal to the sum of the lengths of bonds 1 to 3. Now there is a SSS in which bond *4* is under compression (tension) and the other three are under tension (compression). Both sites **2** and **3** can undergo infinitesimal displacements without changing the length of any bonds, and there are two infinitesimal mechanisms. (c) A line of parallel bonds forming a sample-traversing filament under periodic boundary conditions as depicted in (d). The forces on all sites are zero if all of the bonds are under equal tension or compression, and there is one SSS . (e) A zigzag ladder under periodic boundary conditions with one SSS .

SSS. A configuration of self-stress that is particularly important for the current study is any straight line of bonds under periodic boundary conditions, which we will refer to as straight *filaments*, as shown in figures 5(c)-(d). Changing the straight filament to a zigzagged one removes this state of self stress. On the other hand the "zigzaging" periodic ladder configuration shown in figure 5(e) has one SSS, rather than the two that a straight ladder would have. Tensions alternate in sign from bond to bond in this SSS, a property, which will be important in what follows, that prevents it from having any zero wave-number component.

A system in which there are neither any mechanisms ($M = 0$) nor any states of self-stress ($N_S = 0$) is *isostatic* . A finite isostatic system necessarily satisfies the Maxwell relation $z = z_c^N$, but a system with $z = z_c^N$ can have any number of mechanisms provided it is equal to the number of SSSs. The distinction between satisfying the Maxwell rule and being isostatic is often lost in the literature, and it is common practice to refer to any system that satisfies Maxwell's rule as isostatic. In this review, we will keep the distinction, referring to any free frame satisfying Maxwell's rule as a Maxwell frame, reserving the term isostatic for those free Maxwell frames satisfying $M = N_S = 0$. As we shall see in section 3.3, the extension of this definition to periodic frames presents some problems [49]. Since the term isostatic has become so prevalent, we propose in that section a definition of this term that is in the spirit of the definition for free frames and consistent with common usage for periodic frames.

2.2. Equilibrium and compatibility matrices

In the absence of external forces, the equilibrium force at each site in a frame is determined by the tensions in the bonds it shares with other sites. This is true whether or not the site is in mechanical equilibrium; if the force at a site is nonzero, the mass at that site will accelerate according to Newton's laws. If forces at sites arising from bond tensions are nonzero, they can be balanced by external loads to create an equilibrium situation in which the total force on each site is zero. Clearly, in mechanical equilibrium, the external loads are the negative of the forces at each site arising from bond tensions.

For central forces, the tension in a bond is parallel to the bond. Thus its direction is specified by bond orientation, but its magnitude and sign can vary. Let F be a vector in the dN-dimensional space, V_F, of the d components of force at each site on the lattice exerted by tensions in the bonds that terminate on it, and let T be a vector in the N_B-dimensional space, V_T, of the of the bond tensions, which are scalars of either sign. External loads at sites are represented by the dN-dimensional vector L. In equilibrium when sites do not accelerate (or move if there is external friction), $\mathsf{L} = -\mathsf{F}$. Since the relation between forces and tensions is linear, there is a $dN \times N_B$ dimensional matrix Q (with dN rows and N_B columns), called the *equilibrium* matrix, that maps V_T to V_F:

$$\mathsf{Q}\,\mathsf{T} = -\mathsf{F} = \mathsf{L}, \qquad (2.4)$$

where the final relation only applies in static situations.

The null space or kernel of Q, $\ker(\mathsf{Q})$ of dimension $\mathrm{nullity}(\mathsf{Q})$, is the set of all vectors mapped to the zero vector. Any vector in the null space of Q represents a state of self stress because it corresponds to tensions on a set of bonds for which the forces on all sites are zero. Thus $\mathrm{nullity}(\mathsf{Q})$ is equal to the number of SSSs N_S. Vectors T not mapped into the null space of Q are in the *orthogonal complement*, $\mathrm{OC}(\mathsf{Q})$, of $\ker(\mathsf{Q})$. The dimension of $\mathrm{OC}(\mathsf{Q})$ is equal the to the rank of Q. The rank-nullity theorem of linear algebra [63] relates the rank and nullity of a matrix to its column dimension:

$$\mathrm{rank}(\mathsf{Q}) + \mathrm{nullity}(\mathsf{Q}) = \mathrm{rank}(\mathsf{Q}) + N_S = N_B. \qquad (2.5)$$

Elongation of bonds are determined by the displacements of the sites to which they are attached. The elongations of individual bonds are necessarily parallel to bond vectors for central forces. Let U be a vector in the dN-dimensional space, V_U, of site displacements and E be a vector in the N_B-dimensional space, V_E, of bond elongations. The $N_B \times dN$-dimensional compatibility matrix C maps V_U to V_E:

$$\mathsf{C}\,\mathsf{U} = \mathsf{E}. \qquad (2.6)$$

The null space of C is the set of displacements U that do not change the length of bonds, i.e., the set of zero modes of the system; thus, $\mathrm{nullity}(\mathsf{C}) = N_0$. The rank-nullity theorem applied to C yields

$$\mathrm{rank}(\mathsf{C}) + \mathrm{nullity}(\mathsf{C}) = \mathrm{rank}(\mathsf{C}) + N_0 = dN. \qquad (2.7)$$

The equilibrium and compatibility matrices are not independent: they are matrix transposes of each other. To see this, we can calculate the work done under infinitesimal distortions of the system in the presence of sites forces (and thus necessarily tensions in the bonds) in two ways: First the work W_L done by external

loads in displacing sites and second the work W_T done by bond tensions in stretching bonds. The two calculations must yield the same result:

$$W_L = \mathsf{L}^T \mathsf{U} = \mathsf{T}^T \mathsf{Q}^T \mathsf{U} = W_T = \mathsf{T}^T \mathsf{E} = \mathsf{T}^T \mathsf{C} \mathsf{U}, \tag{2.8}$$

where the superscript T refers to the transpose of a matrix. Since this relation is valid for all U (even U in the null space of C) it must be that $\mathsf{C} = \mathsf{Q}^T$. The rank of a matrix is equal to the rank of its transpose, $\operatorname{rank}(\mathsf{Q}) = \operatorname{rank}(\mathsf{C})$, and subtracting (2.5) from (2.7) yields the Index theorem of (2.3). The equilibrium and compatibility matrices have proven useful in many contexts, and we mention only one in which frames with spring lengths that do not correspond to the length of the bonds they occupy are constructed from frames in which they do [64].

To construct Q and C for a particular frame, it is necessary to have explicit representations for the vectors U, E, T, and F. A frame consists of N sites labeled $s = 1, ..., N$ at equilibrium positions $\boldsymbol{R}(s)$ connected by N_B bonds labeled $\beta = 1, ..., N_B$. Under frame distortions, site positions change to

$$\boldsymbol{X}(s) = \boldsymbol{R}(s) + \boldsymbol{u}(s), \tag{2.9}$$

where $\boldsymbol{u}(s)$ with components $u_i(s)$, $i = 1, ..., d$, is the displacement vector at site s. The force at site s is $\boldsymbol{f}(s) = (f_1(s), ... f_d(s))$, and the dN-dimensional displacement and force vectors are, respectively, $\mathsf{U} = (\boldsymbol{u}_1, ..., \boldsymbol{u}_N)$ and $\mathsf{F} = (\boldsymbol{f}_1, ..., \boldsymbol{f}_N)$.

Each bond $\beta = [s_\beta, s'_\beta]$ connects a pair of sites s_β and s'_β, whose separation in the equilibrium frame is the vector

$$\boldsymbol{b}(\beta) \equiv \boldsymbol{b}([s_\beta, s'_\beta]) = \boldsymbol{R}(s'_\beta) - \boldsymbol{R}(s_\beta) \equiv b_\beta \hat{\boldsymbol{b}}_\beta, \tag{2.10}$$

from s_β to s'_β, where b_β is the length of bond β and $\hat{\boldsymbol{b}}_\beta$ is the unit vector along bond β. The arrows in figure 1(b) show an arbitrarily chosen choice of directions of vectors $\hat{\boldsymbol{b}}_\beta$ for bonds in a simple frame. Other choices will lead to different equations relating forces to tensions but will not affect the physical tensions in the frame. Let the tension in bond β be t_β, and associate with that bond a vector tension,

$$\boldsymbol{t}_\beta = t_\beta \hat{\boldsymbol{b}}_\beta. \tag{2.11}$$

With this convention, the force exerted on sites s_β and s'_β by bond $[s_\beta, s'_\beta]$ are, respectively, $\boldsymbol{t}_\beta$ and $-\boldsymbol{t}_\beta$, or, equivalently, the force on a site s from a bond β that it shares with another site is $\boldsymbol{t}_\beta$ if $\hat{\boldsymbol{b}}_\beta$ points away from the site and $-\boldsymbol{t}_\beta$ if it points toward the site. With these definitions, we can construct the compatibility matrix from the the bond elongation relations,

$$e_\beta = \hat{\boldsymbol{b}}_\beta \cdot (\boldsymbol{u}(s'_\beta) - \boldsymbol{u}(s_\beta)), \tag{2.12}$$

and the equilibrium matrix from the site force equations,

$$\boldsymbol{f}(s) = \sum_{\beta=1}^{z_s} \operatorname{sign}(\beta) \boldsymbol{t}_\beta, \tag{2.13}$$

where z_s is the number of bonds site s shares with its neighbors and $\operatorname{sign}(\beta) = +1(-1)$ if the arrow of bond β points away from (toward) site s.

It is instructive to carry out explicit calculations of Q and C for a simple frame. We consider the frame shown in figure 1(b) with $N = 4$, $N_B = 5$ and $2N - N_B = 3$, the number of modes of rigid translation and rotation. This frame has no floppy modes and no state of self stress, and it is isostatic. The figure labels sites $(s = 0, ..., 3)$, bonds $(\beta = 1, ..., 5)$, and bond directions. The five displacement-elongation equations are

$$e_1 = \hat{\boldsymbol{b}}_1 \cdot (\boldsymbol{u}_1 - \boldsymbol{u}_0) \qquad e_2 = \hat{\boldsymbol{b}}_2 \cdot (\boldsymbol{u}_2 - \boldsymbol{u}_1) \qquad e_3 = \hat{\boldsymbol{b}}_3 \cdot (\boldsymbol{u}_2 - \boldsymbol{u}_3)$$
$$e_4 = \hat{\boldsymbol{b}}_4 \cdot (\boldsymbol{u}_3 - \boldsymbol{u}_0) \qquad e_5 = \hat{\boldsymbol{b}}_5 \cdot (\boldsymbol{u}_3 - \boldsymbol{u}_1), \tag{2.14}$$

and the four vector force equations are

$$\boldsymbol{f}_0 = \boldsymbol{t}_1 + \boldsymbol{t}_4 \qquad\qquad \boldsymbol{f}_1 = -\boldsymbol{t}_1 + \boldsymbol{t}_2 + \boldsymbol{t}_5$$
$$\boldsymbol{f}_2 = -\boldsymbol{t}_2 - \boldsymbol{t}_3 \qquad\qquad \boldsymbol{f}_3 = \boldsymbol{t}_3 - \boldsymbol{t}_4 - \boldsymbol{t}_5. \tag{2.15}$$

The 8×5 compatibility and 5×8 equilibrium matrices are easily constructed from equations (2.14) and (2.15). If, however, we are interested only in internal deformations of the frame and not its uniform translations and rotations, we can apply three constraints to the motion, most easily by pinning site 0 so that $\boldsymbol{u}_0 = 0$ and placing site 1 on a horizontal rail as shown in figure 1(a) to fix $u_{1,y} = 0$ so that $N_{\text{free}} = 5$. We also allow $\boldsymbol{f}_0$ and $f_{1,x}$ to take on whatever values needed to satisfy the constraints, so they do not enter into our equations. This leaves us with a 5×5 compatibility matrix,

$$\mathsf{C} = \begin{pmatrix} 1 & 0 & 0 & 0 & 0 \\ -\frac{1}{2} & \frac{1}{2} & \frac{\sqrt{3}}{2} & 0 & 0 \\ 0 & 1 & 0 & -1 & 0 \\ 0 & 0 & 0 & \frac{1}{2} & \frac{\sqrt{3}}{2} \\ \frac{1}{2} & 0 & 0 & -\frac{1}{2} & \frac{\sqrt{3}}{2} \end{pmatrix}, \tag{2.16}$$

mapping $\mathsf{U} = (u_{1,x}, u_{2,x}, u_{2y}, u_{3,x}, u_{3,y})$ to $\mathsf{E} = (e_1, e_2, e_3, e_4, e_5)$. The equilibrium matrix, mapping $\mathsf{T} = (t_1, t_2, t_3, t_4, t_5)$ to $\mathsf{L} = -\mathsf{F} = -(f_{1,y}, f_{2,x}, f_{2,y}, f_{3,x}, f_{3,y})$ constructed from Eq. (2.15), is trivially equal to C^T. Both Q and C are square invertible matrices: their nullspaces are empty, both $N_0 = 0$ and $M = 0$, and the system is isostatic as required. Thus, the tensions on the bonds are uniquely determined by the forces on the sites and vice versa: the frame is *statically determinate*. And the elongations of the bonds are uniquely determined by the site displacements and vice versa: the frame is *kinematically determinate*. Thus, an alternative, and perhaps preferable, definition of an isostatic frame is that it be both statically and kinematically determinate. Another way of dealing with the trivial zero modes is to introduce "reaction forces" to yield 8×8 matrices Q and C.

2.3. The dynamical matrix

So far, we have only discussed tensions and stretches of bonds without specifying any relation among them. In our "ball-and-spring" frames, each bond β is occupied by a Hooke's law spring whose energy is half its spring constant k_b times the square of its elongation. Let k be the $N_B \times N_B$ diagonal matrix of spring constants, then the elastic energy of the lattice is

$$V_{\text{el}} = \frac{1}{2} \mathsf{E}^T \mathsf{k} \mathsf{E} = \frac{1}{2} \mathsf{U}^T \mathsf{K} \mathsf{U}, \tag{2.17}$$

where

$$\mathsf{K} = \mathsf{Q}\mathsf{k}\mathsf{Q}^T = \mathsf{C}^T\mathsf{k}\mathsf{C} \tag{2.18}$$

is the $dN \times dN$ *stiffness* matrix. Normal-mode frequencies depend on mass as well as the stiffness matrix. The kinetic energy requires the introduction of a mass matrix M. We will restrict our attention of frames in which the mass of all mass points is equal to m, in which case $\mathsf{M} = m\,\mathsf{I}$, where I is the unit matrix, and the kinetic energy is

$$E_{\text{kin}} = \tfrac{1}{2}m\dot{\mathsf{U}}^T\dot{\mathsf{U}}, \tag{2.19}$$

where $\dot{\mathsf{U}}$ is the velocity vector. Normal modes are then eigenvectors of the *dynamical* matrix:

$$\mathsf{D} = \tfrac{1}{m}\mathsf{K}. \tag{2.20}$$

The Lagrangian in the presence of eternal loads is thus

$$L = \tfrac{1}{2}m\dot{\mathsf{U}}^T\dot{\mathsf{U}} - V_{\text{el}} - \mathsf{U}^T\mathsf{L}, \tag{2.21}$$

and the equation of motion is

$$m\ddot{\mathsf{U}} = -\frac{\partial V_{\text{el}}}{\partial \mathsf{U}^T} - \mathsf{L} = -\mathsf{K}\mathsf{U} - \mathsf{L} = \mathsf{F} - \mathsf{L}, \tag{2.22}$$

which vanishes when the external load L is equal to the force $\mathsf{F} = -\mathsf{K}\mathsf{U} = -\mathsf{Q}\mathsf{T}$ exerted by bond stretching. Note that the equilibrium matrix can be used to calculate F whether or not the system is in static equilibrium or not. On the other hand $\mathsf{L} = \mathsf{Q}\mathsf{T}$ only in equilibrium when there is no acceleration (assuming no friction forces).

3. The elastic limit

3.1. Strain and the elastic energy

Strain is a measure of macroscopic distortions of an elastic medium. The macroscopic deformation tensor $\boldsymbol{\lambda} = \boldsymbol{I} + \boldsymbol{\eta}$, where $\boldsymbol{I}$ is the unit tensor, determines displacements at boundary sites s_B of either a finite sample or the periodic box under periodic boundary conditions:

$$\boldsymbol{X}(s_B) = \boldsymbol{\lambda}\boldsymbol{R}(s_B), \text{ or } \boldsymbol{u}(s_B) = \boldsymbol{\eta}\,\boldsymbol{R}(s_B), \tag{3.1}$$

and the macroscopic strain tensor is

$$\boldsymbol{\varepsilon} = \tfrac{1}{2}(\boldsymbol{\lambda}^T\boldsymbol{\lambda} - \boldsymbol{I}) = \tfrac{1}{2}(\boldsymbol{\eta} + \boldsymbol{\eta}^T + \boldsymbol{\eta}^T\boldsymbol{\eta}) \approx \tfrac{1}{2}(\boldsymbol{\eta} + \boldsymbol{\eta}^T), \tag{3.2}$$

where the final form is the linearized limit, which is all that concerns us here.

The elastic energy density associated with the macroscopic strain is

$$f_{\text{el}} = \tfrac{1}{2}K_{ijkl}\varepsilon_{ij}\varepsilon_{kl}, \tag{3.3}$$

where K_{ijkl} is the elastic constant tensor and the Einstein convention on repeated indices is understood. The elastic strain ε_{ij}, (3.2), is symmetric and has $a_d = d(d+1)/2$ independent components in d dimensions. It can be expressed [65, 66] as an a_d-dimensional vector (Voigt notation), which in two dimensions takes the form,

$$\boldsymbol{\varepsilon}_V = (\varepsilon_{xx}, \varepsilon_{yy}, \varepsilon_{xy}). \tag{3.4}$$

The elastic tensor is then an $a_d \times a_d$ matrix, which in two dimension is

$$\mathbb{K} = \begin{pmatrix} K_{xxxx} & K_{xxyy} & 2K_{xxxy} \\ K_{xxyy} & K_{yyyy} & 2K_{yyxy} \\ 2K_{xxxy} & 2K_{yyxy} & 4K_{xyxy} \end{pmatrix} \xrightarrow{\text{isotropic}} \begin{pmatrix} B+G & B-G & 0 \\ B-G & B+G & 0 \\ 0 & 0 & G \end{pmatrix}, \qquad (3.5)$$

where the final form is the isotropic limit, where $B = \lambda + \mu$ is the bulk modulus and $G = \mu$ is the shear modulus with λ and μ the standard Lamé coefficients [59]. The linearized Cauchy stress tensor is

$$\sigma_{ij} = K_{ijkl}\varepsilon_{kl}. \qquad (3.6)$$

Mechanical stability requires that all a_d eigenvalues of the Voigt elastic matrix $\mathbb{K}$ be positive. Thus the elastic energy of an elastically stable system can be expressed as a sum of squares of a_d independent linear combinations of strains (the eigenvectors of the elastic matrix) with positive coefficients (the eigenvalues of the elastic matrix). We shall see shortly that some or all of the eigenvalues of the elastic matrix in lattices at or near the Maxwell limit may be zero.

3.2. Elastic limit and States of Self Stress

Calculations of the elastic tensor require some method of maintaining strain. The usual picture is that boundary sites of a finite frame are clamped to conform with (3.1). Since these sites are fixed, their displacements and the forces associated with them do not enter the calculation of Q and C. An alternative approach, which we implement, is to apply periodic boundary conditions (PBCs) to the frame, which may or may not be composed of repeated unit cells. In this approach, it is the boundaries of the periodic cell that satisfy (3.1).

If the positions of all sites, rather than just boundary sites, displace according to Eq. (3.1), the elastic distortion is *affine*. Under such distortions, the relative displacement of the sites associated with bond β is

$$\boldsymbol{u}(s'_\beta) - \boldsymbol{u}(s_\beta) = \boldsymbol{\eta}\left(\boldsymbol{R}(s'_\beta) - \boldsymbol{R}(s_\beta)\right) = \boldsymbol{\eta}\,\boldsymbol{b}_\beta, \qquad (3.7)$$

and the affine stretch of bond β is

$$e_\beta^{\text{aff}} = \hat{\boldsymbol{b}}_\beta^T\,\boldsymbol{\lambda}\,\boldsymbol{b}_\beta = \hat{b}_{\beta,i}\varepsilon_{ij}b_{\beta,j}, \qquad (3.8)$$

where we used the fact that $\hat{b}_{\beta,i}b_{\beta,j}$ is symmetric in i and j to convert $\boldsymbol{\eta}$ to $\boldsymbol{\varepsilon}$ in the linearized limit. The affine elastic energy density is then

$$f_{\text{el}}^{\text{aff}} = \frac{1}{2V}\,\mathsf{E}_{\text{aff}}^T\,\mathsf{k}\,\mathsf{E}_{\text{aff}}, \qquad (3.9)$$

where V is the volume and E_{aff} is the vector of affine elongations e_β^{aff}.

Affine response throughout a sample is the exception rather than the rule. It is guaranteed to occur in absolutely homogeneous systems and in lattices with one site per unit cell, but it can occur in certain other systems with special relations among elastic constants or special arrangements of sites in periodic systems with multi-site unit cells (for example, as we shall see, in the kagome lattice). Generally, however, the forces at at least some sites under an affine strain imposed by macroscopic stain at the boundary are nonzero, and these sites will relax to positions of zero force

(or equivalently until the energy reaches its minimum value), in which cases their displacements are nonaffine. In Appendix A, we show that the result of this relaxation is that the elastic energy density becomes [48, 47, 67]

$$f_{\mathrm{el}} = \frac{1}{2V} \mathsf{E}_{\mathrm{aff},s}^T [(\mathsf{k}^{-1})_{ss})]^{-1} \mathsf{E}_{\mathrm{aff},s} \xrightarrow{\mathsf{k} \to k\mathsf{I}} \frac{k}{2V} \sum_\alpha (\mathsf{E}_{\mathrm{aff}} \cdot \hat{\mathsf{t}}_\alpha)^2 \qquad (3.10)$$

where $\mathsf{E}_{\mathrm{aff},s}$ and $(\mathsf{k}^{-1})_{ss}$ are the projections of $\mathsf{E}_{\mathrm{aff}}$ and k^{-1} onto $\ker(\mathsf{Q})$, and $\hat{\mathsf{t}}_\alpha$ is the αth orthonormal basis vector of $\ker(\mathsf{Q})$. Thus, only the projections of the affine displacement vectors onto states of self-stress contribute to the elastic energy.

Equation (3.10) encodes a great deal of information.

- First, it shows that lattices cannot be elastically stable unless they have SSSs in the presence of conditions that constrain the macroscopic strain - a simple reflection of the fact that forces on each site must be zero once equilibrium is reached in the presence of imposed strains, which necessarily induce bond tension.

- Second, only those states of self-stress with a nonzero overlap with the affine bond elongations contribute to the elastic energy. These states necessarily traverse the sample, and they are *load-bearing*. The straight filament of figure 5(c) (wound to a circle - figure 5(d)), whose bonds all have the same sign of tension provides an example of a load-bearing state, whereas the zigzag state of figure 5(e) and the localized crossed square of figure 4(d) does not.

- Third, because it is a sum of squares of linear combinations of strain, it shows that there must be at least $a_d = d(d+1)/2$ load-bearing SSSs to produce an elastically stable system with an elastic matrix with a_d positive eigenvalues.

3.3. Isostaticity and periodic boundary conditions

In section 2.1, isostatic lattices were defined as ones that are both kinematically ($N_0 = f(d)$) and statically determinate ($N_S = 0$). This definition is unambiguous for finite free frames. It would seem natural to define an isostatic frame under PBCs in the same way, but there is a problem with this definition [49]. Under PBCs, the shape and size of the frame boundary is fixed; the compatibility matrix (and by extension, the equilibrium matrix) applies to displacements and does not apply to changes in the shape or size of the periodic boundary [68, 34, 35], which are described by macroscopic strain. In order for a lattice to be elastically stable, it must have at least $d(d+1)/2$ SSSs. Reference [49] defines a lattice under PBCs to be statically determinate if $N_S = d(d+1)/2$ and kinematically determinate if $N_0 = d$, but it does not propose applying the terms *isostatic* to such systems. We propose calling a frame under PBCs isostatic if $N_0 = d$ and N_S lies between 1 and $d(d+1)/2$. This corresponds more or less to common usage in the jamming literature. If greater precision is required, the value of N_S can be specified via the term N_S-isostatic.

The above discussion applies to any frame, whether it is a lattice with unit cells on a Bravais lattice or not, and in particular to finite-frame approximations to infinite random systems such as those encountered studies of jamming. These frames can be subjected to PBCs by wrapping them on a torus to create a single cell in which sites separated by repeat distances of the torus are identified. We will refer to these as toroidal PBCs. Since there is only one cell with randomly placed sites, there is no wavenumber $\boldsymbol{q}$ to index the dN vibrational states. Alternatively, the single (large) cell can be periodically repeated in a Bravais lattice, in which case there are dN vibrational

bands with wave-number-dependent frequencies. The $\boldsymbol{q} = 0$ limit of these bands are the vibrational states under the toroidal PBCs and are generally the ones of physical interest, though interesting information about the stability of jammed structures can be obtained from an examination of spectrum at $\boldsymbol{q} \neq 0$ [40].

Lattices under periodic boundary conditions are special. They consist of N_c periodically repeated unit cells with n sites and n_b bonds, and the Index theorem reads $N_0 - N_S = (dn - n_b)N_c$. In a periodic Maxwell lattice, $n_b = dn$, and $N_0 = N_S$. Thus if N_0 has its minimum value of d, $N_S = d$, and under the definition proposed above, such a lattice would be isostatic. It is impossible to have $N_0 = d$ and for N_S to have any other value than d in the interval between 1 and $d(d + 1)/2$ because a change in N_S requires a change in n or n_b and thus of $dn - n_b$, which would lead to a change in $N_0 - N_S$ of order $N_c \gg 1$ rather than of order one. Thus we can uniquely define an *isostatic periodic lattice under* PBCs to be one with $N_0 = N_S = d$.

Finite frames can be constructed from ones subjected to PBCs by cutting bonds along the periodic boundaries and "liberating" the sites attached to them. Since opposite sides of the boundary are equivalent, it is only necessary to cut bonds along half of the boundary to liberate a full free lattice. Thus, an $N_x \times N_y$ free square lattice is obtained by cutting $N_x + N_y$ bonds in the lattice under PBCs. The cutting process thus reduces the number of bonds by of order $N^{(d-1)/d}$ in a lattice of N sites in d dimensions and increases $N_0 - N_S$ by the same amount. If the periodic lattice is isostatic, then there are necessarily of order $N^{(d-1)/d}$ extra zero modes in the finite lattice. If on the other hand, the lattice under PBCs has of order $N^{(d-1)/d}$ SSSs that are removed on cutting, there may be no increase in zero modes at all upon cutting.

4. Periodic Lattices

Our primary interest is in periodic lattices, and we review here notation that we will use to describe them.

4.1. Notation

A general lattice has N_c unit cells consisting of n sites and n_b bonds so that the total number of sites and bonds are, respectively, $N = N_c n$ an $N_B = N_c n_b$. The Bravais lattice vectors $\boldsymbol{R}_\ell$, where $\ell = (l_1, \cdots l_d)$ with each l_i an integer, are linear combinations of the primitive translation vectors $\boldsymbol{a}_j$, $j = 1, \cdots d$:

$$\boldsymbol{R}_\ell = \sum_j^d l_j \boldsymbol{a}_j. \tag{4.1}$$

The positions of sites and bonds in cell ℓ in the undistorted lattice with a basis are

$$\begin{aligned} \boldsymbol{R}_{\ell,\mu} &= \boldsymbol{R}_\ell + \boldsymbol{r}_\mu, & \mu &= 1, \cdots, n \\ \boldsymbol{R}_{\ell,\beta} &= \boldsymbol{R}_\ell + \boldsymbol{r}_\beta, & \beta &= 1, \cdots, n_b, \end{aligned} \tag{4.2}$$

where $\boldsymbol{r}_\mu$ and $\boldsymbol{r}_\beta$ are, respectively the positions of the sites and bonds relative to the origin of the unit cell. The positions of lattice sites in a distorted lattice are

$$\boldsymbol{X}_{\ell,\mu} = \boldsymbol{R}_{\ell,\mu} + \boldsymbol{u}_\mu(\ell), \tag{4.3}$$

where $\boldsymbol{u}_\mu(\ell)$ with Cartesian components $u_{\mu,i}(\ell) \equiv u_\sigma(\ell)$ is the displacement vector of site (ℓ, μ). The components of U are thus the dN displacements $u_\sigma(\ell)$. The Cartesian

components $f_\sigma(\ell)$ of the force vector $\boldsymbol{f}_\mu(\ell)$ are the dN components of F. The N_B bond elongations $e_\beta(\ell)$ and bonds tensions $t_\beta(\ell)$ are the components of the of E, and T, respectively. Fourier transforms in periodic lattices are defined in the usual way in terms of wavenumbers $\boldsymbol{q}$ in the first Brillouin zone:

$$\boldsymbol{u}_\mu(\ell) = \frac{1}{N_c} \sum_{\boldsymbol{q}} e^{i\boldsymbol{q}\cdot(\boldsymbol{R}_\ell+\boldsymbol{r}_\mu)} \boldsymbol{u}_\mu(\boldsymbol{q}), \qquad \boldsymbol{u}_\mu(\boldsymbol{q}) = \sum_\ell e^{-i\boldsymbol{q}\cdot(\boldsymbol{R}_\ell+\boldsymbol{r}_\mu)} \boldsymbol{u}_\mu(\ell) \qquad (4.4)$$

$$t_\beta(\ell) = \frac{1}{N_c} \sum_{\boldsymbol{q}} e^{i\boldsymbol{q}\cdot(\boldsymbol{R}_\ell+\boldsymbol{r}_\beta)} t_\beta(\boldsymbol{q}) \qquad t_\beta(\boldsymbol{q}) = \sum_\ell e^{-i\boldsymbol{q}\cdot(\boldsymbol{R}_\ell+\boldsymbol{r}_\beta)} t_\beta(\ell), \qquad (4.5)$$

and similarly for $\boldsymbol{f}_\mu$, e_β and other site and bond variables. These quantities can also be defined without the site and bond basis vectors, $\boldsymbol{r}_\mu$ and $\boldsymbol{r}_\beta$ in the exponentials, and we will usually leave them out. They will, however, be of use in our discussion of topological states in section 6. The components of the equilibrium matrix Q in periodic lattices are $\mathbf{Q}_{\sigma,\beta}(\ell,\ell')$. Its Fourier transform is

$$\mathbf{Q}_{\sigma\beta}(\boldsymbol{q}) = \sum_\ell e^{-i\boldsymbol{q}\cdot(\boldsymbol{R}_{\ell,\sigma}-\boldsymbol{R}_{0,\beta})} \mathbf{Q}_{\sigma\beta}(\ell,0). \qquad (4.6)$$

Again, the basis vectors in the exponents are not required. The compatibility matrix is $\mathbf{C}(\boldsymbol{q}) = \mathbf{Q}^\dagger(\boldsymbol{q})$.

With these definitions, we can reexpress equations (2.4) and (2.6) as

$$\mathbf{Q}(\boldsymbol{q})\,\mathbf{t}\,(\boldsymbol{q}) = -\mathbf{f}(\boldsymbol{q}) \qquad \mathbf{C}\,(\boldsymbol{q})\,\mathbf{u}(\boldsymbol{q}) = \mathbf{e}(\boldsymbol{q}), \qquad (4.7)$$

where the "bold roman" vectors are defined as $\mathbf{t}(\boldsymbol{q}) = (t_1(\boldsymbol{q}), ..., t_{n_b}(\boldsymbol{q}))$ and $\mathbf{u}(\boldsymbol{q}) = (\boldsymbol{u}_1(\boldsymbol{q}), ..., \boldsymbol{u}_n(\boldsymbol{q}))$ and similarly for $\mathbf{e}(\boldsymbol{q})$ and $\mathbf{f}(\boldsymbol{q})$, and $\mathbf{Q}(\boldsymbol{q})$ is the $dn \times n_b$ matrix with components $\boldsymbol{Q}_{\sigma\beta}(\boldsymbol{q})$. There is one equation for each of the N_c values of $\boldsymbol{q}$, giving us as many independent equations as (2.4) and (2.6). The Index theorem applies to these equations for each $\boldsymbol{q}$:

$$n_0(\boldsymbol{q}) - n_s(\boldsymbol{q}) = dn - n_b, \qquad (4.8)$$

where $n_0(\boldsymbol{q}) = \text{nullity}(\mathbf{C})$ is the number of zero modes and $n_s(\boldsymbol{q}) = \text{nullity}(\mathbf{Q})$ is the number of states of self stress at wavevector $\boldsymbol{q}$. Of course, $N_0 = \sum_{\boldsymbol{q}} n_0(\boldsymbol{q})$ and $N_S = \sum_{\boldsymbol{q}} n_s(\boldsymbol{q})$.

In periodic Maxwell lattices, $dn = n_b$, and there are exactly as many zero modes as states of self stress at each $\boldsymbol{q}$. Under PBCs, there are always d zero modes that arise from translational invariance, and these are necessarily at $\boldsymbol{q} = 0$, implying that there are at least d SSSs at $\boldsymbol{q} = 0$. There may be more, but each additional SSS will require an additional zero mode, which is a $\boldsymbol{q} = 0$ mechanism. At nonzero $\boldsymbol{q}$, there is no general reason for zero modes to exist, but if they do, the are necessarily accompanied by SSSs. We will see that this is a common theme in our study of specific lattices in section 5: removing states of self stress eliminates zero modes and "gaps" the phonon spectrum.

Following (2.17), the potential energy in terms of a periodic harmonic lattice is

$$V_{\text{el}} = \frac{1}{2N_c} \sum_{\boldsymbol{q}} \mathbf{e}^\dagger(\boldsymbol{q})\,\mathbf{k}\,\mathbf{e}(\boldsymbol{q}) = \frac{1}{2N_c} \sum_{\boldsymbol{q}} \mathbf{u}^\dagger(\boldsymbol{q})\mathbf{K}(\boldsymbol{q})\mathbf{u}(\boldsymbol{q}), \qquad (4.9)$$

where $\mathbf{k}$ is the $n_b \times n_b$ diagonal matrix of spring constants, and

$$\mathbf{K}(\boldsymbol{q}) = \mathbf{Q}(\boldsymbol{q})\,\mathbf{k}\,\mathbf{Q}^\dagger(\boldsymbol{q}) \equiv m\mathbf{D}(\boldsymbol{q}) \qquad (4.10)$$

is the stiffness matrix. We will usually set $m = 1$ so that the stiffness matrix $\mathbf{K}$ and the dynamical matrix $\mathbf{D}$ are the same. In periodic systems, nearest-neighbor (NN), next-nearest neighbor (NNN), and further-neighbor bonds are well defined, and bond vectors can be expressed as the direct sum of NN and NNN components, e.g. $\mathbf{e} = \mathbf{e}_{NN} \oplus \mathbf{e}_{NNN}$, and elastic constant matrix and dynamical matrices can be decomposed into NN and NNN:

$$\mathbf{D}(\boldsymbol{q}) = \mathbf{D}_{NN}(\boldsymbol{q}) + \mathbf{D}_{NNN}(\boldsymbol{q}). \tag{4.11}$$

4.2. The elastic limit

4.2.1. The elastic energy Under affine strain, the strain of equivalent bonds in different unit cells are identical, and we can describe affine strain in terms of the n_b dimensional vector $\mathbf{e}_{\text{aff},s}$. As a result, the elastic energy depends only on the projection of the affine strain onto the $\boldsymbol{q} = 0$ SSSs. Following (3.10) and Appendix A, the elastic energy density is thus

$$f_{\text{el}} = \frac{1}{2v_c} \mathbf{e}_{\text{aff},s}^T (\mathbf{k}_{ss}^{-1})^{-1} \mathbf{e}_{\text{aff},s} \rightarrow \frac{1}{2v_c} k \sum_\alpha (\mathbf{e}_{\text{aff}} \cdot \hat{\mathbf{t}}_\alpha)^2, \tag{4.12}$$

where $v_c = N_c/V$ is the volume of a unit cell and $\mathbf{k}_{ss}$ is the projection of the $\mathbf{k}$ on to the nullspace of $\mathbf{Q}(\boldsymbol{q} = 0)$. The final form with $\hat{\mathbf{t}}_\alpha$ ($\alpha = 1, ..., n_s(0)$) basis vectors for the null space of $\mathbf{Q}(\boldsymbol{q} = 0)$ applies when there is a single spring constant k.

Equation (4.12) constrains the elastic energy of *Maxwell* lattices, which depends on the number, m_0, of $\boldsymbol{q} = 0$ mechanisms and on the overlap of $\boldsymbol{q} = 0$ SSSs with the $\boldsymbol{q} = 0$ affine bond elongation $\mathbf{e}_{\text{aff}}$. Consider periodic Maxwell lattices, for which with $N_0 = N_S$.

(i) $m_0 = 0$: In this case, there are exactly d zero modes and exactly d SSSs. There are now two possibilities:

   (a) All d SSSs have a nonzero overlap with the affine bond elongations, and the elastic matrix (3.5) then has d positive and $d(d + 1)/2 - d = d(d - 1)/2$ zero eigenvalues, which correspond to zero-energy elastic deformations, now referred to as Guest modes [49]. This case corresponds to what we call an isostatic periodic lattice. As we shall see, this is the situation for the square, twisted kagome, and topological kagome lattices [section 6.2] in which there are two positive eigenvalues and one zero-energy elastic mode.

   (b) Fewer than d SSSs have a nonzero overlap with affine bond elongations, and as a result there are fewer than d positive eigenvalues to the elastic matrix and more than $d(d - 1)/2$ zero-energy elastic distortions. The zigzagged square lattice to be discussed in section 5.4 provides an example of this behavior. Finite periodic approximates to infinite-unit cell systems, such as packed spheres at the jamming transition [34, 35] and randomized quasi-crystalline Penrose tilings [section 5.4] [69] exhibit smaller and smaller overlap as the order of the approximate increases, leading to shear moduli that vanish as $1/n$ as $n \rightarrow \infty$.

(ii) $m_0 > 0$, and there are $d + m_0$ SSSs, that may or may not have an overlap with affine bond stretches. If more than d overlap, the additional SSSs stabilize elastic response relative that of the lattice with $m_0 = 0$, and we are presented with the curious situation in which additional zero modes increase elastic rigidity. The

usual cause of this effect is the appearance of sample traversing straight filaments that support macroscopic stress, but they also, as we have seen, introduce additional infinitesimal zero modes. The untwisted kagome lattice, with three $q = 0$ states of self stress produced by parallel filaments along three independent directions, is elastically stable with all eigenvalues of the elastic matrix positive. In spite of extra mechanisms it is possible for only some or even none of the SSSs to overlap with affine bond elongations, in which case the elastic energy can even fall to zero. The latter situation occurs in unrandomized periodic approximates to Penrose tilings [69] in which there are of order $\sqrt{n}$ zero modes and states of self-stress but in which all elastic moduli vanish [section 5.4].

4.2.2. Stiffness matrix of $2d$ periodic lattices with Guest modes Two-dimensional periodic lattices with one or two $q = 0$ SSSs and two $q = 0$ zero modes have two and one Guest modes, respectively. Fully gapped isostatic lattices have two such SSSs, but so do lattices that have additional zero modes at non-zero q. When there is only one Guest mode, the elastic matrix of (3.5), which acts on the strain vector $\boldsymbol{\varepsilon}_V$, has one zero eigenvalue with normalized eigenvector $\boldsymbol{v}_0 = (v_{0,1}, v_{0,2}, v_{03})$ (i.e., the strain of the Guest mode with amplitude U_G is $U_G \boldsymbol{v}_0$) and two positive eigenvalues, K_1 and K_2, with respective associated eigenvectors $\boldsymbol{v}_1$, and $\boldsymbol{v}_2$ so that

$$\mathbb{K}_{ij} = K_1 v_{1,i} v_{1,j} + K_2 v_{2,i} v_{2,j} \tag{4.13}$$

The long-wavelength stiffness matrix K is determined by $\mathbb{K}$, and as Appendix B shows, its determinant depends only on K_1, K_2, and the Guest-mode eigenvector $\boldsymbol{v}_0$:

$$\det \mathbf{K}(\boldsymbol{q}) = \frac{1}{4} K_1 K_2 \left(v_{02} q_x^2 - 2v_{03} q_x q_y + v_{01} q_y^2 \right)^2. \tag{4.14}$$

Since $\mathbf{K} = k \mathbf{Q} \cdot \mathbf{Q}^\dagger$, this implies that

$$\det \mathbf{C} = (\det \mathbf{Q})^* = (c/2)\sqrt{K_1 K_2/k} \, \left(v_{02} q_x^2 - 2v_{03} q_x q_y + v_{01} q_y^2 \right), \tag{4.15}$$

where c is some unit amplitude complex number. This simple form implies that in the $q \to 0$ limit the zeroes of $\det \boldsymbol{C}(\boldsymbol{q})$, which occur at [70]

$$q_y = \frac{q_x}{v_{01}} \left(v_{03} \pm \sqrt{v_{03}^2 - v_{01}v_{02}} \right), \tag{4.16}$$

depend only on $\boldsymbol{v}_0$ and not on the elastic moduli K_1 and K_2. The negative of the quantity under the square root is proportional to the determinant of the strain of the Guest mode:

$$\det \boldsymbol{\varepsilon}_G = \varepsilon_{xx}\varepsilon_{yy} - \varepsilon_{xy}^2 = U_G^2(v_{01}v_{02} - v_{03}^2). \tag{4.17}$$

Thus, to order q^2, there is a zero mode with real values of q_x and q_y if $\det \boldsymbol{\varepsilon}_G < 0$ and complex values when $\det \boldsymbol{\varepsilon}_G > 0$. The complex values of $\boldsymbol{q}$ correspond to decaying or growing surface modes. The zeros at real values of $\boldsymbol{q}$ can either become complex when higher-order terms in the q-expansion are included, in which case they again correspond to surface modes albeit with an inverse decay length quadratic rather than linear in the surface wavenumber, or they can remain real. In the latter case, they can occur at specific values of $\boldsymbol{q}$, in which case they are isolated. These points, which have a topologically protected winding number are called Weyl points, and

they have received considerable attention recently in relation to Dirac semimetals and topological insulators [53, 71, 72, 73, 74, 75, 76, 77, 78] and in photonic materials [79, 80, 81]. The distorted square lattices of figure 3(b) has isolated Weyl points [70]. It is also possible to have Weyl lines rather than isolated points. These occur in distorted versions of the $3d$ pyrochlore lattice [82] and gyroid photonic crystals [80].

5. Examples of periodic lattices

In this section, we will study three simple lattices: the square, kagome, and twisted kagome lattices depicted in figure 3. They provide specific examples of the phenomena discussed in the preceding section. Section 5.1 and 5.2 rely heavily of reference [45] and section 5.3 on reference [83].

5.1. Square Lattice

5.1.1. The nearest-neighbor lattice The periodic square lattice (figure 6) with only nearest neighbor bonds, along $\boldsymbol{b}_1 = a(1,0)$ and $\boldsymbol{b}_2 = a(0,1)$, and one site and two bonds per unit cell is the simplest example of a periodic Maxwell lattice. Many of its properties follow without calculation from the observations of the previous sections. It consists of straight filaments in orthogonal directions, each of which develops an SSS when placed under periodic boundary conditions. Thus an $N_x \times N_y$ lattice has $N_S = N_x + N_y$ states of self stress and

$$N_0 = N_x + N_y \qquad (5.1)$$

zero modes, which, apart from the trivial translation modes, are infinitesimal floppy modes in which any row or column is rigidly displaced as shown in figure 6(c). These rigid displacements form a basis for the null space of C, and their Fourier transforms do as well. If filaments parallel to the x-axis are rigidly displaced, then $q_x = 0$, and the Fourier transform of a set of displaced filaments parallel to the x-axis are indexed by a wavevector $\boldsymbol{q}_1 = (0, q_y)$. Similarly rigidly displaced filaments parallel to the y-axis are indexed by $\boldsymbol{q}_2 = (q_x, 0)$. There are N_x independent values of q_x and N_y of q_y. Each wavevector represents a zero mode, and since there are N_x independent values of q_x and N_y independent values of q_y, these account for all of the $N_x + N_y$ zero modes, linear combinations of which account for rigid translations and rotations. Thus, the bulk phonon spectrum for the periodic square Maxwell lattice has two lines of zero modes running from the center Γ of the Brillouin Zone to the midpoint M and M' at the zone boundaries as shown in figure 7.

An $N_x \times N_y$ lattice with free boundary conditions can be created by cutting and removing $N_x + N_y$ bonds from an $N_x \times N_y$ lattice under PBCs. Thus, the cut lattice has only $2N_xN_y - (N_x + N_y)$ bonds [figure 6]. In the cutting process, however, all $N_x + N_y$ SSSs are lost, and the zero mode count of the free lattice is the same as that of the periodic lattice. To infinitesimal order in the displacement, the modes themselves are identical in the two cases. In the free lattice, however, the modes are nonlinear as shown in figure 6(c). The bulk zero modes, which are seen under periodic boundary conditions, exhaust the Index theorem count. There are no additional zero modes at the surface of the free lattice. It is clear that any distortion of one of the surfaces parallel to the x- or y-axis of the free lattice will be transmitted across the entire sample by the rigid filaments, which support the SSS under periodic boundary
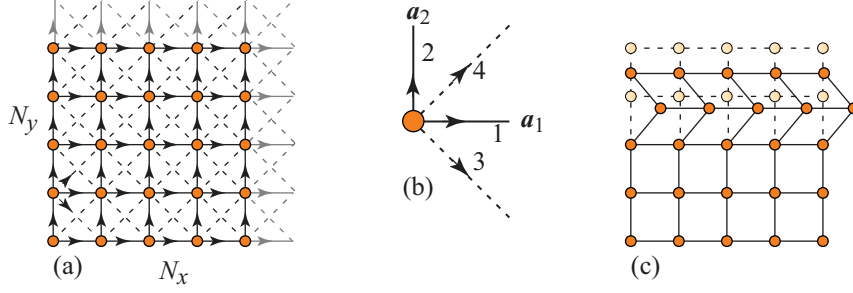
Figure 6. (a) An $N_x = 5$ by $N_y = 5$ square lattice with NN (full lines) and NNN (dashed lines) bonds showing bond directions for the calculation of self stress. The gray bonds at the right and upper boundaries are the $N_x + N_y = 10$ NN and $2(N_x + N_y - 1)$ NNN bonds that must be cut to from a $N_x \times N_y$ lattice under periodic boundary conditions to produce the $N_x \times N_y$ lattice under free boundary conditions. (b) A unit cell showing its two Bravais lattice vectors $\boldsymbol{a}_1$ and $\boldsymbol{a}_2$ and it two NN (1 and 2) and two NNN (3 and 4) bonds. (c) A finite mechanism of the finite square lattice with NN bonds only. This is also an infinitesimal mechanism in the periodic lattice.
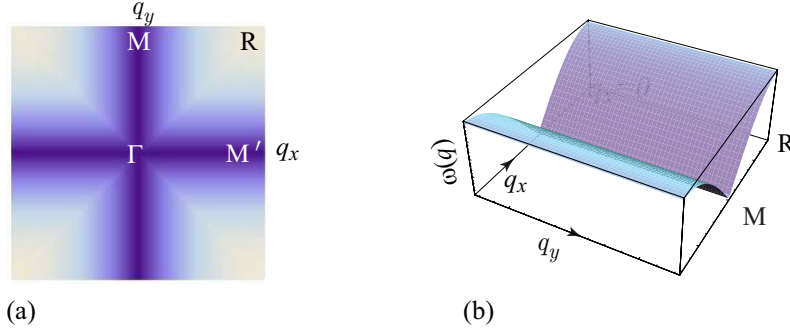

Figure 7. (a) Density plot of the lowest-frequency mode of the NN square lattice showing lines of zero modes running from the Brillouin zone center at Γ to the midpoints M and M' of the zone edge. (b) $3d$ plot of the single mode $\omega_x(\boldsymbol{q})$, which is independent of q_y and equal to zero for $q_x = 0$. *After reference [45]*

conditions. So, zero modes are not localized near the surface; surface distortions have infinite penetration depth and thus do not constitute surface modes.

There are exactly two SSSs at $\boldsymbol{q} = 0$, and they clearly overlap affine bond elongations, which are equal to $a\varepsilon_{xx}$ for bonds parallel to the x-axis and to $a\varepsilon_{yy}$ for bonds parallel to the y axis. Thus the elastic energy density is simply

$$f_{\text{el}} = \tfrac{1}{2}k\left(\varepsilon_{xx}^2 + \varepsilon_{yy}^2\right). \tag{5.2}$$

There are two independent lattice distortions, ε_{xx} and ε_{yy}, that cost energy and one ε_{xy} that does not in agreement with the analysis of section 4.2.1.

5.1.2. The next-nearest-neighbor lattice Introducing NNN bonds, $\boldsymbol{b}_3 = a(1, -1)$ and $\boldsymbol{b}_4 = a(1, 1)$, increases the bond number without changing the number of sites. If NNN bonds are added one at a time, initially no additional SSSs are created, and

each additional bond decreases the zero-mode count by one. As additional bonds are added, eventually additional states of self stress are created, for example in isolated cells with two NNN bonds in configurations like that of figure 4(d). Consider for simplicity the case with $N_x = N_y$. If a filament of equivalent contiguous NNN bonds (pointing either up or down) traverses the sample, a new SSS along that line is created. Thus, if there are no other NNN bonds, the change in bond number and number of SSSs relative to those in the state with no NNN bonds are, respectively, $\Delta N_B = N_x$ and $\Delta N_S = 1$, leading to a decrease in the number of zero modes of $\Delta N_0 = -N_x + 1$ for a total of $N_0 = N_x + 1$. If each unit cell has an upward pointing NNN bond and not a downward pointing one, $\Delta N_B = N_x^2$. In addition, there is one SSS for every $\boldsymbol{q}$ except $\boldsymbol{q} = 0$ for which there are three for a total of $N_S = N_x^2 + 2$ leading to $N_0 = 2$, i.e., leaving only the required two zero modes of uniform translation. Each added down pointing bond increases N_B and N_S by one leaving N_0 fixed at two. Thus, if all NNN bonds are present, there are no zero modes beyond the two at $\boldsymbol{q} = 0$, and the spectrum is gapped everywhere except at $\boldsymbol{q} = 0$ as shown in figure 8(a).

The gap at points M provides a characteristic frequency,

$$\omega^* = 2\sqrt{\frac{k'}{m}}, \tag{5.3}$$

and a comparison of the $k' = 0$ linear dispersion with the $k' \neq 0$ dispersion along the zone edge near M [figure 8(b)] yields a characteristic length

$$\ell^* = \frac{a}{2}\sqrt{\frac{k}{k'}}, \tag{5.4}$$

which diverges as $k' \to 0$. The approach of ω^* and $(\ell^*)^{-1}$ to zero as the Maxwell limit, $k' \to 0$, is similar to the behavior of these quantities near jamming where $\omega^* \sim (\Delta z)$ and $l^* \sim (\Delta z)^{-1}$ [37]. This result is not altogether surprising, given that weakening the spring constants of NNN bonds to zero yields the Maxwell limit in which there is no characteristic frequency or inverse length. An effective medium analysis [46] of the case in which NNN bonds are randomly added with probability $p = (z - z_c)/4$ leads to exactly the same results as jamming.

5.1.3. Equilibrium and dynamical matrices We now investigate how these results follow from explicit calculations of the equilibrium and compatibility matrices. We set $\boldsymbol{a}_1 = a(1, 0)$ and $\boldsymbol{a}_2 = a(0, 1)$ and designate the NN bonds 1 and 2 to be to the right and above each lattice site, respectively, and NNN bonds 3 and 4 to be along $\boldsymbol{a}_1 - \boldsymbol{a}_2$ and $\boldsymbol{a}_1 + \boldsymbol{a}_2$, respectively, as shown in figure 6(b). Following the rules outlined in section 2.2, the force at site ℓ is $\boldsymbol{f}(\boldsymbol{R}_\ell) = \boldsymbol{t}_1(\boldsymbol{R}_\ell) - \boldsymbol{t}_1(\boldsymbol{R}_\ell - \boldsymbol{a}_1) + \boldsymbol{t}_2(\boldsymbol{R}_\ell) - \boldsymbol{t}_2(\boldsymbol{R}_\ell - \boldsymbol{a}_2)$, and

$$\mathbf{Q}_{NN}(\boldsymbol{q}) = -\begin{pmatrix} 1 - e^{-iq_x a} & 0 \\ 0 & 1 - e^{-iq_y a} \end{pmatrix}. \tag{5.5}$$

Thus if $q_x = 0$ and $q_y \neq 0$, the one-dimensional null space of $\mathbf{Q}(\boldsymbol{q})$ is spanned by the unit vector $\hat{\boldsymbol{t}}_x(q_y) = (1, 0)$; and if $q_y = 0$ and $q_x \neq 0$, it is spanned by the vector $\hat{\boldsymbol{t}}_y(q_x) = (0, 1)$. In other words, for each $q_y \neq 0$, there is a SSS for each value of q_y with independent tensions in bonds parallel to the x-axis that have the same value for every bond in a given filament and similarly for $q_x \neq 0$. When both q_x and $q_y = 0$, there are two SSSs . Thus, there is one state SSS for each value of q_x and one for each
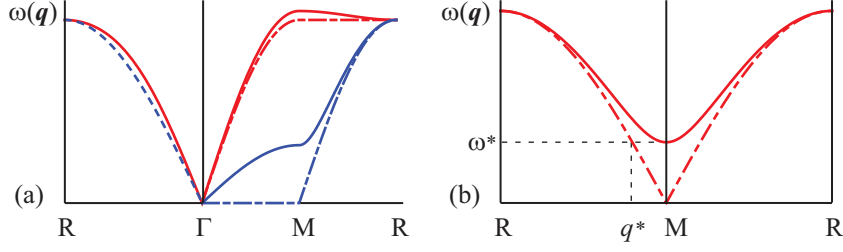
Figure 8. (a) Comparison of the square-lattice phonon frequencies along symmetry directions in the BZ with $k' = 0$ (dashed lines) and $k' > 0$ (full lines) The blue curves depict $\omega_1(k', q)$, the lower and the red curves, $\omega_2(k', q)$, the higher of the two modes. The single blue dashed line from R to Γ represents the curves $\omega_1(0, q)$, $\omega_1(k1, q)$, and $\omega_2(0, q)$, all of which are the same. (b) Frequencies for $k' = 0$ and $k' > 0$ along the BZ edge from R to M and back to R. When $k' = 0$, the frequency grows linearly with q away from M. When $k' > 0$, there is a gap defining the characteristic frequency $\omega^* = \sqrt{k'}$ and a length scale when $l^* \sim 1/\omega^*$.

value of q_y for a total of $N_S = N_x + N_y$ SSSs . The null pace of $\boldsymbol{C}(\boldsymbol{q}) = \mathbf{Q}_{NN}^\dagger(\boldsymbol{q})$, which consists of the set of zero modes, is similar with one zero mode per q_x and q_y for a total of $N_0 = N_S$ zero modes as required by Index theorem. It consists of rigid displacements of individual rods as already discussed.

The force at site ℓ arising from NNN bonds is $\boldsymbol{f}^{NNN}(\boldsymbol{R}_\ell) = \boldsymbol{t}_3(\boldsymbol{R}_\ell) - \boldsymbol{t}_3(\boldsymbol{R}_\ell - \boldsymbol{b}_3) + \boldsymbol{t}_4(\boldsymbol{R}_\ell) - \boldsymbol{t}_4(\boldsymbol{R}_\ell - \boldsymbol{b}_4)$, and the NNN equilibrium matrix is

$$\mathbf{Q}_{NNN}(\boldsymbol{q}) = -\frac{1}{\sqrt{2}} \begin{pmatrix} 1 - e^{-i(q_x - q_y)a} & 1 - e^{-i(q_x + q_y)a} \\ -1 + e^{-i(q_x - q_y)a} & 1 - e^{-i(q_x + q_y)a} \end{pmatrix}. \tag{5.6}$$

When both NN and NNN bonds are present, there are four bonds per unit cell, and the full equilibrium matrix is a the 2×4 matrix

$$\mathbf{Q}(\boldsymbol{q}) = \begin{pmatrix} \mathbf{Q}_{NN}(\boldsymbol{q}) & \mathbf{Q}_{NNN}(\boldsymbol{q}) \end{pmatrix}. \tag{5.7}$$

At $\boldsymbol{q} = 0$, all entries in $\mathbf{Q}$ are zero, and all $\boldsymbol{q} = 0$ bond vectors are in its null space. Thus, the elastic energy is simply the expected affine result,

$$f = \tfrac{1}{2V} \sum_{\alpha=1}^{4} k_\alpha (\hat{\boldsymbol{b}}_{\alpha,i} \varepsilon_{ij} \boldsymbol{b}_{\alpha,j})^2 \tag{5.8a}$$

$$= \tfrac{1}{2} k(\varepsilon_{xx}^2 + \varepsilon_{yy}^2) + \tfrac{1}{4} k' [(\varepsilon_{xx} + \varepsilon_{yy} + 2\varepsilon_{xy})^2 + (\varepsilon_{xx} + \varepsilon_{yy} - 2\varepsilon_{xy})^2] \tag{5.8b}$$

$$= \tfrac{1}{2} K_{11}(\varepsilon_{xx}^2 + \varepsilon_{yy}^2) + K_{12}\varepsilon_{xx}\varepsilon_{yy} + 2K_{44}\varepsilon_{xy}^2, \tag{5.8c}$$

where $K_{11} = k + k'$, and $K_{12} = K_{44} = k'$. As expected, shear moduli vanish when $k' = 0$.

The NN and NNN dynamical matrices are

$$\mathbf{D}^{NN}(\boldsymbol{q}) = 4\frac{k}{m} \begin{pmatrix} \sin^2(q_x a/2) & 0 \\ 0 & \sin^2(q_y a/2) \end{pmatrix}, \tag{5.9a}$$

$$\mathbf{D}^{NNN}(\boldsymbol{q}) = 2\frac{k'}{m} \begin{pmatrix} 1 - \cos q_x a \cos q_y a & \sin q_x a \sin q_y a \\ \sin q_x a \sin q_y a & 1 - \cos q_x a \cos q_y a \end{pmatrix}. \tag{5.9b}$$
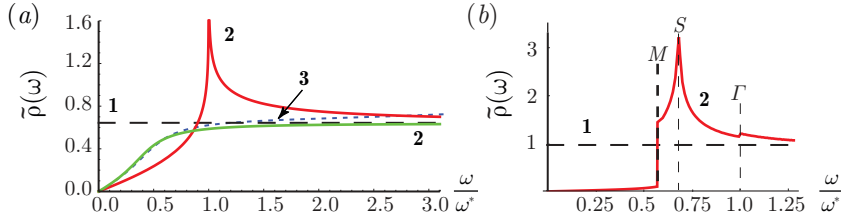
Figure 9. Densities of states $\tilde{\rho}(\omega) = \rho(\omega)/\rho(0)$ for the (a) square and (b) kagome lattices. The dashed black line (labeled **1**) is the flat, one-dimensional $\tilde{\rho}(\omega)$ at $\omega \ll \omega_0$ when $k' = 0$, and the full red line (labeled **2**) is $\tilde{\rho}(\omega)$ for $k' > 0$ showing linear-in-ω Debye behaviour at $\omega \ll \omega^*$, van Hove singularities near $\omega = \omega^*$ and constant behaviour at $\omega > \omega^*$. Lines **3** and **4** in (a) are effective medium results for different probabilities of occupation of NNN bonds showing the washing-out of the van Hove singularity and the smooth transition from Debye to one-dimensional behavior. *Adapted from references [45] and [46]*

The spectrum arising from the sum of these dynamical matrices is shown in figure 8. When $k' = 0$, only $\mathbf{D}^{NN}$ contributes, and there are two independent one-dimensional modes with

$$\omega_{x,y} = 2\omega_0 |\sin(q_{x,y}a/2)|, \tag{5.10}$$

where $\omega_0 = \sqrt{k/m}$. For every q_y, $\omega_x(\boldsymbol{q})$ goes to zero with q_x as cq_x, where $c = \omega_0 a$ is the longitudinal (compressive) sound velocity, and reaches a maximum of $2\omega_0$ at the point M on the zone edge $[\boldsymbol{q} = (\pi/a, 0)]$ and similarly for $\omega_y(\boldsymbol{q})$ as shown in figure 8. These one-dimensional spectra produce [65] (pages 205-209) a density of states

$$\rho(\omega) = \frac{1}{2\pi\omega_0 a} \left(1 - \frac{\omega^2}{4\omega_0^2}\right)^{-1/2}, \tag{5.11}$$

which approaches a constant as $\omega \to 0$ and diverges as $\omega \to 2\omega_0$ at the zone edge.

When $k' > 0$, modes [with $\boldsymbol{q} = q(\cos\theta, \sin\theta)$] exhibit a $\cos(4\theta)$ angular modulation at low frequency and one-dimensional $k' = 0$ behavior at larger $\boldsymbol{q}$. When $0 < k' \ll k$, $D_{ij}(\boldsymbol{q})$ is well approximated as a diagonal matrix with $D_{xx}(\boldsymbol{q}) = kq_x^2 + 4k'\sin^2(q_y/2)$ ($m = 1$) with associated eigenfrequency $\omega_x(\boldsymbol{q}) \sim \sqrt{D_{xx}(\boldsymbol{q})}$. These expressions immediately define the characteristic frequency of (5.3) at the point $M = (0, \pi)$ on the BZ edge. The first term in $D_{xx}(\boldsymbol{q})$ represents the long-wavelength one-dimensional NN-modes that are present when $k' = 0$, whereas the second represents the effects of NNN coupling. When $q_x = 0$, the only length scale in the problem is the unit lattice spacing, and no divergent length scale can be extracted from $D_{xx}(0, q_y)$. When the first term is large compared to the second, $D_{xx}(\boldsymbol{q})$ reduces to its form for the Maxwell $k' = 0$ limit, and we can extract a length by comparing these two terms. The shortest length we can extract is that of (5.4), which comes from comparing kq_x^2 to $D_{xx}(\boldsymbol{q})$ at point M on the zone edge as depicted in figure 8 If $q_y < \pi$, the Maxwell limit is reached when $q_x > q^*$. A similar analysis applies to $D_{yy}(\boldsymbol{q})$ when $q_y > q^*$. If a square of length l is cut from the bulk, the wavenumbers of its excitations will be greater than π/l, and for $ql^* > 1$, all modes within the box will

be effectively those of the lattice without NNN bonds. This construction is equivalent to the cutting argument of Wyart et al. [18, 38].

The characteristic length of (5.4) is identical to the length at which the frequency of the compressional mode $\omega_x(q_x \sim 1/l) = \sqrt{k}/l^* \sim \sqrt{K_{11}}/l^*$ becomes equal to ω^*. A meaningful length from the transverse mode $\omega_x(0, q_y)$ cannot be extracted in a similar fashion. The full phonon spectrum [figure 8(a)] exhibits acoustic phonons identical to those of a standard square lattice at $q \ll 1$ and a saddle point at the point M. Thus, the low-frequency density of states shown in figure 9(a) is Debye-like: $\rho(\omega) \sim \omega/\sqrt{kk'}$ with a denominator that, because of the anisotropy of the square lattice, is proportional to the geometric mean of longitudinal and transverse sound velocities rather than to a single velocity. In addition $\rho(\omega)$ exhibits a logarithmic van Hove singularity at ω^* and approaches the one-dimensional limit $(1/\pi)/\sqrt{k}$ at $\omega^* \ll \omega \ll 2\sqrt{k}$. The frequency ω^* [(5.3)] is recovered by equating the low-frequency Debye form at ω^* to the high-frequency isostatic form of the density of states.

5.2. Kagome lattice

The NN kagome lattice consists of three grids of straight parallel filaments intersecting at lattice sites as shown in figure 10. This figure also shows two different unit cells reflecting the 3-fold symmetry of the lattice. For the moment, we focus on lattices with $N_x = N_y$ cells on a side as shown in the figure. Appendix C derives the compatibility matrix for a generalized kagome lattice, of which the simple kagome lattice considered here is a special case. The equilibrium and dynamical matrices are straightforwardly calculated from it, as are the phonon spectrum and zero modes. As in the square lattice, each of the kagome-lattice filaments supports a SSS under periodic boundary conditions (care must be taken to join equivalent sites at the boundaries to create a single filament for bonds slanting to the left from the bottom), and the expectation is that a periodic lattice will have $3N_x$ states of self stress, and this is indeed the case. There is one state of self stress for each wavevector $\boldsymbol{q} = q\boldsymbol{G}_j/G_0$ along the symmetry equivalent lines from Γ to M in the BZ [figure 11(a)] parallel to the three reciprocal lattice vectors $\boldsymbol{G}_j$, where $G_0 = |\boldsymbol{G}_j| = 4\pi/(\sqrt{3}a)$. Since there are N_x values of $\boldsymbol{q}$ along each of these directions, there are a total of $3N_x$ SSSs, from which SSSs for individual filaments can be constructed.

The $3N_x$ SSSs require an equal number of zero modes, which, as in the square lattice, occur along lines in reciprocal space that have no component parallel to one of the three grids, i.e., along the lines ΓM in reciprocal space as shown in figure 11(b). The zero modes for a filament parallel to the x-axis consist of displacements of all 1-sites and 3 sites by $s(\cos \pi/6, \sin \pi/6)$ and $s(\cos \pi/6, -\sin \pi/6)$, respectively, for infinitesimal s. This corresponds to rigid rotations of triangles about site 2 as shown in figure 10(b). An alternative description of the mode is that the entire filament is displaced a distance $s \cos \pi/6$ to the right, and sites 1 and 3 are, respectively, displaced upward and downward a distance $s \sin \pi/6$ producing the zero-modes structure of figure 5(b). The spectrum of the lowest-frequency modes has a linear dispersion with $\omega = cq$ ($c = \sqrt{3}ka/8$) in the direction perpendicular to the $\Gamma - M$ zero modes (figure 12(c)).

As in the square lattice, adding NNN bonds gaps the spectrum leading to a characteristic frequency $\omega^* \sim \sqrt{k'}$ and associated length scale $\ell^* \sim 1/\sqrt{k'}$ calculated from the dispersion along the line M to K at the zone edge (figure 12). Other characteristic frequencies can be calculated from the lowest frequency optical modes
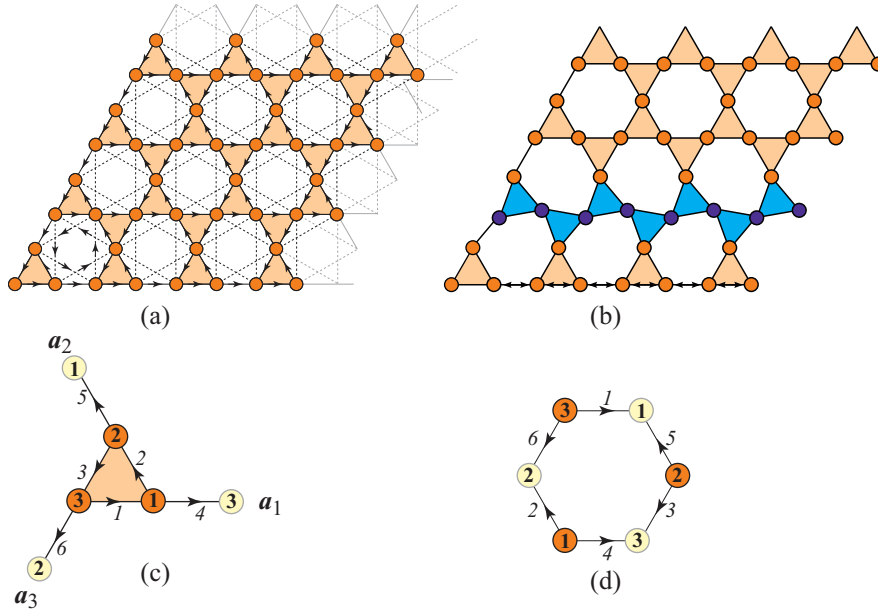
(a)   (b)

(c)   (d)

Figure 10. (a) An $N_x = 5$ by $N_y = 5$ kagome lattice showing NN (full lines) and NNN (dotted lines) bonds. The gray bonds along the right and upper edges are the $2(N_x + N_y - 1)$ NN and $4(N_x + N_y - 1)$ NNN bonds that must be cut from a $N_x \times N_y$ lattice under periodic boundary conditions to produce the the free $N_x \times N_y$ lattice. (b) Representation of a zero modes. (c) and (d) two different symmetric versions of the kagome unit cells showing labeling of sites and NN bonds. The vectors $\boldsymbol{a}_1$ and $\boldsymbol{a}_2$, $\boldsymbol{a}_1$ and $-\boldsymbol{a}_3$, or any other similar pair can serve as basis vectors for the triangular Bravais lattice.

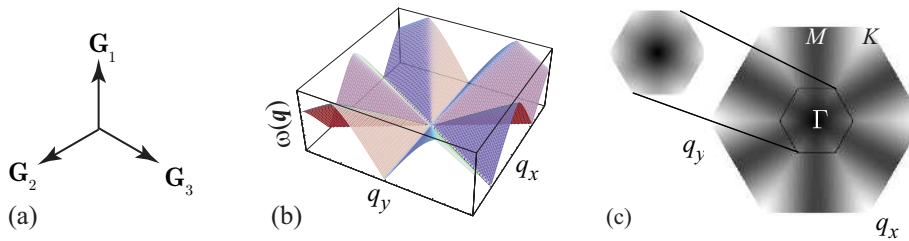(a)   (b)   (c)

Figure 11. (a) Shortest reciprocal lattice vectors, related by 3-fold rotations, of the kagome lattice that satisfy $\boldsymbol{G}_j \cdot \boldsymbol{a}_j = 0$. (b) Dispersion of lowest-frequency mode, showing "knife-edges" along the $\Gamma - M$ in the BZ. (c) Density plot of lowest-frequency mode with $k'/k = 0.02$. Note the isotropic behavior near $\boldsymbol{q} = 0$. *Adapted from reference [45]*
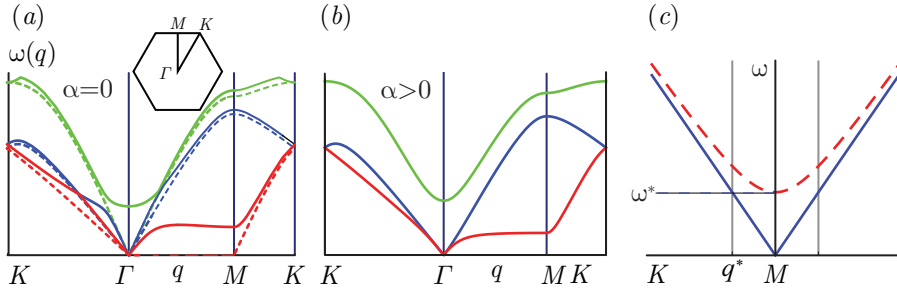
Figure 12. (a) Phonon spectrum for the three lowest modes of the undistorted kagome lattice. Dashed lines depict frequencies at $k' = 0$ and full lines at $k' > 0$. The inset shows the Brillouin zone with symmetry points Γ, M, and K. (b) Phonon spectrum of the twisted kagome lattice with $\alpha > 0$ and $k' = 0$. (c) Phonon dispersion along the zone edges from K to M in schematic form for both the undistorted lattice at $k' > 0$ and for the twisted lattice with $\alpha \neq 0$, showing the characteristic frequency $\omega^* = 2\sqrt{k'/m}$ ($\omega_\alpha \sim \sqrt{k/m}|\sin\alpha|$) and length $l^* = (q^*)^{-1} = (a/2)(k'/k)^{1/2}$ ($l_\alpha \sim 1/|\sin\alpha|$) for the untwisted (twisted) kagome lattice. *Adapted from references [45] and [83].*

or from the frequency at which the low-frequency acoustic phonon modes crosses over to a nearly flat dispersion.

A total of $4N_x - 1$ bonds must be cut to liberate a $N_x \times N_x$-unit-cell free lattice from its periodic parent. There are no states of self-stress in the free lattice, so there must be as many zero modes as bonds that are cut. This is more zero modes than the $3N_x$ in the periodic system. The difference between the two numbers arises from the joining of lines slanting to the left under periodic conditions. The number of horizontal and right slanting filaments is the same in both cases. However, under PBCs, there are N_x distinct left-slanting filaments; under free BCs, there are N_x such lines terminating at the bottom and $N_x - 1$ terminating at the right side of the lattice.

Because of the three sets of filaments aligned along $\boldsymbol{a}_n$, at $\boldsymbol{q} = 0$, there are now three rather than two SSSs, characterized by bond vectors $\hat{\mathbf{t}}_1 = (1, 0, 0, 1, 0, 0)/\sqrt{2}$, $\hat{\mathbf{t}}_2 = (0, 1, 0, 0, 1, 0)/\sqrt{2}$, and $\hat{\mathbf{t}}_1 = (0, 0, 1, 0, 0, 1)/\sqrt{2}$, each of which has a nonzero overlap with the vector of affine distortions. This gives enough SSSs to fully stabilize the elastic energy of the NN kagome lattice with nonzero Lamé coefficients [84]. Addition of NNN bonds increases these coefficients.

$$\lambda = \mu = \frac{\sqrt{3}}{8}(k + 3k') \tag{5.12}$$

The response is affine even though three sites per unit cell introduces the possibility of their undergoing nonaffine displacement to lower energy. However, the geometry of this lattice is special, and response is necessarily affine [28].

5.3. Twisted kagome lattice

The twisted kagome lattice is constructed from the finite zero modes by oppositely rotating triangles along all of the filaments of the untwisted lattice through an angle α as shown in figure 13. There are a continuum of lattices indexed by the angle α that bond 1 makes with the x-axis. As we shall see, this lattice has properties that at first blush seem surprising but that in fact are simple consequences of the Index theorem .
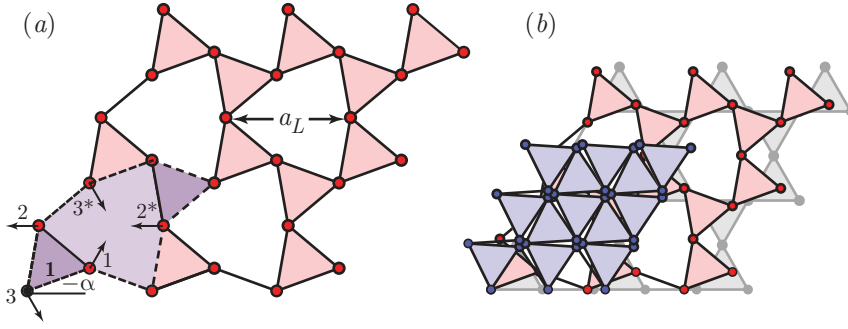
Figure 13. (a) Twisted kagome lattice showing the displacements of sites in the two unit cells shown in figure 10 and rotation of triangles through $\pm\alpha$. Bond **1** (connecting sites 3 and 1) in this figure is rotated through an angle $-\alpha$. The lattice spacing for bonds of length $a/2$ is $a_L = a\cos\alpha$. (b) Lattices with different values of α superposed showing how changing α reduces the lattice area. *From reference [83]*

5.3.1. Bulk and elastic properties The straight filaments of the untwisted kagome lattice become "zigzagged" and lose their ability to sustain SSSs . The result is that there are only the two $q = 0$ states of self stress required by the Index theorem and the existence of two zero modes of translation, and there are no zero modes other than those at $q = 0$. Thus the simple rotation of triangles to create the twisted lattice from the the untwisted ones gaps all but the $q = 0$ bulk phonons, just as does adding NNN bonds to the untwisted lattice (figure 12). The untwisted spectrum is approached continuously as $\alpha \to 0$ leading to a characteristic frequency (measured by the gap at the symmetry point M) and associated length scale,

$$\omega_\alpha \sim |\sin\alpha|, \qquad l_\alpha \sim \frac{1}{|\sin\alpha|}. \tag{5.13}$$

that, respectively, vanish and diverge as $\alpha \to 0$.

As figure 13 shows, twisting the lattice uniformly compresses it. If bond lengths are fixed at $a/2$, the Bravais lattice vectors are reduced in length from a to $a_L = a\cos\alpha$, and the volume of each unit cell from $(\sqrt{3}/2)a^2$ to $(\sqrt{3}/2)a^2\cos^2\alpha$. Thus angle changes modify the area of the lattice without changing any bond length of a NN lattice, implying that the bulk modulus B of these lattices vanishes for all $\alpha \neq 0$. Observe that the twisted lattice has the peculiar property that it expands or contracts isotropically at no energy cost. If it expands in one direction, it will also do so in the opposite direction. Elastic materials with this property have a negative Poisson ratio [59]; they are *auxetic*. The twisted kagome lattice has the most negative allowed Poisson ratio of -1, which it retains for all strain, and it sometimes called *maximally auxetic* [83]. In addition, the unit cell contracts isotropically. Such lattices are termed *equiauxetic* [85]. There are not many naturally occurring materials that have this property, but artificial ones can be created [86].

As indicated above, there are two $q = 0$ states of self-stress that have the potential to create non-vanishing elastic moduli. The long-wavelength elasticity is necessarily isotropic, so if the bulk modulus is zero, the only option if for there to be an isotropic shear modulus or for none of the elastic moduli to be nonzero. The two states of self-stress overlap with affine strain, the shear modulus $\mu = \sqrt{3}k/8$ is nonzero (and

curiously independent of α and identical to that of the untwisted kagome lattice [(5.12)], and the elastic energy density is

$$f_{\text{el}} = \frac{1}{2}\mu\,\tilde{\varepsilon}_{ij}\tilde{\varepsilon}_{ij} \tag{5.14}$$

where $\tilde{\varepsilon}_{ij} = \varepsilon_{ij} - \frac{1}{2}\varepsilon_{kk}$ is the symmetric, traceless shear-strain tensor.

The strain is related to the metric tensor g_{ij} via $\varepsilon_{ij} = (g_{ij} - \delta_{ij})/2$. The traceless part of the strain, $\tilde{\varepsilon}_{ij} = (1/2)(g_{ij} - \frac{1}{2}\delta_{ij}g_{kk})$, which is zero for $g_{ij} = \delta_{ij}$, is invariant, and thus remains equal to zero, under conformal transformations that take the metric tensor from its reference form δ_{ij} to $h(\mathbf{x})\delta_{ij}$ for any continuous function $h(\mathbf{x})$ of position $\mathbf{x}$. The zero modes of the theory thus correspond simply to conformal transformations, which in two dimensions are best represented by the complex position and displacement variables $z = x+iy$ and $w(z) = u_x(z)+iu_y(z)$. All conformal transformations are described by an analytic displacement field $w(z)$. Since by Cauchy's theorem, analytic functions in the interior of a domain are determined entirely by their values on the domain's boundary (the "holographic" property [87]), the zero modes of a given sample are simply those analytic functions that satisfy its boundary conditions. For example, a disc with fixed edges ($\boldsymbol{u} = 0$) has no zero modes because the only analytic function satisfying this FBC is the trivial one $w(z) = 0$; but a disc with free edges (stress and thus strain equal to zero) has one zero mode for each of the analytic functions $w(z) = a_n z^n$ for integers $n \geq 0$. The boundary conditions $\lim_{x\to\infty}\boldsymbol{u}(x,y) = 0$ and $\boldsymbol{u}(x,y) = \boldsymbol{u}(x+L,y)$ on a semi-infinite cylinder with axis along x are satisfied by the function $w(z) = \mathrm{e}^{iq_x z} = \mathrm{e}^{iq_x x}e^{-q_x y}$ when $q_x = 2n\pi/L$, where n is an integer. This solution is identical to that for classical Rayleigh waves [59] on the same cylinder. Like the Rayleigh theory, the conformal theory puts no restriction on the value of n (or equivalently q_x). Both theories break down, however, at $q_x = q_c \approx \min(l_\alpha^{-1}, a^{-1})$ beyond which the full lattice theory, which yields a complex value of $q_y = q_y' + iq_y''$, is needed.

5.3.2. Surface modes As we have seen, free two-dimensional lattices of N sites cut from a periodic Maxwell lattice necessarily have of order $\sqrt{N}$ zero modes because of order $\sqrt{N}$ bonds must be cut, and any sample-spanning states of self stress are lost under the cut. In the untwisted kagome lattice, these modes are identical to the bulk zero modes calculated under PBCs. In the twisted lattice, whose cut lattice must have the same number of zero modes as the untwisted lattice, there are no bulk zero modes (except at $\boldsymbol{q} = 0$), and as a result the zero modes must be localized at surfaces. In the long-wavelength limit, these modes must reduce to the zero-frequency Rayleigh waves of an isotropic elastic continuum with vanishing bulk modulus with decay length $l_s \equiv \kappa^{-1}$ equal to the inverse surface wavenumber q. At shorter wavelength, l_s is determined by the length l_α associated with the twisted phonon gap.

Figure 14 depicts a finite rectangular sample with free horizontal surfaces parallel to $\boldsymbol{a}_1$ and vertical surfaces parallel to $\boldsymbol{a}_2 - \boldsymbol{a}_3$ along with unit cells constructed so that all sites and bonds on a surface lie in periodically repeated continuous cells. It also shows which bonds (or bonds and sites) must be removed to liberate the finite lattice from the one under PBCs. The removal of two bonds or four bonds and one site per unit cell liberate the horizontal surfaces. In either case, the number of zero modes per cell is $n_0 = 2\Delta n - \Delta n_b = 2$, where $\Delta n = 0$, $\Delta n_b = -2$ in the first case and $\Delta n = -1$, $\Delta n_b = -4$ in the second. Similar arguments yield $n_0 = 4$ for vertical surfaces. As might be expected, the modes are distributed equally between opposite
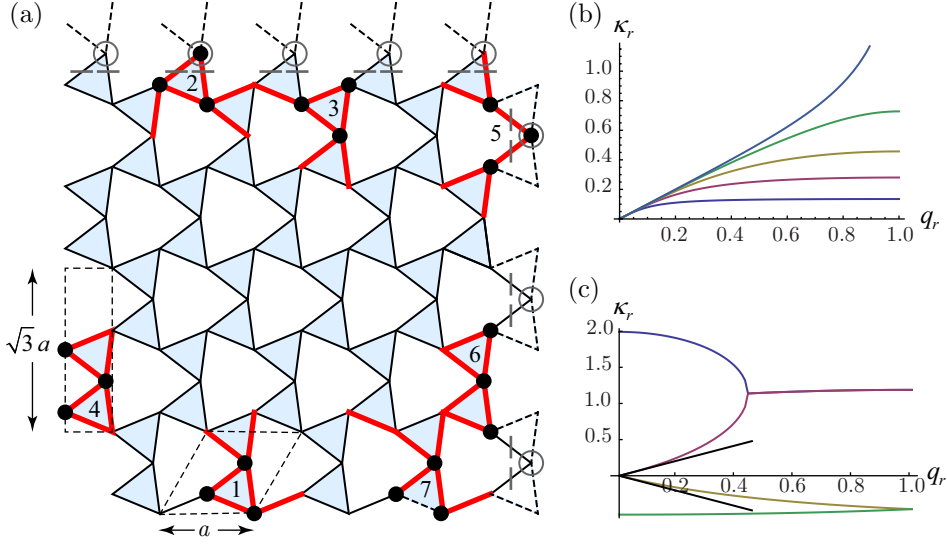
Figure 14. (color online) (a) A free twisted kagome lattice with free horizontal and vertical boundaries. Sites and bonds of unit cells that match the surface are shown in black and red, respectively, and the geometric form of these unit cells are indicated by dashed quadrilaterals. Cutting the two (four) dashed bonds per cell on the horizontal (vertical) boundary produces a lattice with bottom (left) and top (right) boundary cells 1 (4) and 2 (5). Alternatively removing these bonds along with one circled site and the two bonds crossed by grey lines changes the top (right) boundary cell from 2 (5) to 3 (6). The number of zero modes per site is 1 (2) per site on both the bottom (right) and top (left) boundaries. Cell 7 has one additional bond cut from it. (b) The reduced inverse decay length $\kappa_r = \kappa/(G_r/2)$ of the horizontal boundaries as a function of $q_r = q/(G_r/2)$, where $G_r = 2\pi/a$ for $\alpha = \pi/20, \pi/10, 3\pi/20, \pi/5, \pi/4$ in order from bottom to top. All curves follow $\kappa_r = q_r$ near $q_r = 0$. The curve at $\alpha = \pi/4$ diverges at $q_r = 1.0$. (c) κ_r as a function of q_r with $G_r = 2\pi/\sqrt{3}$ for $\alpha = \pi/8$. The positive curves are for the left boundary and the negative ones are minus κ_r for the right boundary. The two positive curves merge at $q_r \approx 0.4$. There are still two distinct decays beyond this point with the same real part and different imaginary parts. The straight grey lines are the elastic limit $\kappa_r = q_r$.

surfaces, i.e., there is one zero mode per unit cell on horizontal surfaces and two modes per unit cell on vertical surfaces. Equivalently, there is one (two) mode per surface wavenumber $-\pi/G_s < q < \pi/G_s$, where G_s is the magnitude of the surface reciprocal lattice vector, $2\pi/a$ for horizontal and $2\pi/(\sqrt{3}a)$ for vertical surfaces.

The amplitude of the surface modes decay as $\exp[-\tilde{\kappa}s]$ with distance s away from the surface all of the way to the opposite free surface, where $\tilde{\kappa}$ is in general complex indicating oscillations along with decay. $\kappa \equiv \operatorname{Re}\tilde{\kappa} = l_s^{-1}$ is the inverse decay length. In the case of horizontal surfaces, the decay length is the same on opposite surfaces. Figure 14(b) plots the single $\kappa(q, \alpha)$ for different values of α. In the case of vertical surfaces, the two decay lengths for the left surface differ from those of the right one. Figure 14(c) plots these for $\alpha = \pi/8$. In all cases, one $\kappa(q, \alpha)$ reduces to $\kappa(q, \alpha) = q$ in the long-wavelength limit as required by the continuum theory.

Surface zero modes are by definition in the null space of the compatibility matrix C. Systems with parallel free surfaces with PBCs along their direction of alignment can be viewed as a series of layers $n = 1, ..., N$, and C can be decomposed as

$$\mathsf{C} = \begin{pmatrix} \mathbf{C}_{11} & \mathbf{C}_{12} & 0 & \ldots & 0 & 0 \\ 0 & \mathbf{C}_{11} & \mathbf{C}_{12} & \ldots & 0 & 0 \\ \ldots\ldots\ldots\ldots\ldots\ldots\ldots\ldots\ldots\ldots\ldots\ldots\ldots \\ 0 & 0 & 0 & \ldots & \mathbf{C}_{11} & \mathbf{C}_{N-1,N} \\ 0 & 0 & 0 & \ldots & 0 & \mathbf{C}_{NN} \end{pmatrix}, \tag{5.15}$$

where all $\mathbf{C}_{ij}$'s depend on the surface wavenumber q and α. $\mathbf{C}_{11}$ is the 6×6 matrix connecting bonds and sites within in a single unit cell and $\mathbf{C}_{12}$ is the 6×6 matrix connecting bonds in one unit cell to sites in unit cells one layer deeper in the sample. The same unit cells are used throughout the sample. The opposite surface may terminate with only a partial version of these cells, and the exact forms of $\mathbf{C}_{N-1,N}$ and $\mathbf{C}_{NN}$ depend on how the surface is terminated. Consider, for example, horizontal surfaces, the bottom of which is characterized by the unit cell labeled 1 in figure 14(a) and the top of which is characterized by unit cell 2. For modes localized at the bottom surface, unit cell 1 is used through out the sample. The termination cell 2 at the opposite surface has all three sites but only four bonds of unit cell 1. The missing bonds (5 and 6) are not affected by cell $N - 1$. Therefore, $\mathbf{C}_{N,N-1} = \mathbf{C}_{12}$ is a 6×6 matrix, and $\mathbf{C}_{NN}$ is a 4×6 matrix. If the top surface is terminated by unit cell 3, which has only 2 sites and 2 bonds of cell 1, $\mathbf{C}_{N-1,N}$ is a 6×4 matrix and $\mathbf{C}_{N,N}$ is a 2×4 matrix. Thus displacements $\mathsf{U} = (\boldsymbol{u}_1, ..., \boldsymbol{u}_N)$ in the null space of C satisfy

$$\mathbf{C}_{11}\boldsymbol{u}_n + \mathbf{C}_{12}\boldsymbol{u}_{n+1} = 0, \tag{5.16}$$

for $n = 1, ...N - 2$. These equations are solved by $\boldsymbol{u}_{n+1} = \lambda \boldsymbol{u}_n$ and

$$\det(\mathbf{C}_{11} + \lambda \mathbf{C}_{12}) = 0 \tag{5.17}$$

subject to the boundary conditions that $\mathbf{C}_{11}\boldsymbol{u}_{N-1} + \mathbf{C}_{N-1,N}\boldsymbol{u}_N = 0$ and $\mathbf{C}_{NN}\boldsymbol{u}_N = 0$.

The inverse penetration depth is determined by λ via $\exp[-\kappa a_\perp] = \lambda$, where $a_\perp = a\sqrt{3}/2$ is the distance between unit cells in the direction perpendicular to the surface. In case of termination with either unit cell 2 or unit cell 3, $\boldsymbol{u}_N$ must equal $\lambda \boldsymbol{u}_{N-1}$ to solve the first boundary condition. Though required by the known existence of the zero mode, it is a remarkable fact that the projection of $\boldsymbol{u}_1$, which is in the null space of $\mathbf{C}_{11} + \lambda \mathbf{C}_{12}$, onto the space of displacements of the last layer is also in the null space of $\mathbf{C}_{NN}$, and as advertised earlier, the surface mode decays exponentially from one free surface to the next. A similar analysis applies to the vertical surface for which $a_\perp = a/2$. Of course, any linear combination of the exponentially decaying modes on the two sides of a strip is a zero mode if both are individually. In the usual situation in which the Rayleigh waves have a nonzero frequency, the eigenstates of a finite strip are symmetric and anti-symmetric combinations of states on the two surfaces that interact across the strip yielding a peristaltic mode with $\omega \sim q$ and a bending mode with $\omega \sim q^2$. It should be noted that κ for modes that are not localized within the surface unit cell can also be calculated from $\det C(\boldsymbol{q})$, which is a function of $\exp[i\boldsymbol{q} \cdot \boldsymbol{a}_i]$, $i = 1, ..., 3$, by setting $\boldsymbol{q} = q_\perp \hat{\boldsymbol{n}}_{in} + \boldsymbol{q}_{||}$ where $\boldsymbol{q}_{||}$ is the component of $\boldsymbol{q}$ parallel to the surface and $\hat{\boldsymbol{n}}_{in}$ is the unit inward normal to the surface, setting $q_\perp = i\kappa$, and solving for κ in $\det C(i\kappa, \boldsymbol{q}_{||}) = 0$. This approach does not directly provide eigenvectors satisfying boundary conditions.
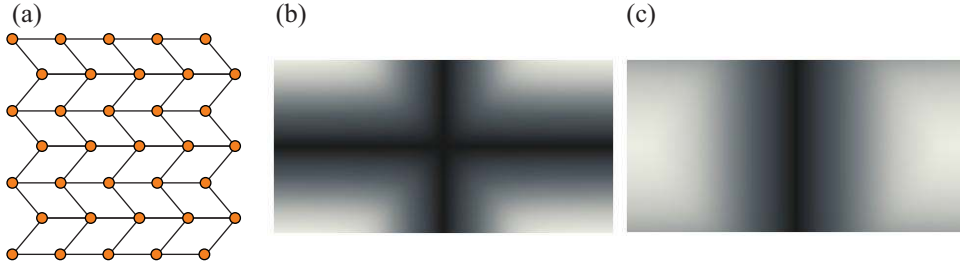
Figure 15. (a) The zigzagged square lattice with two sites per unit cell and rectangular unit cells and Brillouin zone. (b) and (c) density plots of the two lowest-frequency bands, showing lines of zero modes along $q_y = 0$ and $q_x = 0$ in (a) and along $q_x = 0$ in (b). The total number of zero modes in the two bands is the same as in the undistorted square lattice.

A surface consisting of unit cells 7 in figure 14(a) differs from surfaces composed of other unit cells shown in that figure in that it is missing a bond on the surface: it is obtained from cell 1 by cutting the dashed downward pointing bond, and as a result, this surface has two, not one zero mode per cell. The calculation just outlined indeed produces two zero modes per q, one of which is localized completely on the first row because $\mathbf{C}_{11}$ has a non-empty null space. Similarly, κ diverges as shown in figure 14(b) at $q = \pi/G_s$ for $\alpha = \pi/4$ because $\mathbf{C}_{11}(\pi/G_s, \pi/4)$ has a non-empty null space.

5.4. Other lattices

So far, we have focussed on the three simplest examples of two-dimensional periodic Maxwell lattices and the free lattices cut from them. There are many others that can be constructed from these without changing the local coordination numbers or the lengths of any bonds and whose properties can easily be understood in the context of the Index theorem. One of the simplest of such lattices is the "zigzagged" square lattice with two sites per unit cell [88], shown in figure 15, in which every other row is displaced to the right while allowing the requisite compression along the vertical direction. This lattice retains the straight horizontal filaments of the original square lattices but loses those in the vertical direction. It does not, however, lose any vertical SSSs because the SSSs from individual straight filaments are converted to ones like those of figure 5(e) on pairs of zigzagged filaments of which there are total of N_x under PBCs . These SSSs must be accompanied by zero modes in the spectrum, which show up as horizontal and vertical lines of zeros in the lowest-frequency mode and a vertical line of zeros in the second-lowest frequency mode as shown in figures 15(b) and (c). The vertical SSSs have no overlap with affine strain, and the lattice does not resist vertical compression. The result is that the elastic energy density is simply $f_{\rm el} = ku_{xx}^2/2$.

The kagome lattice offers more interesting variations [88, 83]. Figure 16(a) shows one such variation with intriguing properties. It consists of alternating rows of oppositely tilted distorted hexagons. It has rectangular symmetry with 6 sites per unit cell. As figure 16(b) shows, it has an unusual spectrum: its modes are fully gapped (except at $\boldsymbol{q} = 0$) near the origin but exhibit curved lines of zero modes at large $\boldsymbol{q}$. It has zero-frequency surface modes for surface wavenumbers in the gapped region but
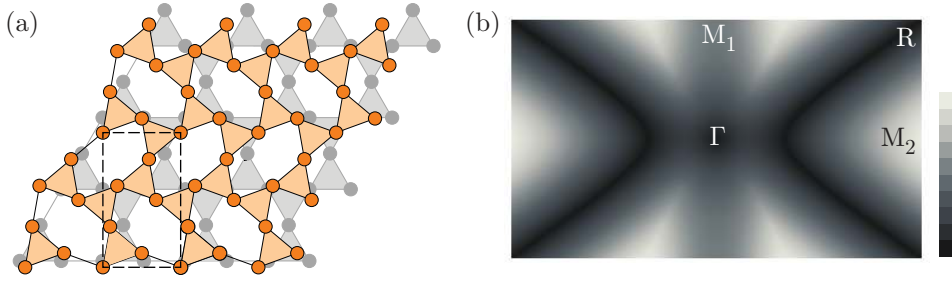
Figure 16. (a) An example of one of the many lattices that can be constructed from the kagome lattice without changing any bond lengths overlayed on an undistorted kagome lattice. This one is a stacked lattice with alternating rows of oppositely tilted hexagons. (b) Density map of the lowest-frequency band showing the gapped spectrum near the origin and two curved lines of zero modes passing between two corners. *Adapted from reference [83]*

not in the ungapped region. Curiously, the elastic energy density is identical to that of the twisted kagome lattice even though it has a lower symmetry.

The square and kagome lattice are the two-dimensional Maxwell lattices with the smallest unit cells. As discussed above, the kagome lattice can be distorted in various ways to produce larger-unit-cell Maxwell lattices, but there are many other lattices including random ones [89] that can be created. An intriguing set of periodic Maxwell lattices [69] are those arising from rational approximates to Penrose rhombohedral tilings [90] that approach a quasi-crystalline lattice with 5-fold symmetry [91, 92, 93]. A unit cell for the second periodic approximate with 80 sites and 160 bonds per cell is shown in figure 17. These periodic lattices, which can be constructed via projection from a five-dimensional cubic lattice [94], all have an average coordination of exactly four even though the coordination of local sites varies from three to as high as ten. The size of the unit cell increases rapidly from $N = 30$ in the first approximate to $N = 25840$ in the eighth approximate. Each of the approximates is a legitimate periodic lattices with a full set of phonon branches with dispersions depending on lattice wavenumber $\boldsymbol{q}$. They can also be interpreted as a single-cell system under toroidal PBCs that approach the infinite-cell quasicrystalline limit. In this interpretation, which we pursue here, only the $\boldsymbol{q} = 0$ part of the spectrum is of physical interest as is the case for periodic approximates to randomly packed spheres at jamming. These lattices have a number of interesting properties: (1) their undistorted versions have of order $\sqrt{N}$ SSSs and zero modes, but none of the SSSs overlap with affine strain, and all elastic moduli are zero, much as in rigidity percolation. (2) Randomizing site positions removes all but the two required SSSs and zero modes. The two SSSs overlap with affine strain to produce two independent positive eigenvalues of the elasticity matrix, one corresponding in the large N limit to the bulk modulus with associated eigenvector of pure compression and one to a shear modulus with associated shear eigenvector. The bulk modulus increases with N reaching a saturation value at $N \approx 10^4$. The shear modulus on the other hand approaches zero as $1/N$. The latter behavior is required by 5-fold-symmetric quasicrystalline limit whose elasticity must be isotropic with both shear moduli equal. Because there are only two SSSs, one shear modulus must be zero if the bulk modulus is nonzero, and the other must approach zero with N. This is essentially the same behavior observed in randomly packed spheres at the jamming threshold with $z = 2d$ [34, 35].
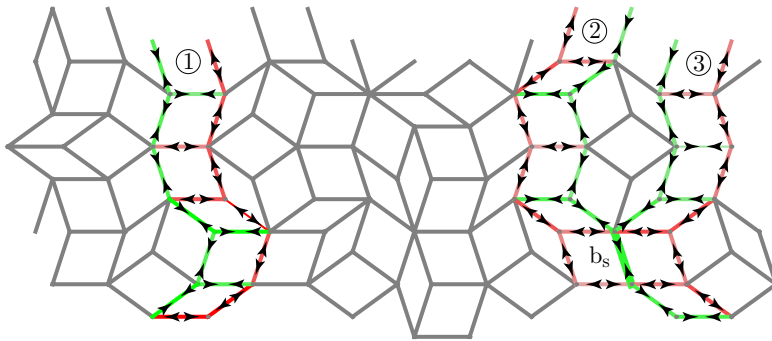
Figure 17. (color online) Unit cell of the second periodic approximant of the Penrose tiling showing SSSs (circled 1, 2, and 3). In all states, stress is localized on vertical ladders with different signs of stress on opposite sides as in figure 5(c). States 2 and 3 share the bond marked b$_s$, and are not orthogonal. They can be orthogonalized to produce states mostly, but not completely localized on the two ladders. *From reference [69]*

6. Topological phonons

Twisting the kagome lattice gaps all zero modes of the untwisted lattice except those at $q = 0$. This gapping is reminiscent of that of the electron spectrum in systems like polyacetylene [52, 95], quantum Hall materials [50, 51] and topological insulators [53, 54, 55, 56, 57, 58], which is associated with the appearance of topologically protected zero modes at free boundaries and at boundaries separating two topological classes. An interesting and natural question is then whether or not the phonon spectra of Maxwell lattices can be gapped in different ways to produce distinct topological classes with protected boundary modes. The answer is yes they can be, and this section, which is mostly based on reference [60], will explore both how they can be constructed and the nature of their interface states.

6.1. A one-dimensional Model

We begin with a one-dimensional model whose phonon spectrum (including both positive and negative frequencies) is identical to that of the one-dimensional Su-Schrieffer-Heeger model for polyacetylene [52, 95] schematically depicted in figures 18(a) and (b). Our model, depicted in figures figure 18(c) and (d), consists of rigid bars of length r that can rotate freely about fixed positions, separated by a distance $a/2$, on a one-dimensional periodic lattice. The ends of neighboring bars are connected by harmonic springs whose lengths are adjusted so that the equilibrium configuration is one in which alternate rods make an angle $\bar{\theta}$ with the upward or downward normals, creating 2-site unit cells of length $2a$. Bars tilt towards the right if $\bar{\theta} > 0$ and to the left if $\bar{\theta} < 0$. Each rod s has one degree of freedom $\theta_s = \bar{\theta} - \delta\theta_s$, and each spring provides one constraint. Under periodic boundary conditions, the number N of rods equals the number N_B of springs. In the linearized limit, the compatibility matrix with components $C_{\beta s}$ connects the stretch in spring β with rotations of rod s: $\delta l_\beta = C_{\beta s}\delta\theta_s$, and the equilibrium matrix $Q_{s\beta}$ relates torques on rod s to tensions t_β in spring β: $\tau_s = -Q_{s\beta}t_\beta$. With appropriate sign convention for the torque, $C_{\beta s} = Q_{\beta s}^T$. In a state of self stress, springs are under tension, but there are no torques on the rods.
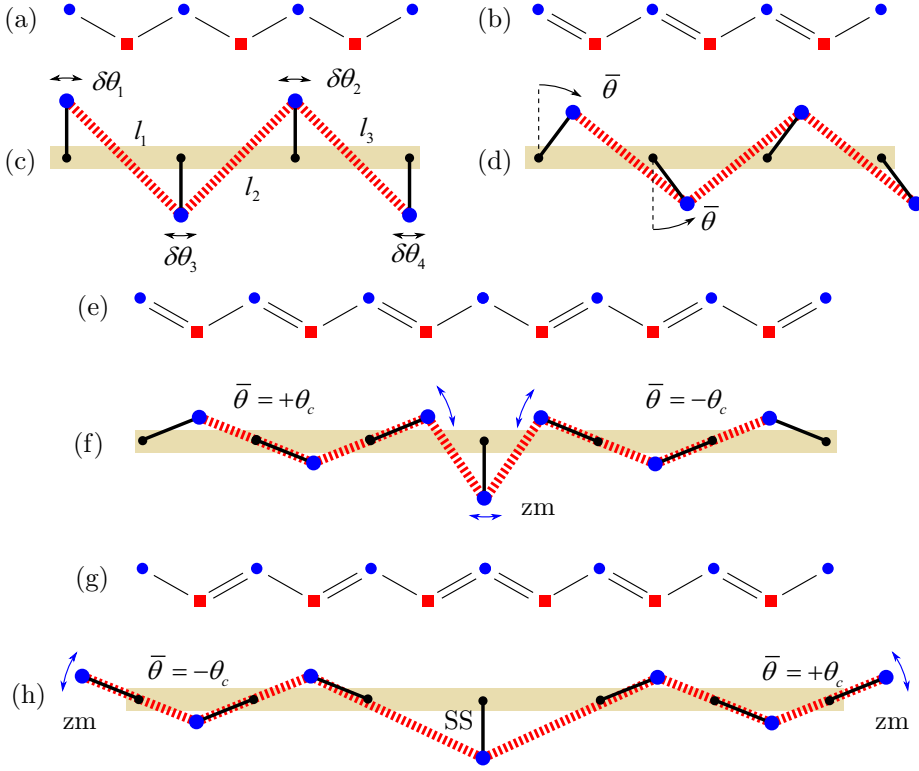
Figure 18. (a) and (b) depict the SSH model of polyacetylene, with A and B sublattices indicated by blue circles and red squares, respectively. (a) describes the gapless state with all bonds identical, while (b) describes the gapped AB dimerized state, with double (single) bonds on the AB (BA) bonds. The BA dimerized state with single and double bonds interchanged is not shown. (c) and (d) show the 1D isostatic lattice model in which masses, represented by the larger blue dots, are connected by springs in red and are constrained to rotate about fixed pivot points, represented by small black dots. (c) is the gapless high-symmetry state with $\bar{\theta} = 0$, and (d) is the gapped lower-symmetry phase with $\bar{\theta} > 0$. (c) and (d) are equivalent to (a) and (b) if we identify the masses (springs) with the A (B) sublattice sites. (e) shows a domain wall in polyacetylene connecting the AB and BA dimerized states. There is a topologically protected zero-energy state associated with the A sublattice at the defect. (f) shows the equivalent state for the mechanical model with a topologically protected zero-frequency mode at the domain wall connecting a $\bar{\theta} = +\theta_c$ lattice with a $\bar{\theta} = -\theta_c$ lattice. (g) shows a domain wall connecting the BA and AB dimerized states, which has a zero energy state associated with the B sublattice. (h) shows the equivalent isostatic state with a state of self-stress (SS) at the domain wall and zero modes at the end so that Index count $N_0 - N_S = 1$ is satisfied. *Adapted from reference [60]*

The Index theorem thus applies directly to this system. Under periodic boundary conditions $N_B = N$ and $N_0 = N_S$. Cutting one bond creates a free lattice with $N_0 = N_S + 1$. Thus, if there are no SSSs, the free system must have one zero mode, which can either be a mode in the bulk spectrum or a surface mode on one of the boundaries. But what determines whether it is localized on the right or left boundary? As we shall now, it is the topological class.

We proceed now to a more detailed analysis of the our model. The components of the compatibility matrix at rest angle $\bar{\theta}$ are

$$C_{\beta s}(\bar{\theta}) = -c_1(\bar{\theta})\delta_{\beta,s} + c_2(\bar{\theta})\delta_{\beta+1,s}, \tag{6.1}$$

where it is understood that rotations of "upward" ("downward") pointing rods are clockwise (clockwise) and

$$c_{1(2)} = \frac{(a \pm 2r\sin\bar{\theta})r\cos\bar{\theta}}{\sqrt{a^2 + 4r^2\cos^2\bar{\theta}}}. \tag{6.2}$$

Thus $|c_1| > |c_2|$ for all $0 < \bar{\theta} < \pi$, and $|c_1| < |c_2|$ for all $-\pi < \bar{\theta} < 0$. The energy of the system (contained entirely in the stretching of the springs) is then

$$E = \tfrac{1}{2}k\sum_{\beta}(\delta l_\beta)^2 = \tfrac{1}{2}k\sum_{s}(c_1\delta\theta_s - c_2\delta\theta_{s+1})^2. \tag{6.3}$$

The Fourier transform of $C_{\beta,s}$ is

$$C(q) = -c_1 + \mathrm{e}^{iqa}c_2, \tag{6.4}$$

and bulk phonon modes have frequency

$$\omega(q) = \pm|C(q)| = \pm\sqrt{(c_1 - c_2)^2 + 4c_1c_2\sin^2(qa/2)}, \tag{6.5}$$

(for unit mass), where $-\pi/a < q \leq \pi/a$. When $\bar{\theta} = 0$ (vertical rods), $c_1 = c_2$, the energy becomes invariant with respect of $\delta\theta_s \to \delta\theta_s + \delta$ for every s, and there is necessarily a bulk zero mode at $q = 0$ - this in spite of the fact that the bases of the rods are anchored, breaking translational invariance. For other values of $\bar{\theta}$, the phonon spectrum is fully gapped.

In a finite system, the compatibility matrix can be expressed in the form of (5.15) with $\mathbf{C}_{11} = -c_1$ and $\mathbf{C}_{12} = c_2$. The decay length of the surface state is determined by $c_1 - \lambda c_2 = 0$ or $\lambda = c_1/c_2 = e^{-\kappa a}$ $(e^{\kappa a})$ for states localized on the left (right) boundary. Thus, the one zero mode is on the left if $|c_1| < |c_2|$ and on the right for $|c_1| > |c_2|$. The left zero mode is particularly easy to see at the critical angle $\theta_c = -\sin^{-1}[a/(2r)]$ at which $c_1 = 0$ as shown in figure 18(s). The equilibrium matrix $\mathbf{Q} = \mathbf{C}^T$ for a finite system has no zero modes, and there are no SSSs as required by the Index count. This follows because $\mathbf{C}_{11}t_1 = 0$ for any $\boldsymbol{t}$ in the null space of $\mathbf{Q}$. Then the equation $-\mathbf{C}_{12}t_n + \mathbf{C}_{11}t_{n+1} = 0$ sets all t_n for $n > 1$ equal to zero. Under periodic boundary conditions, there must be one localized state of self stress for each localize zero mode.

But what does this have to do with topology? The compatibility matrix $C(q) \equiv |C(q)|^{i\phi}$ (or more generally its determinant) maps points in the Brillouin zone $(-\pi/a < q \leq \pi/a)$ to a path in the complex plane. Since it depends on e^{iqa}, the path will be a closed and return to its starting point as q advances between equivalent points in the zone $[q \to q + (2\pi/a)]$. These curves are characterized by an integer winding number:

$$n = \frac{1}{2\pi}\int_0^{2\pi}d\phi = \frac{1}{2\pi i}\int_0^{2\pi/a}dq\frac{\mathrm{d}}{\mathrm{d}q}\mathrm{Im}\ln\det C(q), \tag{6.6}$$

which for the $C(q)$ of (6.4) is either $+1$ or 0. Clearly $n = 0$ if the path in the complex plane does not enclose the origin, and $n = 1$ if it does. The first case occurs whenever
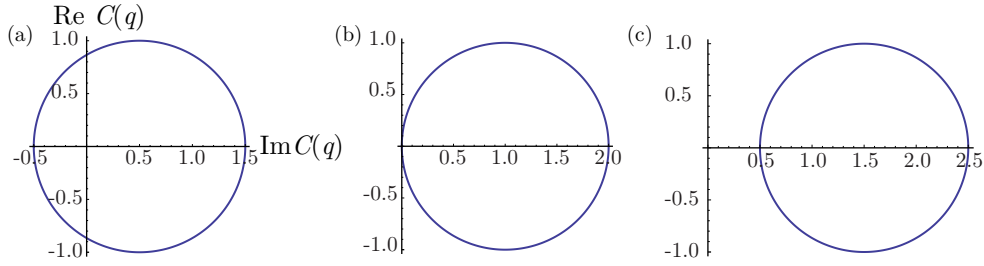
Figure 19. Contour plots in the complex plane of $C(q)$ for complete circuit of q from $q = 0$ to $q = 2\pi/a$. (a) $c_2 = 1.0$ and $c_1 = 0.5 < c_2$; the circuit contains the origin and the topological charge is $n = 1$. (b) $c_1 = c_2 = 1.0$; this is the transition case in which the contour just touches the origin, and $n = 0$. (c) $c_1 = 1.5 > c_2 = 1.0$; the circuit does not contain the origin and $n = 0$. Note the circuits begin with $q = 0$ on the far left and circulate counterclockwise.

$|c_1| > |c_2|$ and the second whenever $|c_1| < |c_2|$ as shown in figure 19. When $|c_1| = |c_2|$, the boundary of the curve passes through the origin. The winding number is thus a topological invariant equal to 1 for all $-\pi < \bar\theta < 0$ and to 0 for all $0 < \bar\theta < \pi$. The only way it can change values is by passing through the critical angles $\bar\theta = 0$ or $\bar\theta = \pi$ (bars lie along the horizontal axis). When $n = 0$, the zero mode is on the right and if $n = 1$, the zero modes is on the left. The connection between the topological invariant and the existence of zero modes is easy to see in this case. A zero surface mode exists if there is a solution to $c(\lambda) = c_1 - c_2\lambda = 0$ with $|\lambda| < 1$. The compatibility matrix is simply $C(q) = c(\lambda = e^{iqa})$, and along the closed path it describes in the complex plane, $|\lambda| = 1$. In the interior of the path $|\lambda| < 1$. Thus, if the path encloses the origin, which is the point at which $c(\lambda) = 0$, the solution for λ will have a magnitude less than one. A complementary perspective, based on the Cauchy argument principle, is discussed in Appendix D,

Here we considered the winding number associated with $C(q)$. We could equally well have considered that associated with the equilibrium matrix $Q(q) = C^*(q)$. Because e^{-iqa} winds clockwise rather than counter clockwise with increasing a, its winding number is either -1 or 0, with -1 corresponding to $|c_1| < |c_2|$. Thus the surface state is at the left when the winding number of Q is -1. We will use a generalization of the Q-winding number in our characterization of topological classes of kagome lattices in what follows.

As is well known for the SSH model [52, 96], an interface between the two dimerizations binds a zero mode, as indicated. Similarly, the interface separating the two signs of $\bar\theta$ does as well. This is most easily seen for $\bar\theta = \pm\theta_c$ where the springs are colinear with the bars, so that c_1 or $c_2 = 0$. Figure 18(f) shows a domain wall between $+\theta_c$ and $-\theta_c$, in which the center two sites share a localized zero mode. Figure 18(h) shows an interface between $-\theta_c$ and $+\theta_c$ with a state of self-stress localized to the middle three bonds, in addition to floppy modes localized at either end. As long as there is a bulk gap, the zero modes cannot disappear when $\bar\theta$ deviates from $\pm\theta_c$. The zero modes remain exponentially localized, with a localization length, $l = a/\ln|c_1/c_2|$, that diverges when $\bar\theta \to 0$.

6.2. Topological lattices

We have just seen the intimate connection between topological properties of the compatibility or equilibrium matrices and zero-modes at boundaries in a one-dimensional system. Here we discuss how these ideas can be extended to higher-dimensional Maxwell lattices. We will for the most part only quote results, and not provide details of how they were obtained. The latter can be found in reference [60]. There are two significant differences between these lattices and those in one dimension. First, because $\mathbf{Q}(\boldsymbol{q})$ (or $\mathbf{C}(\boldsymbol{q})$) depends on the vector wavenumber $\boldsymbol{q}$ with two rather than one independent component, topological characterization will require a vector rather than a scalar winding number. Second there are boundary surface modes imposed by the Index theorem that are required whether or not lattices have any topologically properties. We will thus need to divide the surface mode count into those parts imposed by the Index theorem and those parts implied by topological considerations. The result is that topology cannot change the global count of the Index theorem, but it can move zero modes from one boundary to another and give rise to topologically protected zero modes at interfaces between two different topological classes.

6.2.1. Topological and total mode count

To unify the treatment of zero modes arising from mismatch of sites and bonds and those that arise in locations where there is no local mismatch, reference [60] generalized the Index theorem so that it determines a zero mode count $\nu^S = N_0^S - N_S^S$ in a subsystem S of a larger system. This is well defined provided the boundary of S is deep in a gapped phase where zero modes are absent. This count has the two separate contributions just discussed:

$$\nu^S = \nu_L^S + \nu_T^S, \tag{6.7}$$

where ν_L^S is a local count of sites and bonds in S and ν_T^S is a topological count, which depends on the topological structure of the gapped phases in the boundary of S. The topological contribution has a form similar to that of the one-dimensional system. For the periodic lattices we are considering, it is best expressed as a count per unit cell on an edge indexed by a reciprocal lattice vector $\boldsymbol{G}$ (i.e., $\boldsymbol{G}$ is normal to the surface with a magnitude of $2\pi/a_\perp$, where $a_\perp$ is the distance between lines of cells identical to the line of surface cells),

$$\tilde{\nu}_T^S = \nu^S/N_{\text{cell}} = \boldsymbol{G} \cdot \boldsymbol{R}_T/(2\pi), \tag{6.8}$$

where N_{cell} is the number of surface unit cells and $\boldsymbol{R}_T$, a generalization of the one-dimensional winding number, is a lattice vector

$$\boldsymbol{R}_T = \sum_i n_i \boldsymbol{a}_i, \tag{6.9}$$

where $\boldsymbol{a}_i$ are the primitive translation vectors and

$$n_i = \frac{1}{2\pi \mathrm{i}} \oint_{C_i} d\boldsymbol{q} \cdot \text{Tr}[\mathbf{Q}(\boldsymbol{q})^{-1} \nabla_{\boldsymbol{q}} \mathbf{Q}(\boldsymbol{q})]. = \frac{1}{2\pi} \oint_{C_i} d\boldsymbol{q} \cdot \nabla_{\boldsymbol{q}} \phi(\boldsymbol{q}), \tag{6.10}$$

where $\phi(\boldsymbol{q})$ is the phase of $\det \mathbf{Q}(\boldsymbol{q})$ ($\mathbf{Q}(\boldsymbol{q}) = |\mathbf{Q}(\boldsymbol{q})|^{\mathrm{i}\phi(\boldsymbol{q})}$). Here C_i is a cycle of the BZ connecting $\boldsymbol{q}$ and $\boldsymbol{q} + \boldsymbol{B}_i$, where $\boldsymbol{B}_i$ is a primitive reciprocal vector satisfying

$\boldsymbol{a}_i \cdot \boldsymbol{B}_j = 2\pi\delta_{ij}$ ($\boldsymbol{B}_1 = -\boldsymbol{G}_2$ and $\boldsymbol{B}_2 = \boldsymbol{G}_1$ in figure 11a). The n_i are winding numbers of the phase of det $\mathbf{Q}(\boldsymbol{q})$ around the cycles of the BZ, where $\mathbf{Q}(\boldsymbol{q})$ is the equilibrium matrix in a Bloch basis. This winding number is independent of path, and thus independent of $\boldsymbol{q}$ so long as the spectrum is gapped everywhere except the origin. The zero-mode at the origin of $\boldsymbol{q}$ is not topologically protected (i.e, it can be gapped by a weak potential breaking translational symmetry), so it does not cause any problems. It is possible, however, for there to be topologically protected gapless points. These would be point zeros around which the phase of det $\mathbf{Q}(\mathbf{k})$ advances by 2π. These lead to topologically protected bulk modes that form the analog of a "Dirac semimetal" in electronic systems like graphene [53, 71, 72, 73, 74, 75, 76, 77, 78]. These singularities could be of interest, but they do not occur in lattices derived from the kagome lattice we study below. They do, however, occur in modified square lattices [70] of the type shown in figure 3 considered in reference [49] and in the pyrocholore lattice [82].

In general, the winding number is not gauge invariant and depends on how the sites and bonds are assigned to unit cells. It is, however, possible to adopt a "standard unit cell" with basis vectors $\boldsymbol{r}_{\mu(\beta)}$ for the n_s sites ($n_b = dn_s$ bond centers) per cell for which the "dipole" moment of the site and bond charges, $\boldsymbol{R}_{\text{stan}} = d\sum_\mu \boldsymbol{r}_\mu - \sum_\beta \boldsymbol{r}_\beta$, is equal to zero. The two unit cells of figure 10 satisfy this zero dipole condition even after being distorted to those of the twisted lattice. $\mathbf{Q}(\boldsymbol{q})$ is defined using Bloch basis states $|\boldsymbol{q}, a = \mu, \beta\rangle \propto \sum_l \exp[\mathrm{i}\boldsymbol{q} \cdot (\boldsymbol{R}_l + \boldsymbol{r}_a)]|\boldsymbol{R}_l + \boldsymbol{r}_a\rangle$, where $\boldsymbol{R}_l$ is a Bravais lattice vector. In this gauge, $\boldsymbol{R}_T$ is uniquely defined, and the zero-mode count is given by equations (6.7) to (6.9).

Because $\boldsymbol{R}_{\text{stan}}$ is zero, we could equally well use a basis in which all $\boldsymbol{r}_\mu$ and $\boldsymbol{r}_\beta$ are simply zero. This is in fact the basis we use for all of the calculations presented here. It should be noted that it is not always possible to find a symmetric "standard" unit cell with a vanishing dipole moment defined in terms of charges at sites and bond centers. Indeed, there is no such cell for the SSH model or for 3D pyrochlore lattices. Not having such a standard cell is not a problem, however. The number and the nature of surface modes do not depend on the choice of a "standard" or reference unit cell and are unambiguous. The easiest choice is usually to set the positions of all of the sites and bonds in the unit cell to be zero. As discussed in Appendix D, det $\mathbf{C}$ for different unit cell choices, such as those used to calculate the zero surface modes in section 5.3.2, will have different phase factors, which account for the differences in the topological integral of (6.10) for different choices of unit cells..

The local count, ν_L^S, depends on the details of the termination at the surface and can be determined by evaluating the macroscopic "surface charge" that arises when charges $+d$ (-1) are placed on the sites (bonds) in a manner analogous to the "pebble game" [11]. This can be found by defining a bulk unit cell with basis vectors $\tilde{\boldsymbol{r}}_a$ that accommodates the surface with no leftover sites or bonds (see figures 14 and 20) as discussed in section 5.3.2. This unit cell depends on the surface termination and, in general, will be different from the "standard" unit cell (figure 10) used for the calculation of ν_T^S. The local count is then the surface polarization charge given by the dipole moment $\boldsymbol{R}_L$ per unit cell:

$$\tilde{\nu}_L \equiv \nu_L^S/N_{\text{cell}} = \boldsymbol{G} \cdot \boldsymbol{R}_L/2\pi, \tag{6.11}$$

where

$$\boldsymbol{R}_L = d \sum_{\text{sites } \mu} \tilde{\boldsymbol{r}}_\mu - \sum_{\text{bonds } \beta} \tilde{\boldsymbol{r}}_\beta. \tag{6.12}$$

The total zero-mode count on the surface then follows from equations (6.7), (6.8), and (6.11). The polarization of the standard cell is zero so that $\boldsymbol{R}_L = \boldsymbol{R}_L - \boldsymbol{R}_{\text{stan}}$ can be calculated from the displacements $\tilde{\boldsymbol{r}}_a - \boldsymbol{r}_a$ of the surface cell sites and bonds relative to those of the standard cell.

6.2.2. Constructing topological lattices The kagome lattice has three sites per unit cell, and displacing these sites while maintaining the size and shape of the unit cell creates different lattices, each of which can be smoothly connected with the other across domain walls. The twisted kagome lattice, with bond length increased by $1/\cos\alpha$ to connect smoothly with the untwisted lattice, is an example of this operation. The most general such lattice is described by four parameters (one site in the the unit cell can always be fixed). The most useful parametrization is one in which the "straightness" of the three sets of filaments are controlled individually. Such a set is depicted in figure 20. Displacing site 1 of the unit cell by $-\sqrt{3}x_1\boldsymbol{p}_1$, where $\boldsymbol{p}_1$ is the vector of length a perpendicular to lattice vector $\boldsymbol{a}_1$, "zigzags" the filaments parallel to $\boldsymbol{a}_1$. Though this operation leaves filaments parallel of $\boldsymbol{a}_3$ straight, it zigzags the filaments parallel to $\boldsymbol{a}_2$. The latter can be straightened by the simple operation of displacing site 2 along $\boldsymbol{a}_3$ by $x_1\boldsymbol{a}_3$, as shown in figure 20(a). This process is repeated to zigzag filaments parallel of $\boldsymbol{a}_2$ and $\boldsymbol{a}_3$ as shown in figures 20 (b) and (c). Finally the $1-2-3$ triangle can be isotropically expanded by displacing the three sites the same amount along directions $\boldsymbol{p}_1$, $\boldsymbol{p}_2$ and $\boldsymbol{p}_3$. The basis vectors for the unit cell are then

$$\boldsymbol{r}_\mu = \boldsymbol{r}_\mu^0 - \sqrt{3}x_\mu\boldsymbol{p}_\mu + x_{\mu-1}\boldsymbol{a}_{\mu+1} + (z/\sqrt{3})\boldsymbol{p}_{\mu-1}, \qquad (6.13)$$

where $\boldsymbol{r}_\mu^0$ (e.g., $\boldsymbol{r}_1 = \boldsymbol{a}_1/2$, $\boldsymbol{r}_2 = -\boldsymbol{a}_3/2$, $\boldsymbol{r}_3 = 0$) are the basis vectors of the untwisted unit cell and it is understood that all subscripts are evaluated mod 3. The bond vectors are then

$$\boldsymbol{b}_\beta = \boldsymbol{d}_{\beta+1} - \boldsymbol{d}_\beta = \tfrac{1}{2}\boldsymbol{a}_\beta - (-1)^{\text{Int}((\beta-1)/3)}[(x_{\beta+1} - x_{\beta-1} - z)\boldsymbol{a}_\beta + \sqrt{3}x_\beta\boldsymbol{p}_\beta], \quad (6.14)$$

where $\text{Int}(x)$ is the integer part of x and it is understood that $\boldsymbol{a}_{\beta+3} = \boldsymbol{a}_\beta$ and $\boldsymbol{p}_{\beta+3} = \boldsymbol{p}_\beta$. The expressions for $\boldsymbol{b}_\beta$ for $\beta = 4, 5, 6$ are obtained from those for $\beta = 1, 2, 3$ via the relation $\boldsymbol{b}_{\beta+3} = \boldsymbol{a}_\beta - \boldsymbol{b}_\beta$. The untwisted kagome lattice corresponds to $X = (x_1, x_2, x_3; z) = (0, 0, 0; 0)$ and the twisted kagome with twist angle $\alpha = \tan^{-1}(2\sqrt{3}x)$ to $X = (x, x, x; 0)$. For a lattice with straight filaments along $\boldsymbol{a}_1$ only, $X = (0, x_2, x_3; z)$ and similarly for straight filaments along $\boldsymbol{a}_2$ and $\boldsymbol{a}_3$. These lattices have SSSs and associated zero modes along a single direction in the Brillouin Zone. Moving off $x_1 = 0$ gaps the spectrum as shown in figure 21.

The topological polarization in terms of X is

$$\boldsymbol{R}_T = \frac{1}{2}\sum_{p=1}^{3}\boldsymbol{a}_p\,\text{sign}(x_p). \qquad (6.15)$$

This leads to the ternary phase diagram shown in figure 20(c) as a function of x_1, x_2, and x_3 for fixed $x_1 + x_2 + x_3$ and $z = 0$. It has eight octants corresponding to the eight possible sign combinations of (x_1, x_2, x_3). The $(+, +, +)$ and $(-, -, -)$ octants correspond to the class of the twisted kagome lattice. The remaining 6 octants are states that are topologically equivalent, but related to each other by C_6 rotations. Figure 21 shows representative structures for the $\boldsymbol{R}_T = 0$ phase (figure 21(a)), the $\mathbf{R}_T \neq 0$ phase (figure 21(c)), and the transition between them (figure 21(b)). The
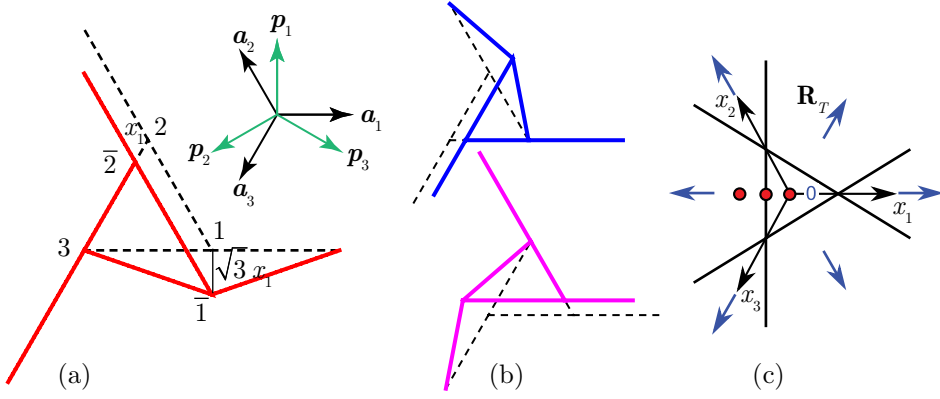
Figure 20. (a) and (b) depict the geometry used to derive equations (6.13) and (6.14). In (a), site 1 of the symmetric unit cell of figure 10(c) is displaced downward by $\sqrt{3}\,x_3\,\boldsymbol{p}_1$, perpendicular to the lattice vector $\boldsymbol{a}_1$, and site 2 is displaced along $\boldsymbol{a}_3$ by $x_1\boldsymbol{a}_3$. The result is that the filaments along $\boldsymbol{a}_2$ and $\boldsymbol{a}_3$ remain straight whereas those along $\boldsymbol{a}_1$ are zigzagged. (b) depicts similar displacements that zigzag only filaments along $\boldsymbol{a}_2$ or $\boldsymbol{a}_3$. (c) shows the ternary phase diagram for fixed $x_1 + x_2 + x_3 > 0$. The space enclosed by the central triangle corresponds to the to the state with $\boldsymbol{R}_T = 0$. The direction of $\boldsymbol{R}_T$ is the six sectors surrounding the central triangle are indicated by the blue arrows. The red dots from right to left correspond to the three lattices shown in the opposite order in figure 21
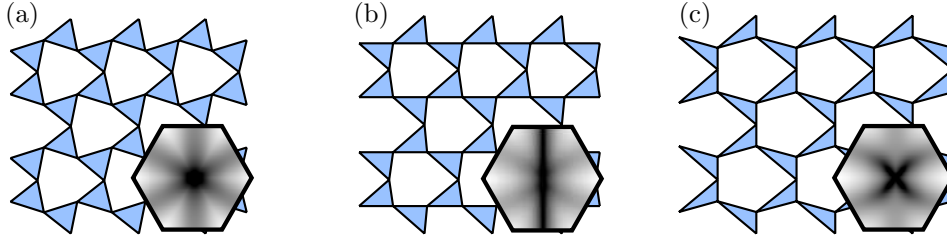

Figure 21. Representations of lattices and the density maps of their associated lowest frequency modes for (a) a twisted kagome lattice with $X = (0.1, 0.1, 0.1; 0)$ and $\boldsymbol{R}_T = 0$ (right-most red dot in figure 20(c)), (b) a critical lattice with $X = (0, 0.1, 0.1; 0)$ (central red dot), and (c) a topological lattice with $X = (-0.1, 0.1, 0.1; 0)$ and $\boldsymbol{R}_T = -\boldsymbol{a}_1$ (left-most red dot). Note the isotropically gapped spectrum (except for the origin) of (a), the line of zero modes in (b), and the soft-mode cross in (c). *Adapted from reference [60]*

insets show density plots of the lowest frequency mode, which highlight the gapless point due to the acoustic mode in figure 21(a) and the gapless line due to states of self stress in figure 21(b). In figure 21(c), the gap vanishes only at the origin, but there is a low-frequency cross that arises because acoustic modes vary quadratically rather than linearly with $\boldsymbol{q}$ along its axes. This behavior will be discussed in the next section.

We are now in a position to analyze zero interface modes for different X. Surfaces in the twisted-kagome octants are in the same class of those discussed in section 5.3.2 and in figure 14. The bonds and sites to be displaced to convert the standard unit
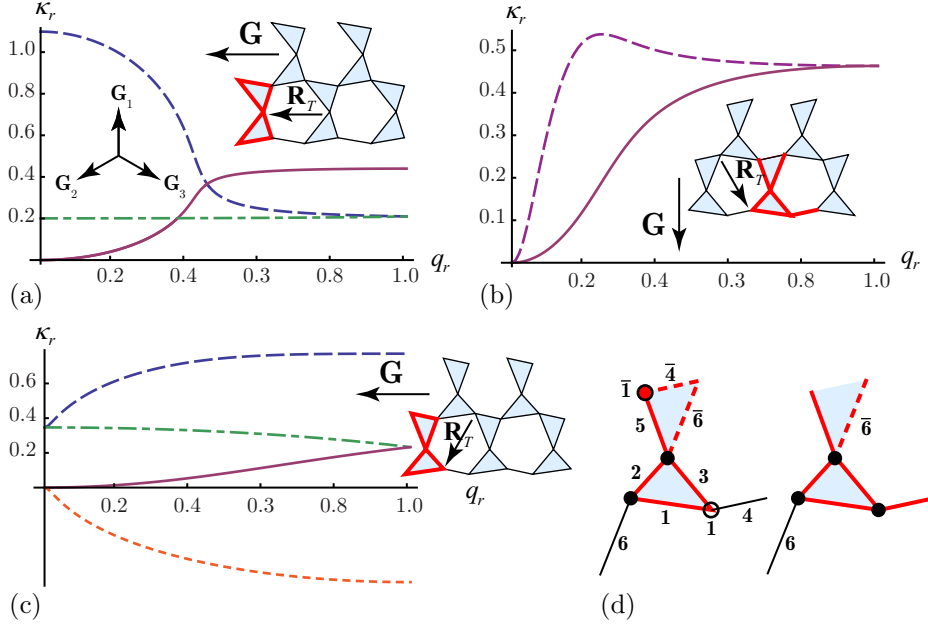
Figure 22. Real part of the reduces inverse penetration depth $\kappa_r = 2\kappa/G_S$ for various orientations of surfaces and $\boldsymbol{R}_T$ as a function of reduced surface wavenumber $q_r = 2q/G_S$, where G_S is the magnitude of the surface reciprocal lattice vector. In (a) the surface lattice vector $\boldsymbol{G} = \boldsymbol{G}_2 - \boldsymbol{G}_3$, $\boldsymbol{R}_T = -\boldsymbol{a}_1$, $\boldsymbol{G} \cdot \boldsymbol{R}_T/(2\pi) = 2$, and there are four zero surface modes. The opposite surface with $-\boldsymbol{G}$ has no zero modes. The full magenta curve is doubly degenerate with opposite imaginary parts, and the two dashed curves are not degenerate. (b) $\boldsymbol{G} = -\boldsymbol{G}_1$, $\boldsymbol{R}_T = \boldsymbol{a}_3$ and $\boldsymbol{G} \cdot \boldsymbol{R}_T/(2\pi) = 1$. There are two surface zero modes. (c) $\boldsymbol{G} = \boldsymbol{G}_2 - \boldsymbol{G}_3$, $\boldsymbol{R}_T = -\boldsymbol{a}_2$, $\boldsymbol{G} \cdot \boldsymbol{R}_T/(2\pi) = 1$, and there are three surface zero modes. The full magenta curves in (a) to (c) correspond to acoustic surface states, and in all cases κ_r approaches 0 as q_r^2 as $q_r \to 0$. (d) shows how to construct the dipole moments $\boldsymbol{R}_L$ for the surface unit cells in (a) to (c). On the left, black bonds **4** and **6** of the symmetric unit cell are, respectively, displaced by $\boldsymbol{a}_2$ and $-\boldsymbol{a}_3$ while the circled site 1 is displaced by $\boldsymbol{a}_2$ to produce the surface unit cell of (a) and (c) with $\boldsymbol{R}_L = 2\boldsymbol{a}_2 - (\boldsymbol{a}_2 - \boldsymbol{a}_3) = -\boldsymbol{a}_1$ and $\tilde{\nu}_L^S = 2$. On the right, the black bond **6** is displaced through $-\boldsymbol{a}_3$ to produce the surface unit cell of (b) with $\boldsymbol{R}_L = \boldsymbol{a}_3$ ad $\tilde{\nu}_L = 1$.

Table 1. Reciprocal lattice vectors $\boldsymbol{G}$ indexing surfaces, dipole moment $\boldsymbol{R}_L$, and local count $\tilde{\nu}_L$ for the seven surfaces cells of figure 14(a). The reciprocal lattice vectors $\boldsymbol{G}_1$, $\boldsymbol{G}_2$, and $\boldsymbol{G}_3$ are depicted in figure 11 and the Bravais lattice vectors $\boldsymbol{a}_1$, $\boldsymbol{a}_2$, and $\boldsymbol{a}_3$ in figure 10.

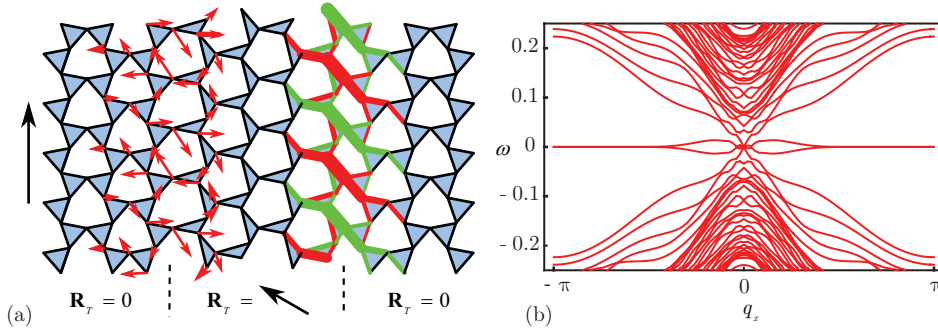| cell	1	2	3	4	5	6	7
$\boldsymbol{G}$	$-\boldsymbol{G}_1$	$\boldsymbol{G}_1$	$\boldsymbol{G}_1$	$\boldsymbol{G}_2 - \boldsymbol{G}_3$	$\boldsymbol{G}_3 - \boldsymbol{G}_2$	$\boldsymbol{G}_3 - \boldsymbol{G}_2$	$-\boldsymbol{G}_1$
$\boldsymbol{R}_L$	$\boldsymbol{a}_3$	$\boldsymbol{a}_2$	$-\boldsymbol{a}_3$	$-\boldsymbol{a}_1$	$\boldsymbol{a}_1$	$\boldsymbol{a}_1$	$\boldsymbol{a}_3 - \boldsymbol{a}_2$
$\tilde{\nu}_L$	1	1	1	2	2	2	2

Figure 23. Zero modes at domain walls. (a) shows a lattice with periodic boundary conditions and two domain walls, the left one between $(.1, .1, .1; 0)$ and $(.1, .1, -.1; 0)$ with zero modes and the right one between $(.1, .1, -.1; 0)$ and $(.1, .1, +.1; 0)$ with states of self stress. The zero mode eigenvectors at $q_x = \pi$ are indicated for the floppy mode (arrows) and the state of self-stress (red (+) and green (-) thickened bonds). (b) shows the vibrational mode dispersion as a function of q_x. *From reference [60]*

cell to a surface one are depicted for two cells in figure 22(d). Table 1 lists the surface polarization vector, the surface reciprocal lattice vector $\boldsymbol{G}$, and the reduced surface index $\tilde{\nu}_L$ (which because there are no SSSs equals the number of zero modes per surface cell) for the seven surface cells shown in figure 14. As required, the count corresponds to the number obtained by direct evaluation.

Converting $\boldsymbol{R}_T = 0$ to $\boldsymbol{R}_T \neq 0$ modifies the surface count by the term $\boldsymbol{R}_T \cdot \boldsymbol{G}/(2\pi)$ in $\tilde{\nu}$. Since $\boldsymbol{G}$ has opposite signs on opposite parallel surfaces, the effect is to move zero surface modes between the two surfaces while keeping the total count fixed as required. Figure 22 plots the real part of the surface penetration wavenumber, κ, of three representative surfaces and orientations of $\boldsymbol{R}_T$ relative to the surface normals. In figure 22(a), $\boldsymbol{R}_T$ is parallel to $\boldsymbol{G}$ of a vertical surface, and there are four rather than the two zero modes of the non-topological surface of figure 14 with surface cell 4. Thus on the opposite surface (with surface cells 5 an 6 in figure 14), there are no zero modes. Similarly in figure 22(b) with $\boldsymbol{R}_T$ at 30° to $\boldsymbol{G}$ of a horizontal surface, there are two zero surface modes whereas the same surface (cell 1 in the $\boldsymbol{R}_T = 0$ lattice of figure 14) has only one. Finally figure 22(c) with $\boldsymbol{R}_T$ at 60° to $\boldsymbol{G}$ of a vertical surface, there are three rather than two surface modes per unit cell. A striking feature is that the curves versus the surface wavenumber q of κ for acoustic modes when $\boldsymbol{R}_T \neq 0$ is that their approach to 0 as $q \rightarrow 0$ is quadratic rather than linear in q. This is a consequence of the modes with q^2 dispersion shown in figure 21(c).

We next examine the modes of the deformed kagome lattice at the boundary between two different topological classes. Figure 23 shows a system with periodic boundary conditions in both directions that has two domain walls separating $X = (.1, .1, .1; 0)$ from $X = (.1, .1, -.1; 0)$, exhibiting zero modes and the other exhibiting states of self stress. Since there are no broken bonds, the local count is $\nu_S^L = 0$, but the global count remains zero so that the number of states of self stress on the second domain wall equals the number of zero modes the first. On the two domain walls, (6.11) predicts

$$\tilde{\nu}_T = \boldsymbol{G} \cdot (\boldsymbol{R}_T^1 - \boldsymbol{R}_T^2) = +1(-1), \tag{6.16}$$

for the left (right) domain wall, where $\boldsymbol{R}_T^1$ and $\boldsymbol{R}_T^2$ characterize the material to the left

and right of the domain wall, respectively. Figure 23' shows the positive and negative vibrational frequencies of $\mathbf{D}$ and $\mathbf{Q}^T \cdot \mathbf{Q}$, which has zero modes when there are states of self stress, as a function of the momentum q_x parallel to the domain wall. In the vicinity of $q_x = 0$ the zero modes on the two domain walls couple and split because their penetration depth diverges as $k_x \to 0$. The eigenvectors for the zero modes at $k_x = \pi$ are indicated in figure 23 by the arrows and the thickened bonds.

6.2.3. Continuum limit As we have seen, there are two related long-wavelength properties of the topological lattices that differ from their non-topological counterparts: Their spectrum has peculiar low-frequency lobes [figure 21(c)], and penetration wavenumbers of their acoustic modes approach zero with q as q^2 rather than as q. These properties must be reflected in the in the form of the long-wavelength elastic energy, and indeed they are. For simplicity we focus on states with $X = (x_1, x_2, x_2; 0)$, where $x_2 > 0$ is fixed and x_1 is allowed to vary. The elastic energy density f can be written

$$f = \tfrac{1}{2}K[(u_{xx} - r_1 u_{yy})^2 + 4r_4 u_{xy}^2], \tag{6.17}$$

where $r_1 \propto x_1$ for small x_1, while $r_4 > 0$ and K are positive and smoothly varying near $x_1 = 0$. Thus, the $\boldsymbol{R}_T = 0$ and $\boldsymbol{R}_T \neq 0$ sectors are distinguished by the sign of r_1. The Guest mode [49], for which $f = 0$, corresponds to shape distortions with $u_{xx} = r_1 u_{yy}$ and $u_{xy} = 0$. When $r_1 > 0$, u_{xx} and u_{yy} have the same sign, and the distortion has a negative Poisson ratio [86], expanding or contracting in orthogonal directions (a feature shared by the twisted kagome lattice [83]); when $r_1 < 0$, u_{xx} and u_{yy} have the same sign, and the distortion has the more usual positive Poisson ratio. Finally when $r_1 = 0$, uniaxial compressions along y costs no energy. Note that this energy consists of two independent positive definite quadratic forms as it must in a periodic isostatic lattice with two SSSs. Figure 24 shows the effects of evolution of the nonlinear Guest mode in response to compression along the x-axis of various topological lattices.

Expanding $\det \mathbf{C}$ for small $\boldsymbol{q}$ provides useful information about the bulk- and surface-mode structure. To order q^3,

$$\det \mathbf{C} = A[q_x^2 + r_1 q_y^2 + i\gamma(q_x^3 - 3q_x q_y^2)] + O(q^4), \tag{6.18}$$

where $A > 0$ and $\gamma > 0$ for small x_1. The quadratic part of the equation follows from (4.15) and the elastic matrix, (3.5), with $K_{xxxx} = K$, $K_{yyyy} = r_1^2 K$, and $K_{xyxy} = r_4 K$, associated with the free energy of (6.17). Long-wavelength zero modes are solutions of $\det \mathbf{C} = 0$. The quadratic term, which corresponds to the elastic theory reveals an important difference between the bulk acoustic modes of $\boldsymbol{R}_T = 0$ and $\boldsymbol{R}_T \neq 0$. In the former case, $r_1 > 0$, $\det \mathbf{C} = 0$ only at $\boldsymbol{q} = 0$. For $r_1 < 0$, though, to order q^2, $\det \mathbf{C} = 0$ for $q_x = \pm\sqrt{|r_1|}q_y$, so the elastic theory predicts lines of gapless bulk modes. The degeneracy is lifted by the q^3 term, leading to a q^2 dispersion along those lines, which can be seen by the cross in the density map of figure 21(c).

As we have seen, $\det \mathbf{C}(\boldsymbol{q} \to 0)$ vanishes for complex wavenumbers associated with zero-frequency Rayleigh surface waves. Writing $\boldsymbol{q} = q_\perp \hat{\boldsymbol{n}} + q_{||}\hat{z} \times \hat{\boldsymbol{n}}$ for a surface whose outward normal $\hat{\boldsymbol{n}}$ makes an angle θ with $\hat{x}$, there is an $\omega = 0$ Rayleigh wave with penetration depth $\kappa^{-1} = |\text{Im}\, q_\perp|^{-1}$ if $\text{Im}\, q_\perp < 0$. To order $q_{||}^2$ there are two solutions,

$$q_\perp^\pm = i\kappa \frac{\sin\theta \pm i\sqrt{r_1}\cos\theta}{\cos\theta \mp i\sqrt{r_1}\sin\theta}q_{||} + \frac{\sqrt{r_1}(3 + r_1)\gamma}{2(\cos\theta \pm i\sqrt{r_1}\sin\theta)^3}q_{||}^2. \tag{6.19}$$
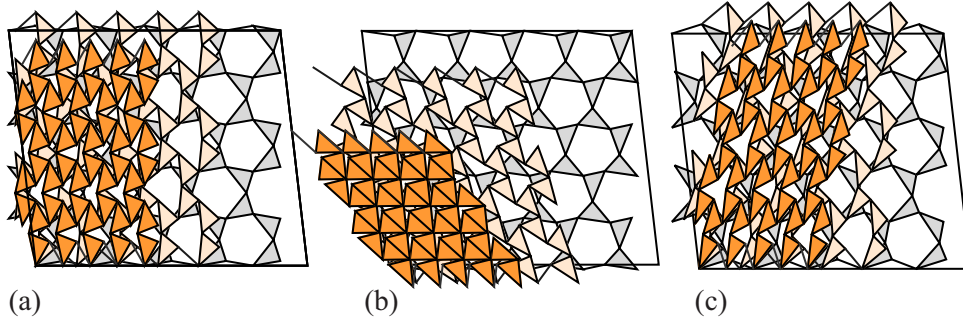
Figure 24. Evolution of the nonlinear Guest mode in topological lattices in response to uniform compression along the x-axis. (a) $X = \{-0.05, 0.05, 0.05\}$: Small compression along x produces area change along with pure shear with a positive Poisson ratio in agreement with (6.17). At large compression, there is contraction along both x and y reflecting a nonlinear negative Poisson ratio. (b) $X = \{0.05, -0.05, 0.05\}$: Compression along x now produces a simple shear component with length contraction in all directions (negative Poisson ratio). (c) $X = \{-0.1, 0.025, 0.075\}$: Compression along x now produces some simple shear, but the Poisson ratio $(-u_{yy}/u_{xx})$ remains positive for all compressions.

When $r_1 > 0$, the linear term is always finite and nonzero, and $\mathrm{Im}\, q_\perp^\pm$ have opposite signs, indicating that there can be acoustic surface zero modes on all surfaces. These are the classical Rayleigh waves predicted by the elastic theory [59], with penetration depth $\mathrm{O}(q_{||}^{-1})$. When $r_1 < 0$, the linear term in $q_{||}$ is real and $\kappa_r = \mathrm{Im}\, q_\perp^\pm \propto q_{||}^2$. The number of long wavelength surface zero modes depends on the angle of the surface. When $|\theta| < \theta_c = \cot^{-1}\sqrt{|r_1|}$, $\mathrm{Im}\, q_\perp^\pm$ are both positive, and there are no acoustic surface zero modes. The opposite surface, $|\theta - \pi| < \theta_c$, has two acoustic surface modes. For $\theta_c < \theta < \pi - \theta_c$, $\mathrm{Im}\, q_\perp^\pm$ have opposite sign, so there is one mode. This is consistent with the results shown in figures 14 and 22. In the former figure, $r_1 > 0$, and there are acoustic zero modes on every surface. In the latter, $\boldsymbol{R}_T$ is chosen so that the coordinate system can always be rotated so that its direction corresponds to the $-x$ direction. Thus, in figure 14(a), the surface normal $\boldsymbol{G}$ and $\boldsymbol{R}_T$ are parallel, implying by the above considerations that $\theta = \pi$ and that there should be two acoustic zero surface modes. In (b), $\theta = 5\pi/6$, and there are also two zero acoustic modes whereas in (c), $\theta = 3\pi/3$, and there is only one acoustic mode. This is consistent with the above long-wavelength analysis if $\pi/6 < \theta_c < \pi/3$. Finally, for surfaces such as those with cells 1, 2, 3, and 7 in figure 14, $\theta = \pm\pi/2$ for systems with $\boldsymbol{R}_T$ in the $\pm x$ direction, and there should be one acoustic zero mode on each surface as is the case.

7. Review and future directions

In this review, we have presented a pedagogical introduction to Maxwell frames, in free versions of which $N_B = dN - d(d+1)/2$ and in the periodic versions of which $N_B = dN$, and to related frames on the verge of mechanical collapse. We made extensive use of the Index theorem [2], which relates the number of zero modes and SSSs of a frame to its site number N and bond number N_B, and of a relation between elastic energy and SSSs [47, 67] to frame our discussion of the elasticity and vibrational spectrum of these frames. We concentrated on Maxwell lattices, whose sites can be collected into unit cells whose origins lie on sites in a Bravais lattice, and we paid

particular attention to the surface zero-modes that necessarily arise when periodic Maxwell lattices are cut to create free surfaces.

All of the physical examples we studied were two-dimensional, both because important concepts are most easily explored in two rather than higher dimensions and because there is very little work of the type we discuss on higher dimensional systems. There is nonetheless, interesting work to be done on three-dimensional systems. The most obvious frames to investigate are variants of the pyrochlore lattice, a generalization of the two-dimensional kagome lattice composed of corner sharing tetrahedra arranged so that lines of bonds form straight filaments. Under periodic boundary conditions, this lattice is a Maxwell lattice with $N_B = 6N$. Preliminary work [82] indicates that this lattice can be distorted in much the same way as the kagome lattices to gap the spectrum and produce topologically distinct states with protected interfacial zero modes. Three-dimensional Maxwell lattices other than the simple cubic lattice include the many zeolite lattices, which like the pyrochlore lattice are based on corner sharing tetrahedra and which are in a sense $3D$ generalizations of the distorted kagome lattices like the twisted lattice of figure 3(d) or the more complex layered lattice of figure 16. These lattices all have a "flexibility window" that, like the twisted kagome lattice allow for easy change in volume [97]. It is likely that judicious rearrangements of lattice sites in these lattice will yield different topological states.

We considered here only linearized elasticity and vibrational structure. Maxwell frames obviously have interesting nonlinear properties, which in the end are responsible, for example, for the ability of the kagome lattice to undergo large area change upon twisting. References [98, 99] explored the nonlinear properties of the one-dimensional model [60] discussed in section 6.1 and found that under appropriate boundary conditions, the surface zero-modes become elevated to zero-energy nonlinear topological modes that propagate freely throughout the bulk. The system is a nonlinear mechanical conductor whose carriers are nonlinear solitary waves not captured by the linearized theory. An obvious question is whether similar behavior will be found in appropriately designed two- or three-dimensional frames.

As we have seen Maxwell lattices exhibit a surprisingly rich variety of vibrational responses. Ideal lattice-structures are generally the exception rather than the rule, and one can ask what effect do defects like dislocations have on the linear and nonlinear vibrational spectrum of Maxwell lattices. Reference [100] studied just this question in dislocated topological kagome lattices and found that zero modes can be localized at dislocations as a result of the interplay between between the topological dipole $\boldsymbol{R}_T$ of the lattice and the topological Burgers vector of the dislocations. Thus zero modes can be localized at a point by dislocations and along a a grain boundary separating two topologically distinct phases. Localized modes can also be created by enclosing a region of topological type B in a lattice of topological type A. There is certainly the potential for interesting and perhaps useful generalizations of these ideas.

Acknowledgments

to CLK, and by the Georgia Institute of Technology (AS).

Appendix A. States of self stress and the elastic energy

In this appendix, we present a derivation of (3.10). Our starting point is (2.17) for the stretch energy in terms of the N_B dimensional bond-elongation vector E, which we break up into an affine part $\mathsf{E}_{\mathrm{aff}}$ with components given by (3.8) and a part $\mathsf{CU} = \mathsf{Q}^T \mathsf{U}$ describing additional elongation that relaxes in response to the macroscopic strain imposed by $\mathsf{E}_{\mathrm{aff}}$. Multiplying Q^T on the left by the decomposition of the N_B-dimensional into the projection operators P_r^Q and P_s^Q, onto $\mathrm{OC}(\mathsf{Q})$ and $\ker(\mathsf{Q})$, respectively, and on the right by the decomposition of the dN-dimensional unit matrix into projections operators P_r^C and P_z^C onto $\mathrm{OC}(\mathsf{C})$ and $\ker(\mathsf{C})$, respectively, Q^T can be decomposed into $\mathsf{Q}^T = \mathsf{Q}_{rr}^T + \mathsf{Q}_{sr}^T + \mathsf{Q}_{rs}^T + \mathsf{Q}_{ss}^T$, where $\mathsf{Q}_{sr}^T = \mathsf{P}_s^Q \mathsf{Q}^T \mathsf{P}_r^C$, and so on. When Q^T multiplies any vector to its right, the components of that vector in $\ker(\mathsf{C})$ are annihilated, and only the components in $\mathrm{OC}(\mathsf{C})$ survive. Thus, $\mathsf{Q}^T \mathsf{U} = (\mathsf{Q}_{rr}^T + \mathsf{Q}_{sr}^T) \mathsf{U}_r$. When this quantity is multiplied on the left by any N_B-dimensional vector W, the term involving $\mathsf{Q}_{sr}^T \mathsf{U}_r$ vanishes because it is orthogonal to $\mathrm{OC}(\mathsf{Q})$ and it gives zero for any vector in $\ker(\mathsf{Q})$. Thus, in V_{el}, $\mathsf{Q}^T \mathsf{U}$ can be replaced by $\mathsf{Q}_{rr}^T \mathsf{U}_r$. Similarly, $\mathsf{U}^T \mathsf{Q}$ can be replaced by $\mathsf{U}_r^T \mathsf{Q}_{rr}$, and the elastic energy as a function of U and $\mathsf{E}_{\mathrm{aff}}$ is

$$V f_{\mathrm{el}} = \tfrac{1}{2}(\mathsf{E}_{\mathrm{aff}}^T + \mathsf{U}_r^T \mathsf{Q}_{rr}) \mathsf{k} (\mathsf{E}_{\mathrm{aff}} + \mathsf{Q}_{rr}^T \mathsf{U}_r). \tag{A.1}$$

Minimizing over the $dN - N_0$ independent components of U_r (or U_r^T) yields

$$V \frac{\partial f_{\mathrm{el}}}{\partial \mathsf{U}_r^T} = \mathsf{Q}_{rr} \mathsf{k} (\mathsf{E}_{\mathrm{aff}} + \mathsf{Q}_{rr}^T \mathsf{U}_r) = 0 \tag{A.2}$$

or, because both Q_{rr} and k_{rr} are invertible,

$$\mathsf{E}_{\mathrm{aff},r} + \mathsf{Q}_{rr}^T \mathsf{U}_r = -(\mathsf{k}_{rr})^{-1} \mathsf{k}_{rs} \mathsf{E}_{\mathrm{aff},s} \tag{A.3}$$

and

$$V f_{\mathrm{el}} = \tfrac{1}{2} \mathsf{E}_{\mathrm{aff},s}^T (\mathsf{k}_{ss} - \mathsf{k}_{sr}(\mathsf{k}_{rr})^{-1} \mathsf{k}_{rs}) \mathsf{E}_{\mathrm{aff},s} = \tfrac{1}{2} \mathsf{E}_{\mathrm{aff},s}^T [(\mathsf{k}^{-1})_{ss}]^{-1} \mathsf{E}_{\mathrm{aff},s}, \tag{A.4}$$

where $(\mathsf{k}^{-1})_{ss}$ is the projection of k^{-1} onto the null space of Q. This is (3.10). The final relation can be derived as follows: Let p the inverse of k and decompose the two matrices into their projections onto the range and nullspace of Q,

$$\mathsf{k} = \begin{pmatrix} \mathsf{k}_{ss} & \mathsf{k}_{sr} \\ \mathsf{k}_{rs} & \mathsf{k}_{rr} \end{pmatrix} \qquad \mathsf{p} = \begin{pmatrix} \mathsf{p}_{ss} & \mathsf{p}_{sr} \\ \mathsf{p}_{rs} & \mathsf{p}_{rr\cdot} \end{pmatrix} \tag{A.5}$$

Then $\mathsf{k}\,\mathsf{p} = \mathsf{I}$ implies that $\mathsf{k}_{ss}\mathsf{p}_{ss} + \mathsf{k}_{sr}\mathsf{p}_{rs} = \mathsf{I}_{ss}$ and $\mathsf{k}_{rs}\mathsf{p}_{ss} + \mathsf{k}_{rr}\mathsf{p}_{rs} = 0$. Thus, $\mathsf{k}_{ss} + \mathsf{k}_{sr}\mathsf{p}_{rs}\mathsf{p}_{ss}^{-1} = \mathsf{p}_{ss}^{-1}$ and $\mathsf{k}_{rs} = -\mathsf{k}_{rr}\mathsf{p}_{rs}\mathsf{p}_{ss}^{-1}$, and finally $\mathsf{k}_{ss} - \mathsf{k}_{sr}\mathsf{k}_{rr}^{-1}\mathsf{k}_{rs} = \mathsf{p}_{ss}^{-1} = [(\mathsf{k}^{-1})_{ss}]^{-1}$ as required.

Appendix B. Zeroes of $\det \mathsf{K}(\boldsymbol{q})$ and Guest Modes.

In this appendix we derive (4.14) relating the determinant of the long-wavelength dynamical matrix and the eigenvectors of the elastic Guest mode. We begin by

representing ε_{ij} as $\frac{1}{2}(q_i u_j + q_j u_i)$. The the strain vector becomes

$$\boldsymbol{\varepsilon}_V = \begin{pmatrix} iq_x u_x \\ iq_y u_y \\ \frac{i}{2}(q_x u_y + q_y u_x) \end{pmatrix} \equiv i \begin{pmatrix} q_x & 0 \\ 0 & q_y \\ \frac{1}{2}q_y & \frac{1}{2}q_x \end{pmatrix} \begin{pmatrix} u_x \\ u_y \end{pmatrix} \equiv \mathsf{S}_{ai} u_i, \qquad (B.1)$$

where the summation convention is understood, $a = 1, 2, 3$, and $i = x, y$. The elastic energy density for a fixed $\boldsymbol{q}$ is thus

$$f_{\mathrm{el}} = \tfrac{1}{2} u_i \mathsf{S}_{ia}^T \mathbb{K}_{ab} \mathsf{S}_{bj} u_j = \tfrac{1}{2} u_i(-\boldsymbol{q}) \mathsf{K}_{ij}(\boldsymbol{q}) u_j(\boldsymbol{q}), \qquad (B.2)$$

where $\mathsf{K}_{ij} = \mathsf{S}_{ia}^T K_{ab} \mathsf{S}_{bj}$. Then using (4.13),

$$\mathsf{K}_{ij} = \mathsf{S}_{ia}^T \left(\sum_{p=1,2} K_p v_{pa} v_{pb} \right) \mathsf{S}_{bj} \equiv \sum_{p=1,2} K_p \tilde{\mathsf{S}}_{pi} \tilde{\mathsf{S}}_{pj}, \qquad (B.3)$$

where $\tilde{\mathsf{S}}_{pj} = v_{pb} \mathsf{S}_{bj}$, or

$$\tilde{\mathsf{S}}_{11} = \boldsymbol{v}_1 \cdot (q_x, 0, \tfrac{1}{2}q_y) = q_x v_{11} + \tfrac{1}{2} q_y v_{13}$$
$$\tilde{\mathsf{S}}_{22} = \boldsymbol{v}_2 \cdot (0, q_y, \tfrac{1}{2}q_x) = q_y v_{22} + \tfrac{1}{2} q_x v_{23}$$
$$\tilde{\mathsf{S}}_{12} = \boldsymbol{v}_1 \cdot (0, q_y, \tfrac{1}{2}q_x) = q_y v_{12} + \tfrac{1}{2} q_x v_{13}$$
$$\tilde{\mathsf{S}}_{21} = \boldsymbol{v}_2 \cdot (q_x, 0, \tfrac{1}{2}q_y) = q_x v_{21} + \tfrac{1}{2} q_y v_{23}. \qquad (B.4)$$

Thus,

$$\mathsf{K}_{ij} = \begin{pmatrix} K_1 \tilde{\mathsf{S}}_{11}^2 + K_2 \tilde{\mathsf{S}}_{21}^2 & K_1 \tilde{\mathsf{S}}_{11} \tilde{\mathsf{S}}_{12} + K_2 \tilde{\mathsf{S}}_{21} \tilde{\mathsf{S}}_{22} \\ K_1 \tilde{\mathsf{S}}_{12} \tilde{\mathsf{S}}_{11} + K_2 \tilde{\mathsf{S}}_{21} \tilde{\mathsf{S}}_{22} & K_1 \tilde{\mathsf{S}}_{12}^2 + K_2 \tilde{\mathsf{S}}_{22}^2 \end{pmatrix} \qquad (B.5)$$

and

$$\begin{aligned} \det \mathsf{K} &= (K_1 \tilde{\mathsf{S}}_{11}^2 + K_2 \tilde{\mathsf{S}}_{21}^2)(K_1 \tilde{\mathsf{S}}_{12}^2 + K_2 \tilde{\mathsf{S}}_{22}^2) - (K_1 \tilde{\mathsf{S}}_{11} \tilde{\mathsf{S}}_{12} + K_2 \tilde{\mathsf{S}}_{21} \tilde{\mathsf{S}}_{22})^2 \\ &= K_1 K_2 (\tilde{\mathsf{S}}_{11} \tilde{\mathsf{S}}_{22} - \tilde{\mathsf{S}}_{12} \tilde{\mathsf{S}}_{21})^2 \\ &\equiv K_1 K_2 (\det \tilde{\mathsf{S}})^2, \end{aligned} \qquad (B.6)$$

where

$$\det \tilde{\mathsf{S}} = \mathsf{S}_{1i} \mathsf{S}_{2j}(v_{1i} v_{2j} - v_{2i} v_{1j}). \qquad (B.7)$$

The three-component vectors $\boldsymbol{v}_1$, $\boldsymbol{v}_2$, and $\boldsymbol{v}_0$ form an orthonormal triad such that $(v_{1i} v_{2j} - v_{2i} v_{1j}) = \epsilon_{ijk} v_{0k}$, where ϵ_{ijk} is the anti-symmetric Levi-Civita symbol, and

$$\det \tilde{\mathsf{S}} = \mathsf{S}_{1i} \mathsf{S}_{2j} \epsilon_{ijk} v_{0k} = -\frac{1}{2}(v_{02} q_x^2 - 2 v_{03} q_x q_y + v_{01} q_y^2). \qquad (B.8)$$

Using this equation and (B.6) yields (4.14).

Appendix C. Compatibility matrix for kagome lattices

The kagome lattice has a central role in this review. Here we derive and display the $\boldsymbol{q}$-dependent compatibility matrix for a general lattice for the symmetric unit cell of figure 10(c), which identifies and labels the three sites and six bonds in the cell. The labeling of the sites and bonds does not change when the cell is distorted to produce the twisted kagome of topological lattices. The equations relating the six

bond elongations in the unit cell to sites displacements in that and nearest neighbor cells are

$$e_1 = (\boldsymbol{u}_1(\boldsymbol{R}) - \boldsymbol{u}_3(\boldsymbol{R})) \cdot \hat{\boldsymbol{b}}_1 \qquad\qquad e_2 = (\boldsymbol{u}_2(\boldsymbol{R}) - \boldsymbol{u}_1(\boldsymbol{R})) \cdot \hat{\boldsymbol{b}}_2$$

$$e_3 = (\boldsymbol{u}_3(\boldsymbol{R}) - \boldsymbol{u}_2(\boldsymbol{R})) \cdot \hat{\boldsymbol{b}}_3 \qquad\qquad e_4 = (\boldsymbol{u}_3(\boldsymbol{R} + \boldsymbol{a}_1) - \boldsymbol{u}_1(\boldsymbol{R})) \cdot \hat{\boldsymbol{b}}_4$$

$$e_5 = (\boldsymbol{u}_1(\boldsymbol{R} + \boldsymbol{a}_2) - \boldsymbol{u}_2(\boldsymbol{R})) \cdot \hat{\boldsymbol{b}}_5 \qquad e_6 = (\boldsymbol{u}_2(\boldsymbol{R} + \boldsymbol{a}_3) - \boldsymbol{u}_3(\boldsymbol{R})) \cdot \hat{\boldsymbol{b}}_6, \quad \text{(C.1)}$$

where $\boldsymbol{R}$ is the position of the unit cell, and $\boldsymbol{a}_i$ are the lattice vectors shown in figure 10(c) and the resultant compatibility matrix (in a gauge in which the site and bond basis vectors $\boldsymbol{r}_\mu$ and $\boldsymbol{r}_\beta$ are set to zero) is

$$\boldsymbol{C}_{\text{sym}}(\boldsymbol{q}) = \begin{pmatrix} \hat{b}_{1x} & \hat{b}_{1y} & 0 & 0 & -\hat{b}_{1x} & -\hat{b}_{1y} \\ -\hat{b}_{2x} & -\hat{b}_{2y} & \hat{b}_{2x} & \hat{b}_{2y} & 0 & 0 \\ 0 & 0 & -\hat{b}_{3x} & -\hat{b}_{3y} & \hat{b}_{3x} & \hat{b}_{3y} \\ -\hat{b}_{4x} & -\hat{b}_{4y} & 0 & 0 & e^{i\boldsymbol{q}\cdot\boldsymbol{a}_1}\hat{b}_{4x} & e^{i\boldsymbol{q}\cdot\boldsymbol{a}_1}\hat{b}_{4y} \\ e^{i\boldsymbol{q}\cdot\boldsymbol{a}_2}\hat{b}_{5x} & e^{i\boldsymbol{q}\cdot\boldsymbol{a}_2}\hat{b}_{5y} & -\hat{b}_{5x} & -\hat{b}_{5y} & 0 & 0 \\ 0 & 0 & e^{i\boldsymbol{q}\cdot\boldsymbol{a}_3}\hat{b}_{6x} & e^{i\boldsymbol{q}\cdot\boldsymbol{a}_3}\hat{b}_{6y} & -\hat{b}_{6x} & -\hat{b}_{6y} \end{pmatrix} \quad \text{(C.2)}$$

Appendix D. Gauge choice and surface zero modes

This appendix presents details about properties of $\det \mathbf{C}$ in different choices of the unit cell (different gauges) and how switching from the symmetric unit cell (i.e., those shown in figure 10) to ones that match surface boundaries changes the topological index as measured by (6.10) with $\mathbf{Q}$ replaced by $\mathbf{C}$ to the total count (local plus topological) of the number of surface zero modes.

We begin with the observation that $\det \mathbf{C}_{\text{Sym}}$ is the compatibility matrix in the symmetric gauge [(C.2)] of the kagome lattice scan be expressed in terms of four parameters $g_0, ..., g_3$ (each a function of the unit vectors $\hat{\boldsymbol{b}}_\beta$) as

$$\det \mathbf{C}_{\text{Sym}} = g_1 S_2 S_3 + g_2 S_3 S_1 + g_3 S_1 S_2 + g_0 S_1 S_2 S_3, \qquad \text{(D.1)}$$

where $S_n = w_n - 1$ with $w_n = e^{i\boldsymbol{q}\cdot\boldsymbol{a}_n}$. Note that there is no constant term or terms linear in w_n. This is a reflection of the fact that the translation invariance requires the stiffness matrix $\mathbf{K} = k\mathbf{C}^T\mathbf{C}$ (4.10) have two eigenvalues that vanish as q in the long-wavelength $q \to 0$ limit and thus that $\det \mathbf{K}$ vanish as q^4, or equivalently that $\det \mathbf{C}$ (for any gauge) vanish as q^2. With the help of the identity $w_1 w_2 w_3 = 1$, (D.1) expressed in terms of the w_ns becomes

$$\det \mathbf{C}_{\text{Sym}} = a + \sum_{n=1}^{3} b_n w_n + \sum_{n=1}^{3} c_n w_n^{-1}, \qquad \text{(D.2)}$$

where $a = g_1 + g_2 + g_3$, $b_n = g_0 + g_n - a$, and $c_n = g_n - g_0$, or setting $w_1 = z_x$, $w_2 = z_x^{-1/2} z_y$, and $w_3 = z_x^{-1/2} z_y^{-1}$, where $z_x = e^{iq_x}$ and $z_y = e^{i\sqrt{3}q_y/2}$,

$$\det \mathbf{C}_{\text{Sym}} = (a + b_1 z_x + c_1 z_x^{-1}) + (b_2 z_x^{-1/2} + c_3 z_x^{1/2})z_y + (b_3 z_x^{-1/2} + c_3 z_x^{1/2})z_y^{-1}. \quad \text{(D.3)}$$

This equation can be used without further modification to study the topological number associated with $\det \mathbf{C}_{\text{Sym}}$ for $\boldsymbol{q}$-vectors an paths between equivalent points in the BZ parallel to the x and y axes.

The Cauchy argument principle provides a relative count of the number of zeros and poles of any meromorphic function $F(z)$ of a complex number z in the interior of a contour $\mathcal{C}$:

$$\frac{1}{2\pi i}\oint_{\mathcal{C}}\frac{F'(z)}{F(z)}dz = \frac{1}{2\pi i}\oint_{\mathcal{C}}\frac{d\ln F(z)}{dz}dz = n - p, \tag{D.4}$$

where n is the number of zeros and p the number of poles counted with their order (e.g., if $F(z) = z^{-2}$, $p = 2$) in the region bounded by $\mathcal{C}$. If the contour $\mathcal{C}$ is the unit circle, the magnitude of z at any zero of $F(z)$ is less than unity. Thus, the argument principle applied to $\det \mathbf{C}$ with $\mathcal{C}$ the unit circle will count the number of zeros with $|z| < 1$, and thus the number of decaying surface modes, minus the number of poles.

Consider first the case for $\boldsymbol{q}$ along the y-direction (i.e. perpendicular to a surface parallel to the x-axis). z_y remains unchanged under the transformation $q_y \to q_y + 4\pi/\sqrt{3}a$ or equivalently under $\boldsymbol{q} \to \boldsymbol{q} + \boldsymbol{G}_1$, where $\boldsymbol{G}_1$ is defined in figure 10, reflecting the fact that the width of the symmetric unit cell along y is $a\sqrt{3}/2$. $\det \mathbf{C}_{\mathrm{Sym}}$ is equal to z_y^{-1} times a quadratic polynomial in z_y and therefore has one pole and either $n = 0, 1,$ or 2 zeros. Thus by the argument principle,

$$\frac{1}{2\pi i}\oint \frac{d}{dz_y}\ln\det\mathbf{C}_{\mathrm{Sym}} = n - 1 \equiv m_y, \tag{D.5}$$

where $m_y = -1, 0, 1$. In the non-topological lattices, $m_y = 0$ indicating that as a function of q_y there is one zero in $\det\mathbf{C}_{\mathrm{Sym}}(z_y)$ within the unit circle. In the topological lattice shown in figure 21 (c), $\boldsymbol{R}_T = -\boldsymbol{a}_1$, and $m_y = 1$ (for the configuration shown in figure 21(b)) indicating two zeros in $\det\mathbf{C}_{\mathrm{Sym}}$ within the unit circle. Direct evaluation of the the integral in (D.5) confirms this result.

For $\boldsymbol{q}$ parallel to x [perpendicular to surface parallel to y-axis as in figure 22(a) or (c)], $\det\mathbf{C}_{\mathrm{Sym}}$ is a function of $z \equiv z_x^{1/2}$ and is equal to z^{-2} times a fourth order polynomial in z, and it has two poles and four zeros in z. The topological integral of $\ln\det\mathbf{C}_{\mathrm{Sym}}$ around the unit circle in z (i.e., for q_x from 0 to 4π) can, therefore, take on values of $m_x = -2, -1, ..., 2$. For the non-topological lattice, $m_x = 0$ for all orientation of $\boldsymbol{R}_T$ relative to the x-axis, indicating two zeros within the unit circle. For the topological lattices, $m_x = 2$ and $m_x = 1$, respectively, for configuration figure 22 (a) with $\boldsymbol{R}_T = -\boldsymbol{a}_1$ and configuration figure 22(a) with $\boldsymbol{R}_T = \boldsymbol{a}_3$.

Transformations from the symmetric unit cell to cells compatible with specific surfaces constitute gauge transformations in which the phase of $\det\mathbf{C}$ changes by a factor of the local polarization charge of (6.12), $-\boldsymbol{q}\cdot\boldsymbol{R}_L = -d\sum\tilde{\boldsymbol{r}}_\mu + \sum_\beta\tilde{\boldsymbol{r}}_\beta$:

$$\det\mathbf{C}_{\mathrm{Sur}} = e^{-i\boldsymbol{q}\cdot\boldsymbol{R}_L}\det\mathbf{C}_{\mathrm{Sym}}. \tag{D.6}$$

The phase factor can be determined directly from (C.1) relating bond stretches to site displacements. For example, the left-hand (LH) surface cell of figure 22(d) requires the displacement of site 1 through $\boldsymbol{a}_2$ and bonds 4 and 6 through $\boldsymbol{a}_2$ and $-\boldsymbol{a}_3$, respectively. A bond translation through a lattice vector $\boldsymbol{a}$ changes the arguments of the displacements of sites at the both ends of the translated bond by $\boldsymbol{a}$. For example, a displacement of bond 4 through $\boldsymbol{a}_2$ with no site displacement would change the equation for the stretch of bond 4 from that in (C.1) to $e_4 = (\boldsymbol{u}_3(\boldsymbol{R} + \boldsymbol{a}_1 + \boldsymbol{a}_2) - \boldsymbol{u}_1(\boldsymbol{R} + \boldsymbol{a}_2)) \cdot \hat{\boldsymbol{b}}_4$. On the other hand, a translation of a site requires the change in the arguments of the displacement of all occurrences of that site by the negative of the translation. Thus the equation for bond 4, which includes

a displacement of site 1 whose argument must be augmented by the negative of that displacement, i.e., by $-\boldsymbol{a}_2$ in the case of the LH surface cell of figure 22(d), becomes $e_4 = (\boldsymbol{u}_3(\boldsymbol{R} + \boldsymbol{a}_1) - \boldsymbol{u}_1(\boldsymbol{R})) \cdot \hat{\boldsymbol{b}}_4 \cdot$ as can be verified by calculating the expression for e_4 direction from the surface cell.

Thus for the LH cell of figure 22(d), $\boldsymbol{R}_L = -\boldsymbol{a}_1$, and $e^{-i\boldsymbol{q}\cdot\boldsymbol{R}_L} = e^{iq_x} = z^2$, and $\det \mathbf{C}_{\mathrm{Sur}} = z^2 \det \mathbf{C}_{\mathrm{Sym}}$ is simply a fourth-order polynomial in $z = e^{iq_x/2}$. The two poles in $\det \mathbf{C}_{\mathrm{Sym}}$ have been removed, and the topological integral around the unit circle of z counts only the zeros of $\det \mathbf{C}_{\mathrm{Sym}}$ within the unit circle, four in the case of figure 22(a) and three in the case of figure 21(c).

The right-hand (RH) surface cell of figure 22(d), on the other hand, requires only the translation of bond 6 through $-\boldsymbol{a}_3$, and $\det \mathbf{C}_{\mathrm{Sur}} = z_x z_y \det \mathbf{C}_{\mathrm{Sym}}$, which has no poles in z_y, is simply a quadratic polynomial in z_y. Again, the topological integral around the unit circle of z_y counts only zeros of $\det \mathbf{C}_{\mathrm{Sur}}$.

It is clear that $\mathbf{C}_{\mathrm{Sur}}$ for a given surface is identical with $e^{i\boldsymbol{q}\cdot\boldsymbol{G}_s}$ replaced by λ, where $\boldsymbol{G}$ is the reciprocal lattice vector associated that surface, is identical to $\mathbf{C}_{\mathrm{Sur}}$ calculate from the surface cells directly as discussed in section 5.3.2, (5.15) to (5.17). The latter equations are set up from the beginning so that there are no negative powers of λ in $\mathbf{C}_{\mathrm{Sur}}$, so the integral around the unit circle of $\det \mathbf{C}_{\mathrm{Sur}}$ give the count of the number of zero modes of that surface.

[1] J. C. Maxwell. On the calculation of the equilibrium and stiffness of frames. *Philos. Mag.*, 27:294, 1864.

[2] C. R. Calladine. Buckminster Fuller "tensegrity" structures and Clerk Maxwell rules for the construction of stiff frames. *Int. J. Solids Struct.*, 14(2):161–172, 1978.

[3] Jacques Heyman. *The Science of Structural Engineering*. Cengage Learning, Stamford CT, 2005.

[4] Aslam Kassimali. *Structural Analysis*. Cengage Learning, Stamford CT, 2005.

[5] J. C. Phillips. Topology of covalent non-crystalline solids 2: medium-range order in chalcogenide alloys and α-Si(Ge). *J. Non-Cryst. Solids*, 43(1):37–77, 1981.

[6] M. F. Thorpe. Continuous deformations in random networks. *J. Non-Cryst. Solids*, 57(3):355 – 370, 1983.

[7] J. C. Phillips and M. F. Thorpe. Constraint theory, vector percolation and glass formation. *Solid State Commun.*, 53:699 – 702, 1985.

[8] M. F. Thorpe, D. J. Jacobs, M. V. Chubynsky, and J. C. Phillips. Self-organization in network glasses. *J. Non-Cryst. Solids*, 266:859–866, 2000.

[9] P. Boolchand, G. Lucovsky, J. C. Phillips, and M. F. Thorpe. Self-organization and the physics of glassy networks. *Philo. Mag.*, 85(32):3823–3838, 2005.

[10] Shechao Feng and Pabitra N. Sen. Percolation on elastic networks: New exponent and threshold. *Phys. Rev. Lett.*, 52:216–219, 1984.

[11] D. J. Jacobs and M. F. Thorpe. Generic rigidity percolation: The pebble game. *Phys. Rev. Lett.*, 75:4051–4054, 1995.

[12] D. J. Jacobs and M. F. Thorpe. Generic rigidity percolation in two dimensions. *Phys. Rev. E*, 53(4):3682–3693, 1996.

[13] E. Guyon, S. Roux, A. Hansen, D. Bideau, J. P. Troadec, and H. Crapo. Non-local and non-linear problems in the mechanics of disordered systems - application of granular media and rigidity problems. *Rep. Prog. Phys.*, 53(4):373–419, 1990.

[14] M. V. Chubynsky and M. F. Thorpe. Algorithms for three-dimensional rigidity analysis and a first-order percolation transition. *Phys. Rev. E*, 76(4), 2007.

[15] Kenton D. Hammonds, Martin T. Dove, Andrew P. Giddy, Volker Heine, and Bjoern Winkler. Rigid-unit phonon modes and structural phase transitions in framework silicates. *American Mineralogist*, 81(9-10):1057–1079, 1996.

[16] A. J. Liu and S. R. Nagel. Jamming is not just cool any more. *Nature*, 396:21, 1998.

[17] M. Wyart. On the rigidity of amorphous solids. *Ann. Phys. Fr*, 30(3):1–96, 2005.

[18] M. Wyart, S. R. Nagel, and T. A. Witten. Geometric origin of excess low-frequency vibrational modes in weakly connected amorphous solids. *Europhys. Lett.*, 72(3):486–492, 2005.

[19] M. van Hecke. Jamming of soft particles: geometry, mechanics, scaling and isostaticity. *J. Phys: Condens. Matter*, 22(3):033101, 2010.

[20] A. J. Liu and S. R. Nagel. *The Jamming Transition and the Marginally Jammed Solid*, volume 1 of *Ann. Rev. Condens. Matter Phys.*, pages 347–369. 2010.

[21] C. P. Broedersz and F. C. MacKintosh. Modeling semiflexible polymer networks. *Rev. Mod. Phys. 86, 995*, 86, 2014.

[22] David A. Head, Alex J. Levine, and F. C. MacKintosh. Deformation of cross-linked semiflexible polymer networks. *Phys. Rev. Lett.*, 91(10):108102, 2003.

[23] Jan Wilhelm and Erwin Frey. Elasticity of stiff polymer networks. *Phys. Rev. Lett.*, 91(10):108103, 2003.

[24] Claus Heussinger and Erwin Frey. Floppy modes and nonaffine deformations in random fiber networks. *Phys. Rev. Lett.*, 97(10):105501, 2006.

[25] C. Heussinger, B. Schaefer, and E. Frey. Nonaffine rubber elasticity for stiff polymer networks. *Phys. Rev. E*, 76(3):031906, 2007.

[26] E. M. Huisman and T. C. Lubensky. Internal stresses, normal modes, and nonaffinity in three-dimensional biopolymer networks. *Phys. Rev. Lett.*, 106(8):088301, 2011.

[27] C. P. Broedersz, X. Mao, T. C. Lubensky, and F. C. MacKintosh. Criticality and isostaticity in fibre networks. *Nat. Phys.*, 7:983–988, 2011.

[28] X. Mao, O. Stenull, and T. C. Lubensky. Elasticity of a filamentous kagome lattice. *Phys. Rev. E*, 87:042602, 2013.

[29] S. A. Wells, S. Menor, B. Hespenheide, and M. F. Thorpe. Constrained geometric simulation of diffusive motion in proteins. *Phys. Biol.*, 2(4):S127–S136, 2005.

[30] Dietrich Stauffer and Amnon Aharony. *Introduction to Percolation Theory*. Taylor and Francis, London, 2nd edition edition, 1994.

[31] S. Kirkpatrick. Percolation and conduction. *Rev. Mod. Phys.*, 45(4):574–588, 1973.

[32] S. A. O'Hern, C. S.and Langer, A. J. Liu, and S. R. Nagel. Random packings of frictionless

particles. *Phys. Rev. Lett.*, 88(7):075507, 2002.

[33] C. S. O'Hern, L. E. Silbert, A. J. Liu, and S. R. Nagel. Jamming at zero temperature and zero applied stress: The epitome of disorder. *Phys. Rev. E*, 68:011306, 2003.

[34] C. P. Goodrich, A. J. Liu, and S. R. Nagel. Finite-size scaling at the jamming transition. *Phys. Rev. Lett.*, 109(9):095704, 2012.

[35] C. P. Goodrich, Simon Dagois-Bohy, Brian P. Tighe, Martin van Hecke, A. J. Liu, and Sidney R. Nagel. Jamming in finite systems: stability, anisotropy, fluctuations and scaling. *Phys. Rev. E*, 90:0222138, 2014.

[36] D. J. Durian. Foam mechanics at the bubble scale. *Phys. Rev. Lett.*, 75(26):4780–4783, 1995.

[37] L. E. Silbert, A. J. Liu, and S. R. Nagel. Vibrations and diverging length scales near the unjamming transition. *Phys. Rev. Lett.*, 95(9):098301, 2005.

[38] M. Wyart, L. E. Silbert, S. R. Nagel, and T. A. Witten. Effects of compression on the vibrational modes of marginally jammed solids. *Phys. Rev. E*, 72:051306, 2005.

[39] C. P. Goodrich, W. G. Ellenbroek, and A. J. Liu. Stability of jammed packings I: the rigidity length scale. *Soft Matter*, 9(46):10993–10999, 2013.

[40] S. S. Schoenholz, C. P. Goodrich, O. Kogan, A. J. Liu, and S. R. Nagel. Stability of jammed packings II: the transverse length scale. *Soft Matter*, 9(46):11000–11006, 2013.

[41] N. Xu, V. Vitelli, M. Wyart, A. J. Liu, and S. R. Nagel. Energy transport in jammed sphere packings. *Phys. Rev. Lett.*, 102(3):038001, 2009.

[42] N. Xu, V. Vitelli, A. J. Liu, and S. R. Nagel. Anharmonic and quasi-localized vibrations in jammed solids-modes for mechanical failure. *EPL*, 90(5):56001, 2010.

[43] E. Lerner, G. During, and M. Wyart. A unified framework for non-brownian suspension flows and soft amorphous solids. *PNAS*, 109(13):4798–4803, 2012.

[44] G. During, E. Lerner, and M. Wyart. Phonon gap and localization lengths in floppy materials. *Soft Matter*, 9(1):146–154, 2013.

[45] Anton Souslov, A. J. Liu, and T. C. Lubensky. Elasticity and response in nearly isostatic periodic lattices. *Phys. Rev. Lett.*, 103(20):205503, 2009.

[46] Xiaoming Mao, Ning Xu, and T. C. Lubensky. Soft modes and elasticity of nearly isostatic lattices: Randomness and dissipation. *Phys. Rev. Lett.*, 104(8):085504, 2010.

[47] S. Pellegrino. Structural computatons with the singular-value decomposition of the equilibrium matrix. *Int. J. Solids Struct.s*, 30(21):3025–3035, 1993.

[48] S. Pellegrino and C. R. Calladine. Matrix analysis of statically and kinetmatically indeterminate frameworks. *Int. J. of Solids Struct.*, 22(4):409–428, 1986.

[49] S. D. Guest and J. W. Hutchinson. On the determinacy of repetitive structures. *J. Mech. Phys. Solids*, 51(3):383–391, 2003.

[50] B. I. Halperin. Quantized Hall Conductance, Current-Carrying Edge States, and the Existence of Extended States in a Two-Dimensional Disordered Potential. *Phys. Rev. B*, 25(4):2185–2190, 1982.

[51] F. D. M. Haldane. Model for a Quantum Hall Effect Without Landau Levels - Condensed Matter Realization of the Parity Anomaly. *Phys. Rev. Lett.*, 61(18):2015–2018, OCT 31 1988.

[52] W. P. Su, J. R. Schrieffer, and A. J. Heeger. Solitons in polyacetalene. *Phys. Rev. Lett.*, 42:1698, 1979.

[53] C. L. Kane and E. J. Mele. Z(2) topological order and the quantum spin Hall effect. *Phys. Rev. Lett.*, 95(14):146802, 2005.

[54] B. Andrei Bernevig, Taylor L. Hughes, and Shou-Cheng Zhang. Quantum spin Hall effect and topological phase transition in HgTe quantum wells. *Science*, 314(5806):1757–1761, 2006.

[55] J. E. Moore and L. Balents. Topological invariants of time-reversal-invariant band structures. *Phys. Rev. B*, 75:121306, 2007.

[56] Liang Fu, C. L. Kane, and E. J. Mele. Topological Insulators in Three Dimensions. *Phys. Rev. Lett.*, 98:106803, 2007.

[57] Z. Hasan and C.L. Kane. Colloquium: Topological insulators. *Rev. Mod. Phys.*, 82:3045, 2010.

[58] Xiao-Liang Qi and Shou-Cheng Zhang. Topological insulators and superconductors. *Rev. Mod. Phys.*, 83(4):1057–1110, 2011.

[59] L. D. Landau and E. M. Lifshitz. *Elasticity Theory*. Pergamon Press, 1986.

[60] CL Kane and T. C. Lubensky. Topological boundary modes in isostatic lattices. *Nature Phys.*, 10(1):39–45, 2014.

[61] Michael F. Atiyah and Singer Isadore M. The index of elliptic operators on compact manifolds. *Bull. Amer. Math. Soc.*, 69(3):322–433, 1963.

[62] N. Nakamura. *Geometry, Topology and Physics*. Institute of Physics Publishing, Bristol, 2nd edition, 2008. p. 79 and chapter 12.

[63] Garret Birkhoff and Saunders MacLane. *A Survey of Modern Algebra*. Taylor and Francis (A K Peters/CRC Press), New York, 1998.

[64] L. Yan, G. During, and M. Wyart. Why glass elasticity affects the thermodynamics and fragility of supercooled liquids. *PNAS*, 110(16):6307–6312, 2013.

[65] Charles Kittel. *Introduction to Solid State Physics*. John Wiley and Sons, New York, fourth edition, 1971.

[66] Niel W. Ashcroft and N. David Mermin. *Solid State Physics*. Cenage Learning, New York, first edition, 1976.

[67] C.P. Goodrich. unpublished private communication. 2014.

[68] S. Dagois-Bohy, B. P. Tighe, J. Simon, S. Henkes, and M. van Hecke. Soft-sphere packings at finite pressure but unstable to shear. *Phys. Rev. Lett.*, 109(9):095703, 2012.

[69] T. C. Stenull, OlafLubensky. Penrose tilings as jammed solids. *Phys. Rev. Lett.*, 113(15):158301, 2014.

[70] M. Falk, B. Chen, T. C. Lubensky, D. Zeb Rocklin, and V. Vitelli. Topological phonon states in deformed square lattices. *unpublished*, 2015.

[71] Vivek Aji. Adler-bell-jackiw anomaly in weyl semimetals: Application to pyrochlore iridates. *Phys. Rev. B*, 85, 2012.

[72] Huazhou Wei, Sung-Po Chao, and Vivek Aji. Excitonic phases from weyl semimetals. *Phys. Rev. Lett.*, 109(19):196403, 2012.

[73] Peng Wei, Zhiyong Wang, Xinfei Liu, Vivek Aji, and Jing Shi. Field-effect mobility enhanced by tuning the fermi level into the band gap of Bi_2Se_3. *Phys. Rev. B*, 85(20):201402, 2012.

[74] Vivek Aji, Yan He, and C. M. Varma. Magnetochiral kerr effect with application to the cuprates. *Phys. Rev. B*, 87(17):174518, 2013.

[75] Lijun Zhu, Vivek Aji, and Chandra M. Varma. Ordered loop current states in bilayer graphene. *Phys. Rev. B*, 87(3):035427, 2013.

[76] Michael Phillips and Vivek Aji. Tunable line node semimetals. *Phys. Rev. B*, 90(11):115111, 2014.

[77] Evan Sosenko, Huazhou Wei, and Vivek Aji. Effect of contacts on spin lifetime measurements in graphene. *Phys. Rev. B*, 89(24):245436, 2014.

[78] Huazhou Wei, Sung-Po Chao, and Vivek Aji. Long-range interaction induced phases in weyl semimetals. *Phys. Rev. B*, 89(23):235109, 2014.

[79] Ling Lu, John D. Joannopoulos, and Marin Soljacic. Waveguiding at the edge of a three-dimensional photonic crystal. *Phys. Rev. Lett.*, 108(24):243901, 2012.

[80] Ling Lu, Liang Fu, John D. Joannopoulos, and Marin Soljacic. Weyl points and line nodes in gyroid photonic crystals. *Nature Photonics*, 7(4):294–299, 2013.

[81] Ling Lu, John D. Joannopoulos, and Marin Soljaclc. Topological photonics. *Nature Photonics*, 8(11):821–829, 2014.

[82] Olaf Stenull, C. L. Kane, and T. C. Lubensky. unpublished. 2015.

[83] Kai Sun, Anton Souslov, Xiaoming Mao, and T. C. Lubensky. Surface phonons, elastic response, and conformal invariance in twisted kagome lattices. *PNAS*, 109(31):12369–12374, 2012.

[84] R. G. Hutchinson and N. A. Fleck. The structural performance of the periodic truss. *J. Mech. Phys. Solids*, 54(4):756–782, 2006.

[85] H. Mitschke, G. E. Schr"oder-Turk, K. Mecke, P. W. Fowler, and S. D. Guest. The structural performance of the periodic truss. *EPL*, 102:66005, 2013.

[86] R. Lakes. Foam structures with a negative poisson's ratio. *Science*, 235(4792):1038–1040, 1987.

[87] L. Susskind. The world as a hologram. *J. Math Phys.*, 36:6377–6396, 1995.

[88] Anton Souslov unpublished thesis, Universtiy of Pennsylvania, 2011. 2014.

[89] C.L. Henley. *Random Tiling Models*, pages 429–518. World Scientific, Singapore, 1991.

[90] Penrose Roger. *Bull. Inst. Math Appl.*, 10:266, 1974.

[91] Dov Levine and Paul Joseph Steinhardt. Quasicrystals: A new class of ordered structures. *Phys. Rev. Lett.*, 53:2477–2480, 1984.

[92] Paul J. Steinhardt and Ostlund S. *The Physics of Quasicrystals*. World Scientific, Singapore, 1987.

[93] DiVincenzo D.P. and Paul J. Steinhardt. *Quasicrystals - The State of the Art*. World Scientific, Singapore, 1991.

[94] N.G. de Bruijn. *Proc. K. Ned. Acad. Wet. Ser. A*, 43:39, 1981.

[95] A. J. Niemi and G. W. Semenoff. Index theorems on open infinite manifolds. *Nucl. Phys. B*, 269(1):131–169, 1986.

[96] R. Jackiw and C. Rebbi. Solitons with Fermion number 1/2. *Phys. Rev. D*, 13(12):3398–3409,

1976.

[97] Asel Sartbaeva, Stephen A. Wells, M. M. J. Treacy, and M. F. Thorpe. The flexibility window in zeolites. *Nat. Mater.*, 5:962–965, 2006.

[98] Nitin Upadhyay, Bryan Gin-ge Chen, and Vincenzo Vitelli. Nonlinear conduction in a topological mechanical insulator. *PNAS*, 111(36):13004–13009, 2014.

[99] Vincenzo Vitelli, Nitin Upadhyay, and Bryan Gin-ge Chen. Topological mechanisms and classical spinor fields. *arXiv:1407.2890*, 2014.

[100] Paulose Jayson, Bryan Gin-ge Chen, and Vincenzo Vitelli. Topological modes bound to dislocations in mechanical metamaterials. *Nature Physics*, 11:153-156, 2014.